MULTIPACTOR DISCHARGE WITH TWO-FREQUENCY RF FIELDS

By

Asif Iqbal

A DISSERTATION

Submitted to
Michigan State University
in partial fulfillment of the requirements
for the degree of

Electrical Engineering – Doctor of Philosophy

2021

ABSTRACT

MULTIPACTOR DISCHARGE WITH TWO-FREQUENCY RF FIELDS

By

Asif Iqbal

Multipactor is a nonlinear ac discharge in which a high frequency rf field creates an electron avalanche sustained through secondary electron emission from metallic or dielectric surfaces. Multipactor discharge can adversely affect various rf systems, such as telecommunications systems, high power electromagnetic sources, and accelerator structures. The restricted frequency spectrum and the cluttered satellite orbits require a single spacecraft to perform the same or enhanced functions which previously required several satellites. This necessitates complex multi-frequency operation for a much-enlarged orbital capacity and mission, where the requirement of high power rf payload significantly increases the threat of multipactor. This work provides a comprehensive understanding of multipactor discharge driven by two-frequency rf fields. The study provides important results on single and two-surface multipactor, including multipactor mitigation, migration of electron trajectory, and frequency domain analysis.

We use Monte Carlo simulations and analytical calculations to obtain single surface multipactor susceptibility diagrams with two-frequency rf fields. We present a novel multiparticle Monte Carlo simulation model with adaptive time steps to investigate the time dependent physics of the single surface multipactor. The effects of the relative strength and phase of the second carrier mode as well as the frequency separation between the two carrier modes are studied. It is found that two-frequency operation can reduce the multipactor strength compared to single-frequency operation with the same total rf power. Migration of the multipactor trajectory is demonstrated for different configurations of the two-frequency rf fields. Formation of beat waves is observed in the

temporal profiles of the surface charging electric field with small frequency separation between the two carrier modes.

We study the amplitude spectrum of the surface charging field due to multipactor in the frequency domain. It is found that for the single-frequency rf operation, the normal electric field consists of pronounced even harmonics of the driving rf frequency. For two-frequency rf operation, spectral peaks are observed at various frequencies of intermodulation product of the rf carrier frequencies. Pronounced peaks are observed at the sum and difference frequencies of the carrier frequencies, at multiples of those frequencies, and at multiples of the carrier frequencies.

We also study two surface multipactor with single- and two-frequency rf fields using Monte Carlo simulations and CST. The effects of the relative strength and phase of the second carrier mode, and the frequency separation between the two carrier modes on multipactor susceptibility are studied. Regions of single and mixed multipactor modes are observed in the susceptibility chart. The effect of space charge on multipactor susceptibility and the time dependent physics is also studied.

ACKNOWLEDGEMENTS

First, I would like to express my gratitude to my advisor, Professor Peng Zhang. Since the first day of my graduate study, Professor Zhang has provided me with endless guidance and support. As I was in his first batch of students, there was no senior graduate student when I joined the group. Therefore, Professor Zhang himself had to undertake the tedious role of teaching me the elementary physics of multipactor discharge. Even with his busy schedule, he always prioritized my training and development. I would like to thank him for being patient with my shortcomings and inadequacies. He has been an excellent mentor who leads with encouragement and leads by example. Watching him and working with him every day has helped me be more responsible and disciplined. Professor Zhang has made a world of difference in many aspects of my academic and personal development.

I would also like to thank Professor John Verboncoeur, for his encouragement and support throughout the course of my graduate study. His vast expertise on the field and his thorough guidance has been most valuable in the progress of my PhD research. I am also grateful to Professor Sergey Baryshev for providing many useful insights and advices on my work. I wish to thank him for the many lively discussions we had over the past few years. I would also like to thank Dr. John Luginsland for serving on my thesis committee and sparing his valuable time to discuss technical details with me.

I would like to thank Dr. Scott Rice for giving me important guidelines regarding the Monte Carlo codes for modeling multipactor discharge. I also wish to thank Dr. De-Qi Wen and Dr. Patrick Wong for giving me opportunities to collaborate with them in interesting projects. I wish to thank my friends Sneha Banerjee, Janez Krek, and Yi Luo from the NanoPATh and the PTSG research groups at MSU for their help throughout my research and graduate coursework. I would like to thank Dr. Wasif Afsari Khan and Dr. Jubaid Abdul Qayyum for helping me with my qualifying and comprehensive examination preparation and for their guidance on academic and personal matters. My journey in graduate studies would not be smooth and enjoyable without the friendship and love of my friends Md. Ashikuzzaman, Md Golam Morshed, Nezam Uddin, Md Afibuzzaman, and Shams Reaz. I would especially like to thank my wife, Armin Rahman Mouly, for her love and support throughout my graduate studies. Lastly, I would like to dedicate this thesis to my parents. Without their endless sacrifice, support, and constant encouragement I would not be where I am today.

This work was supported by the Air Force Office of Scientific Research (AFOSR) Award No. FA9550-18-1-0062. I would also like to acknowledge the Michigan Institute for Plasma Science and Engineering Graduate Fellowship.

TABLE OF CONTENTS

LIST OF TABLES

LIST OF FIGURES

CHAPTER 1: Introduction

This Chapter is based on a manuscript under review titled, "A Review of Recent Studies on Two-Frequency RF Field Induced Single Surface Multipactor", by A. Iqbal, *et al*.

1.1. Motivation

A multipactor discharge [1–7] is a nonlinear phenomenon in which electrons driven by a high frequency rf field create an avalanche by impacting one or more metallic or dielectric surfaces. The electron avalanche sustains itself by an exponential charge growth through secondary electron emission [8–11] from the surfaces. If this avalanche of electrons reaches a sufficiently high saturation level [2,4,5] by inducing appreciable outgassing from the surface, it can eventually turn into a gaseous-like discharge within the desorbed gas layer which is called flashover [12] .

While there are some beneficial aspects of multipactor discharge [3], such as vacuum conditioning or electron sources, it is considered detrimental to rf systems in most applications. The discharges may cause breakdown of dielectric windows [13–16], erosion of metallic structures, melting of internal components and perforation of vacuum walls [2] (Fig. 1.1). Multipactor can also detune rf systems, limit the delivery of rf power, and cause a local pressure rise due to the desorption of surface gases [17]. In some cases [18,19], multipactor can induce a glow discharge below the expected minimum pressure for a multipactor-free, Paschen-type rf glow discharge [20]. Due to its various undesired effects, multipactor has been a major concern for high power microwave (HPM) sources [21–26], rf accelerators [15], and space-based communication systems [27–37].

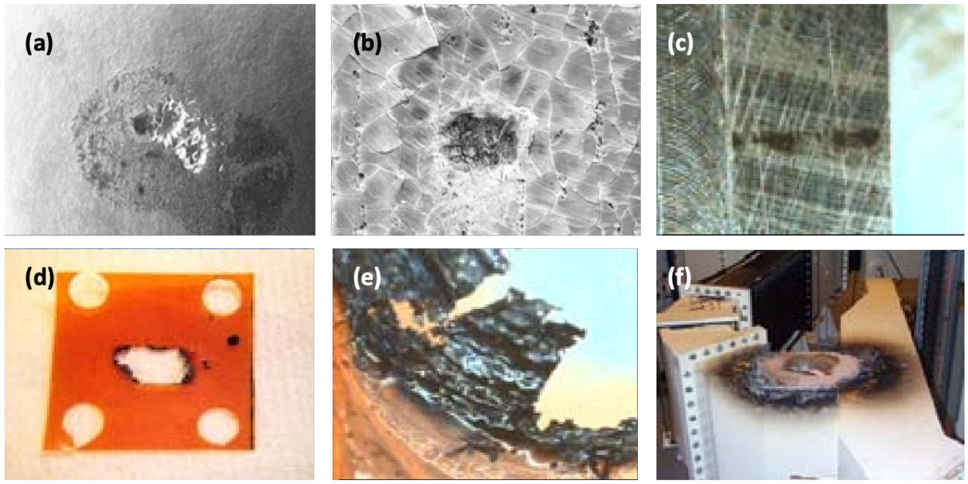

Figure 1.1. Damage caused by multipactor discharge in (a) Silver Band pass filter, (b) Anodized Band pass filter, (c) Aluminum waveguide, (d)-(e) Kapton pressure flange, and (f) Treated waveguide. (Image Courtesy: European Space Agency [38])

To date, theoretical and experimental multipactor investigations have heavily focused on the single frequency rf field induced multipactor discharge. Voltage, frequency, and geometric criteria for multipactor development have been studied thoroughly for single frequency rf field, as will be discussed in the next section. However, many modern communication systems employ multicarrier rf transmission [39,40]. A primary requirement for modern satellites and spacecraft is the ability to perform complex multifrequency communication through restricted frequency spectrum [36]. Additionally, in recent times, due to restricted availability of orbital slots, several advanced communication missions are being frequently incorporated in a single satellite payload rendering multifrequency communication essential [41]. When a number of carrier waves are transmitted simultaneously at different frequencies through the system, modulation of the signal amplitude takes place which may significantly modify the conditions for multipactor breakdown [40]. Incidental superposition of multiple frequencies can also occur in many rf components due to coupling between imperfectly isolated subsystems, such as in transmission lines and supporting components. Therefore, it is imperative to understand multipactor discharge with multi-frequency rf fields.

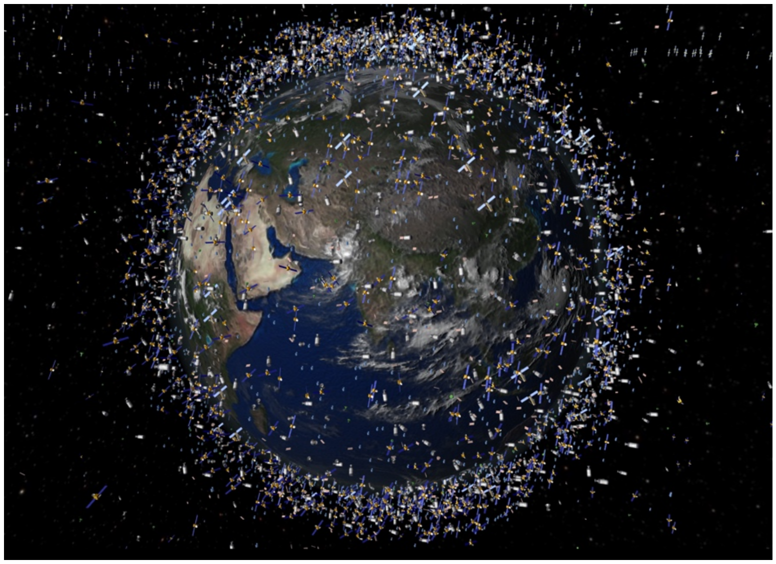

Figure 1.2. An artist's impression of satellites orbiting the earth based on actual data. Objects are shown at an exaggerated size to make them visible at the scale shown. According to the United Nations Office for Outer Space Affairs (UNOOSA) Online Index of Objects Launched into Outer Space, 4665 satellites are orbiting the earth in June 2020. Number of satellites are expected to increase drastically in the next decade as tens of thousands of new broadband satellites have been planned to be deployed. Protecting satellite components exposed to multifrequency rf operation from damages due to multipactor discharge is a major concern. (Image Courtesy: European Space Agency)

Many recent studies have been conducted to date on multipactor discharge induced by rf fields consisting of multiple carrier modes [28–32,39,42]. However, important aspects of multipactor discharge due to multi-frequency rf operation, such as the multipactor susceptibility, time dependent physics, and frequency domain analysis on single surface multipactor have been rarely studied and are still not very well understood. This dissertation aims to provide a detailed account of multipactor discharge with two frequency rf fields. The simulation methods and analytic theory for the study have been developed based on extensively used and well understood principles of classical electron dynamics. By understanding multipactor discharge with two frequency rf fields, rf systems can be better designed to mitigate multipactor. The data from this study can be used for verification of present and future experiments. They could also lead to the development of new technologies which may take advantage of the multipactor discharge.

1.2. Historical Background of Multipactor

1.2.1. 1920's-1970's

Multipactor discharge was first reported in the 1920's by French physicists C. Gutton and H. Gutton [43]. The first conceptual description of multipactor phenomenon in American technical literature was given in 1934 by Philo T. Farnsworth [1]. He employed multipactor to design an electron multiplier tube capable of producing current in the form of multipacting electrons to drive a fluorescent screen and produce a television image. Farnsworth first referred to this phenomenon as "multipactor" [1] and received several patents on technologies which highlighted multipactor discharges [44–47]. Observations of multipactor in gaseous breakdown experiments in 1930's and 1940's led to many early theories. In 1936, Henneburg *et al.* [48] derived the resonance condition on the transit time for electrons emitted with zero initial velocity, and also identified single particle phase focusing and stability of the discharge.

In the 1940's, while investigating high frequency gas discharges at low pressure, Gill and von Engel of Oxford University rediscovered multipactor [49] and later conducted many theoretical and experimental studies on the subject of multipactor discharge. Gill experimentally outlined part of the region of multipactor susceptibility and advanced a theory that recognized the sensitivity of the solution to a nonzero emission velocity of secondaries. Gill provided a theoretical relation between the amplitude, phase, and frequency of the driving field, and the multipactor trajectory length. Gill and von Engel introduced the ad hoc assumption that the ratio of the impact velocity of the primaries to the emission velocity of secondaries is a constant parameter denoted by k. This assumption was made without any physical basis to avoid the complications of a distribution of random emission velocities.

In 1950's, Hatch and Williams reformulated [6,7] the theory within a more concise mathematical framework and obtained reasonable agreement to their own multipactor experiments. However, they retained the constant k assumption of Gill and von Engel with some modifications. Even with this flawed assumption, the theory was useful in constructing susceptibility curves and remained the classic theory on the accessibility of multipactor for decades.

It is important to note that these early theoretical treatments of multipactor [6,7,49] were based on simple assumptions such as negligible space charge effects and electric fields that only vary in time, and are invariant with respect to the location between the bounding surfaces, as would be the case for an infinite parallel plate geometry. These assumptions help the mathematical relationships of multipactor resonance to be derived and have been frequently adopted by later researchers as well.

Research on multipactor discharge during this period heavily focused on two surface multipactor and investigation on single surface multipactor was scarce. However, in his 1961 publication Vaughan [14] described two types of experimentally observed dielectric window failure in magnetrons and klystrons namely *cracking* and *puncturing* and attributed these failures to the electrostatic charging of an evaporated metallic deposit on the surface and an internal multipactor discharge, respectively. In the same year, Preist and Talcott [13] suggested that the dielectric window failure in microwave tubes could be attributed to excessive heating caused by "electron bombardment". They proposed a theory and outlined the necessary conditions for such dielectric failure to take place which was essentially the first theoretical treatment of single surface multipactor. In the late 1990's Kishek *et al.* expanded on that theory and conducted a comprehensive study [4,50] on the topic.

1.2.2. 1980's-Present

In the 1980's, Vaughan [2] promoted an alternative to the constant-k theory from first principles. In contrast to the constant-k theory, Vaughan's theory uses more realistic assumption of a monoenergetic nonzero initial velocity. It was adopted by many researchers in the 1990's and 2000's such as Riyopoulos *et al.* [51–53], Kishek *et al.* [50,54–56], Ang. *et al.* [57], and Valfells *et al.* [58,59] etc. Riyopoulos *et al.* extended the theory to include a crossed-magnetic field [51] and studied the multipactor saturation induced by space charge debunching [53]. Kishek *et al.* extensively studied the multipactor discharge and rf circuits interaction [54] and the phase focusing mechanism in the parallel plate geometry [55]. The numerous theoretical and computational studies and experimental investigations of the multipactor effect are summarized in the review articles of Vaughan [2] and Kishek [3] up through the time of their respective publication years of 1988 and 1998.

In 2010, S. Anza *et al.* proposed an alternative to the classical theory of electron dynamics called the nonstationary statistical theory [28] for both two surface and single surface multipactor with experimental validation. Recently, Moiz Siddiqi and Rami Kishek have proposed a map based theory [60] based on principles from nonlinear dynamics and chaos theory to study multipactor discharge. The theory has been employed in parallel plate geometry to study multipactor stability and growth [61] and to obtain susceptibility charts [62]. The theory has also been employed in single surface [63] and coaxial [64] geometry.

The theory of multipactor discharge on single dielectric surface has been extensively researched since the 1980's. Notable numerical investigations were carried out employing Monte

Carlo (MC) particle simulations [3,5,40] and particle-in-cell (PIC) simulations [65]. The classical analytical theory based on electron dynamics has been employed to study the single surface susceptibility diagram [4] and power deposition on to the dielectric [57]. The effects of space charge [58,66], external electric and magnetic fields [5,59,67], oblique rf electric fields [59,68], wave reflection [67], desorption or background gases [5,69] have been investigated. The transition of window breakdown from vacuum multipactor discharge to rf plasma has been studied, by both PIC simulations [65] and volume-averaged global models (GM) [70,71]. Analytical scaling laws have been derived for dielectric window breakdown in vacuum and collisional regimes [72]. Time-dependent physics of single surface multipactor has been investigated [73].

It is worthwhile to note that in addition to single and two surface geometries, multipactor discharge has been extensively studied for other geometries such as coaxial [34,64,74–77], rectangular [78,79], microstrip [80], circular [81,82], and elliptical [83] waveguides. Also noteworthy is that in recent years, along with numerical and analytical studies, much emphasis has been put on computer aided simulations of multipactor discharge using software such as the Multipactor Electron Simulation Tool (MEST) [84,85] and the Computer Simulation Technology (CST) [86–88].

In recent years, studies on multipactor have heavily focused on its mitigation since avoiding multipactor is critical in the operation of certain systems as described in Section 1.1. Treatments to mitigate multipactor in various applications can be roughly categorized into two approaches. The first approach is mitigation by engineering the device susceptible to multipactor, which can be further categorized into three methods: conditioning of the components by the discharge [89], surface treatments such as coating [89–93], and geometrical modification [94–98]. Conditioning is a lengthy process that depends on the discharge affecting the surface characteristics enough to quench itself. Surface treatments include using materials with low secondary electron yield (SEY), such as TiN [99,100], for device fabrication or surface coating. D. C. Joy provided [85] a large database of materials' SEY which is very useful in this respect. However, there is lack of stable materials with low SEY, especially for extreme system requirements [93]. Geometrical modification can be useful in two ways. Firstly, artificially roughened or porous surfaces can be introduced to reduce the SEY [94–96,102,103]. Secondly, geometric modification can be employed to alter the trajectories of electrons so as to eliminate multipactor at frequencies of interest [104,105]. Although these processes can be effective for multipactor mitigation in future devices, components already in use in various applications often cannot benefit from these treatments. For example, replacement of existing microwave components in satellites that degrade system performance and face the risk of damage due to multipactor is not possible [106]. Moreover, system geometries may have engineering constraints or may be fixed by the necessary boundary conditions as in a waveguide, and other methods must be employed to prevent multipactor.

The second approach of mitigation is by modifying the electric or magnetic fields that the devices are exposed to. This can be done by either applying external electric and/or magnetic fields or by modifying the driving rf electric field. A. Valfells *et al.* showed [59] that a large external magnetic field perpendicular to the rf electric field and to the normal electric field can significantly reduce multipactor on a single dielectric surface. C. Chang *et al.* demonstrated both theoretically [107] and experimentally [108] that high-power microwave (HPM) dielectric multipactor can be suppressed by utilizing external resonant magnetic field. O. A. Ivanov *et al.* demonstrated [109] in their experimental study that an external dc bias repulsing the charges from a single dielectric (quartz) surface can mitigate multipactor. Mitigation by modification of the driving rf electric field, such as the two-frequency and the multicarrier operation, is a rather vast domain itself that we will discuss in section 1.3. In 2011, Chang *et al.* summarized recent theoretical and experimental progress on improving HPM multipactor and breakdown threshold [110].

1.3. Multipactor and Multicarrier RF Operation

Since the multicarrier rf operation has been extremely important in diverse applications in recent years, a number of studies have been conducted during this period to address multipactor discharge for the multicarrier rf operation. Majority of the studies on multicarrier rf field induced multipactor discharge have been carried out for two surface geometry. To tackle multicarrier multipactor discharge for parallel plate waveguides, the industry has widely adopted semi-empirical multipaction threshold prediction methods [111] including the most commonly employed “20 gap crossing rule” [30] which is based on the dependency of the multipactor discharge on the signal envelope. The rule states that multipactor occurs when the multicarrier signal envelope exceeds the single carrier multipactor threshold for an interval equal or longer than 20 times the time for an electron to cross the gap [111]. In the academia, S. Anza *et al.* generalized the nonstationary statistical theory for multicarrier signals [29] and showed that the prediction accuracy of the nonstationary theory is better than the 20-gap-crossing rule [31]. Siddiqi and Kishek employed their map based theory to investigate the long term multipactor discharge for two-frequency rf field [112]. Wong *et al.* recently proposed a model [36] to assess the effects of multipactor on the on the distortion of a signal for planer and coaxial geometry. They also proposed a novel way of using multipactor discharges for harmonic generation [113] by using the intrinsic phase-focusing mechanism of multipactor as a natural charge-bunching mechanism. A. A. Hubble *et al.* studied multipactor under two-tone [114] and multicarrier [35] rf operations in microstrip geometry and proposed useful improvements in multipactor testing and diagnostics [115–117].

Several studies have been conducted on the frequency domain analysis of two surface multipactor as well. Tang and Kudsia investigated [118] multipactor breakdown and passive intermodulation (PIM) in microwave components for satellite applications. Zhang *et al.* investigated [119] passive intermodulation in a parallel plate transmission line (PPTL) caused by multipaction with 2-frequency and 4-frequency rf signals. Semenov *et al.* proposed a simplified analytical model [120] to predict the spectrum of electric current induced by the multipacting electrons between two parallel electrodes exposed to a single frequency rf electric field.

Multicarrier operation has also been found effective for multipaction mitigation. Semenov *et al.* [39] showed in early 2000's that with two-frequency rf operation, mitigation of multipactor breakdown can be achieved in a metallic gap when the two carrier waves have close but separated frequencies. By employing the two-frequency rf field, Rice *et al.* [121] demonstrated the migration of multipactor trajectories to specific desirable locations in the parallel plate geometry for the purpose of cleaning the structure or reducing multipactor susceptibility. For the single surface geometry, Wen *et al.* [122] demonstrated reduction of multipactor discharge due to non-sinusoidal rf waveshapes, which is intrinsically a multi-frequency waveform, using Particle-in-cell (PIC) [65,73] and multiparticle Monte Carlo (MC) [123,124] simulations.

Despite recent increased focus on multicarrier rf field induced multipactor, several key aspects in this domain still lack clear understanding. For example, multipactor susceptibility is not well characterized for single-surface and two-surface multipactor for multicarrier rf operation and the time dependent physics has not been comprehensively studied. In addition, the frequency domain analysis of single surface multipactor is rarely studied. This thesis attempts to address some of these issues theoretically.

1.4. Organization of this Dissertation

This dissertation is organized into six chapters, with this introduction being Chapter 1. Chapter 2 provides theoretical and computational methodology for single surface multipactor discharge with two frequency rf fields in the absence of space charge effects. The electron dynamics as well as the relationship between multipactor and the secondary electron yield (SEY) of surfaces sustaining multipactor are discussed. Monte Carlo and analytical approaches to analyzing multipactor are then discussed. In the final section of the chapter, a novel multiparticle Monte Carlo simulation model is presented, which can be employed to investigate the time dependent physics of single surface multipactor discharge.

Chapter 3 presents a detailed analysis of the time-dependent physics of multipactor discharge on a single dielectric surface with a transverse rf electric field of two carrier frequencies using the multiparticle Monte Carlo simulation model presented in Chapter 2. The time averaged multipactor susceptibility diagrams are constructed for two-frequency rf fields. Effect of the relative strength and phase of the second carrier mode on multipactor electron trajectories are presented. The phase space evolution of multipactor electrons is examined. Effect of non-integer frequency ratio on the time dependent physics is described.

Chapter 4 presents the comprehensive frequency domain analysis of multipactor discharge on a single dielectric surface for both single- and two-frequency rf operations. The amplitude spectrum of the normal electric field, its frequency components and their strengths are analyzed.

In Chapter 5 we present an investigation on two-surface multipactor discharge. First, we reproduce important previous results, such as the susceptibility charts, for the single frequency rf operation, by employing both analytical and Monte Carlo approaches. Next, for two-frequency operation, susceptibility charts produced by Monte Carlo simulation are presented, showing the effects of the second carrier mode on multipactor susceptibility.

Chapter 6 concludes this dissertation with a summary of the results obtained, and possible directions for future works.

CHAPTER 2: Fundamentals of Single Surface Multipactor and a Novel Multiparticle Monte Carlo Method

In this Chapter, we present the theoretical and computational methodology of studying single surface multipactor discharge with two frequency rf fields in the absence of space charge effects. The chapter begins with discussions on the electron dynamics of single surface multipactor discharge and the secondary electron yield (SEY) of surfaces sustaining multipactor. Then we present the Monte Carlo and analytical approaches to analyze multipactor susceptibility on a dielectric. We discuss the limitations of existing Monte Carlo simulation schemes in investigating the time dependent physics of single surface multipactor discharge. Finally, we present a novel multiparticle Monte Carlo simulation model to overcome these limitations. This Chapter contains figures and excerpts from [40,123] which have been reproduced with permission from AIP Publishing.

2.1. Electron Dynamics

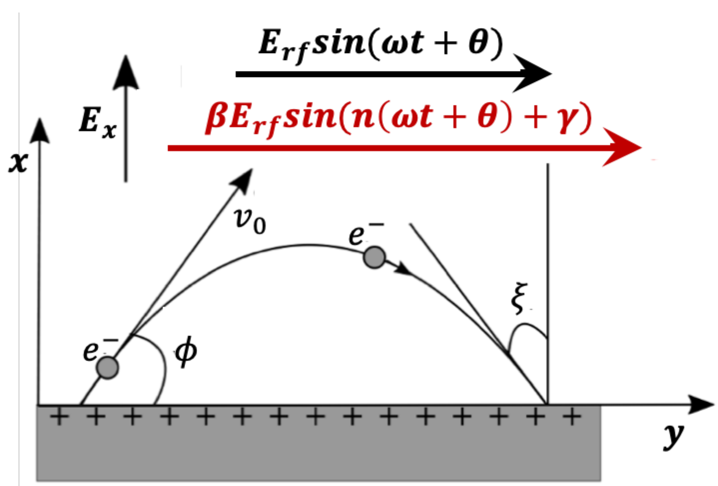

Figure 2.1. Schematic of the single surface multipactor discharge in a normal electric field and a parallel rf field with two carrier frequencies.

Figure 2.1 shows the schematic of single surface multipactor discharge. An rf electric field $E_y = [E_{rf}\sin(\omega t+\theta) + \beta E_{rf}\sin(n(\omega t+\theta)+\gamma)]$ is applied parallel to the surface along the y-direction. Here E_{rf} is the peak electric field strength, ω is the angular frequency, and θ is the initial phase of the electric field, of the fundamental carrier mode. β is the field strength of the second carrier mode relative to the fundamental mode, γ is the relative phase of the second carrier mode when $(\omega t+\theta) = 0$ or integer multiple of 2π, and n is the ratio of the two carrier frequencies. The multipactor electrons are subjected to forces imposed by this parallel rf electric field and the normal electric field E_x originating from the residual charge on the dielectric acting along the x-direction (Fig. 2.1). In our studies, the possible space-charge effects due to multipactor electrons are not considered [16,40,65,123], except the varying strength of E_x, which is captured in Monte Carlo simulations, as discussed in Sec. 2.5 below [125]. Referring to Fig. 2.1, the flight trajectory of a multipactor electron is governed by the force law,

$$m\frac{\partial \vec{v}}{\partial t} = -\mid e\mid\left[\vec{E}_{rf}\sin(\omega t+\theta) + \beta\vec{E}_{rf}\sin(n(\omega t+\theta)+\gamma) + \vec{E}_x\right]. \tag{2.1}$$

The velocity of the electron is obtained as,

$$v_x = -\frac{|e|}{m}E_x t + v_0 sin\phi, \tag{2.2a}$$

$$v_y = \frac{\mid e\mid}{m\omega}E_{rf}\left\{cos(\omega t+\theta) - cos\theta + \frac{\beta}{n}[cos(n(\omega t+\theta)+\gamma) - cos(n\theta+\gamma)]\right\} + v_0 cos\phi, \tag{2.2b}$$

where v_0 and ϕ are the emission speed and emission angle with respect to the surface of the multipactor electron, respectively. From Eq. (2.2), we obtain the instantaneous position of a multipactor electron as,

$$x = -\frac{|e|}{2m}E_x t^2 + v_0 t sin\phi + x_0, \tag{2.3a}$$

$$y = \frac{|e|}{m\omega} E_{rf} \left\{ \frac{1}{\omega}(sin(\omega t + \theta) - sin\theta) - tcos\theta + \frac{\beta}{n}\left[\frac{1}{n\omega}(\sin(n(\omega t + \theta) + \gamma) - \sin(n\theta + \gamma)) - tcos(n\theta + \gamma)\right]\right\} + v_0 tcos\phi + y_0. \tag{2.3b}$$

Here x_0 and y_0 account for the initial position of the particles at $t = 0$. The transit time τ of an electron in flight is calculated by solving Eq. (2.3a) for $x = 0$. Note the solutions to Eq. (2.1) given in Eqs. (2.2a, 2.2b) and (2.3a, 2.3b) apply only during the intervals between any two consecutive impacts from the entire ensemble of particles upon the surface, during which the normal electric field E_x remains constant. E_x changes only upon the impact of any particle onto the dielectric surface.

2.2. Secondary Electron Yield

The average number of secondary electrons produced by the impact of each primary electron upon the surface is called the secondary electron yield, δ. It is a function of the impact energy of the primary electron, E_i, and the angle to the normal, ξ, at which it strikes the surface [10]. It also depends on material properties translating into two parameters, the maximum yield, δ_{max}, and the energy at which it occurs, E_{max}. We specify these parameters and adopt Vaughan's empirical formula [10], to estimate the secondary electron yield for normal incidence [10,126] to estimate the secondary electron yield,

$$\frac{\delta(\xi)}{\delta_{max}(\xi)} = (we^{1-w})^k, \text{ for } w \le 3.6; \tag{2.4a}$$

$$\frac{\delta(\xi)}{\delta_{max}(\xi)} = 1.125/w^{0.35}, \text{ for } w > 3.6, \tag{2.4b}$$

where $w = E_i/E_{max}$, $k = 0.56$ for $w < 1$, $k = 0.25$ for $1 \le w \le 3.6$. The parameters are adjusted in calculating the yield, for impact at an angle ξ with respect to the normal (Fig. 2.1), according to the following equations [10,126]:

$$E_{max} = E_{max0}\left(1 + \frac{K_{sE}\xi^2}{2\pi}\right), \tag{2.5a}$$

$$\delta_{max} = \delta_{max0}\left(1 + \frac{K_{s\delta}\xi^2}{2\pi}\right). \tag{2.5b}$$

In this study, we choose $E_{max0} = 400eV$ and $\delta_{max0} = 3$ as the parameters for an impact angle $\xi = 0$ (i.e., normal to the surface, c.f. Fig. 2.1) which is typical for some materials used in rf windows [4]. k_{sE} and $k_{s\delta}$ are a surface smoothness factors for E and δ ranging from 0 for a rough surface to 2 for a polished surface. In this paper we set the values $k_{sE} = k_{s\delta} = 1$, representing a typical dull surface [10,126]. Two values of impact energy, termed the first and second crossover points, E_1 and E_2, respectively, result in a yield of 1, with $\delta > 1$ in between (Fig. 2.2).

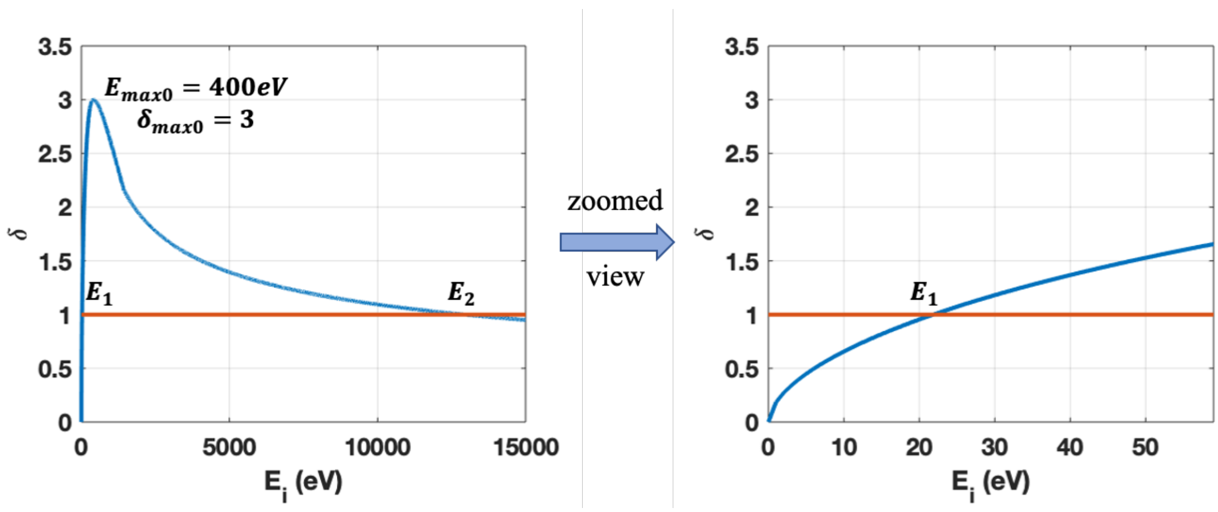

Figure 2.2. SEY vs. incidence energy curves from Vaughan's models for impact angle $\xi = 0$.

2.3. Monte Carlo Simulation – Single Particle Approach

To calculate the growth rate of the multipactor discharge and thus to construct the multipactor susceptibility diagram for a given set of surface charging field E_x, and rf electric field E_{rf}, we follow the trajectory of a weighted macroparticle over a large number of impacts in a MC simulation [4,5,57]. The initial rf phase, θ, is uniformly distributed over $0 < \theta < 2\pi$ (Fig. 2.1).

Each time a macroparticle leaves the surface, we assign it a random initial energy $E_0 = (½)mv_0^2$ and angle ϕ according to the following distributions [4]:

$$f(E_0) = \frac{E_0}{E_{0m}^2} e^{-\left(\frac{E_0}{E_{0m}}\right)}, \tag{2.6a}$$

$$g(\phi) = \frac{1}{2} sin\phi, \qquad 0 < \phi < \pi \tag{2.6b}$$

where E_{0m} is the peak of the distribution of emission energies, on the order of the work function, i.e., a few eV. The expected value of E_0 is $2E_{0m}$, and $\int g(\phi)d\phi = 1$ over $0 < \phi < \pi$. Substituting these random values of initial velocity and angle into Eqs. (2.2) and (2.3), we obtain the impact energy, E_i, and impact angle, ξ, and hence, the secondary electron yield, δ, from Eq. (2.4). We use this value of the yield to adjust the charge and mass on the macroparticle and then emit it again with a random velocity. We repeat the process to obtain a series of yields $(\delta_1 . \delta_2 \ldots \delta_N)$ for a large number of impacts. In order to average out the dependence of a secondary electron's flight trajectory upon the rf conditions of a primary electron's impact onto the surface, the phase of the rf field θ can be randomly assigned at the beginning of each flight. Alternatively, the rf phase θ is randomly assigned only initially, and then calculated self-consistently $(\theta_{i+1} = \theta_i + \omega\tau_i)$ at the beginning of each flight for a given macroparticle, the process of which is then repeated for many independent macroparticles. It is found that the two approaches yield very similar results in terms of multipactor susceptibility. In this study, we present the results using the latter method. The average value of secondary yield over *N* impacts is then calculated as $\bar{\delta} = (\delta_1 . \delta_2 \ldots \delta_N)^{1/N}$, where a large N (e.g. = 200) is used in the calculation. The simulation is then repeated for $M = 100$ (independent) macroparticles. The median value of the secondary yield of these *M* independent macroparticles is calculated, which represents either an exponentially growing $(\bar{\delta} > 1)$ or an exponentially decaying $(\bar{\delta} < 1)$ trend in the number of electrons in the avalanche. This trend depends on the external parameters, such as E_x, E_{rf}, δ_{max0}, θ, n, β, and γ. For any given values of the fields, this average value of the secondary electron yield, averaged over the distributions of random emission energy, emission angle, and rf phase at emission, gives the growth rate. The boundaries of the multipactor susceptibility are determined when $\overline{\delta} = 1$, i.e., the exponential growth rate of the electrons equals zero. Figure 2.3 shows susceptibility diagrams obtained from the single particle Monte Carlo simulation with single- and two- frequency rf fields. Roughly, the lower (upper) boundary corresponds to electron impact energy on the dielectric surface equal to the first (second) crossover point in the secondary electron yield curve [4]. Typically, multipactor saturation occurs at the lower boundary.

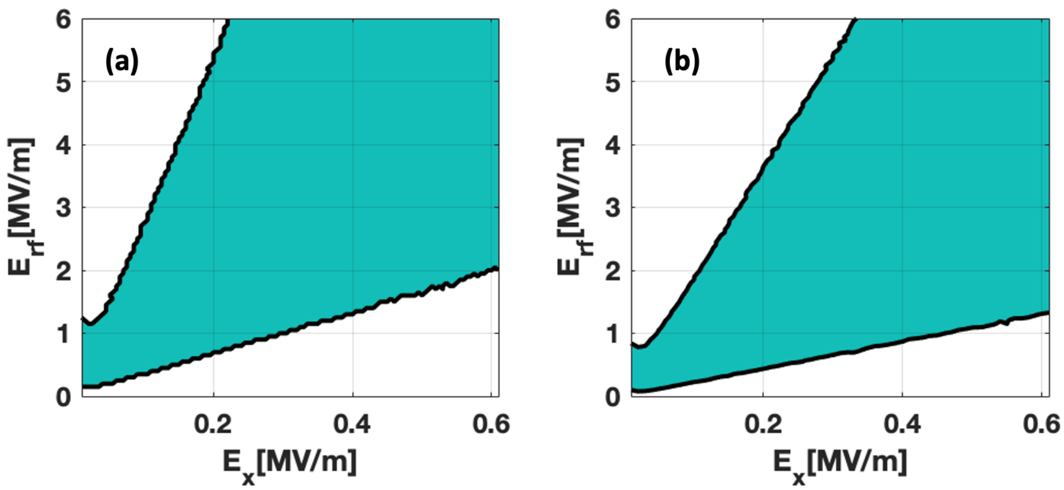

Figure 2.3. Multipactor susceptibility boundaries obtained from single particle Monte Carlo simulation in the (E_x,E_{rf}) plane for $\delta_{max0} = 3, E_{0m}/E_{max0} = 0.005$, with (a) single frequency rf field, (b) two frequency rf field with $n = 2, \gamma = 0$, and $\beta = 1$. For both cases, we use a fundamental rf frequency, $f_{rf} = 1GHz$. The colored region is the multipactor susceptibility region.

2.4. Analytical Solution

We follow Ref. [4,40] and assume that all electrons are emitted normal to the surface (i.e., $\phi = 90^0$ in Fig. 2.1), with a single energy $E_0 = (½)mv_0^2 = 2E_{0m}$. Hence, substituting $\phi = 90^0$ into Eqs. (2.2)– (2.4), averaging over rf phase θ, and setting the resulting average impact energy equal to E_1 and E_2 at $\xi \approx \pi/2$ [cf., Eqs. (2.4) and (2.5)], we obtain the following normalized equations for the lower and upper boundaries:

$$\bar{E}_{rf1,2} = \sqrt{\frac{2\bar{E}_{1,2}}{1-cos\bar{\tau}+\frac{\beta^2}{n^2}(1-cosn\bar{\tau})+\frac{\beta}{n}[\cos(n\bar{\tau}-\bar{\tau}+\gamma)-\cos(\bar{\tau}-\gamma)-\cos(n\bar{\tau}+\gamma)+cos\gamma]}}, \tag{2.7}$$

where $\bar{E}_{rf1,2} = \frac{|e|E_{rf1,2}}{\omega\sqrt{mE_{max0}}}$,$\bar{E}_{1,2} = \frac{E_{1,2}}{E_{max0}}$, $\bar{\tau} = \frac{2\sqrt{2\bar{E}_0}}{\bar{E}_x}$, $\bar{E}_0 = \frac{E_0}{E_{max0}}$, and $\bar{E}_x = \frac{|e|E_x}{\omega\sqrt{mE_{max0}}}$. When $\beta = 0$, Eq. (2.7) recovers the following boundaries of multipactor susceptibility for a single frequency rf field only [4],

$$\bar{E}_{rf1,2} = \sqrt{\frac{2\bar{E}_{1,2}}{1-cos\bar{\tau}}}. \tag{2.8}$$

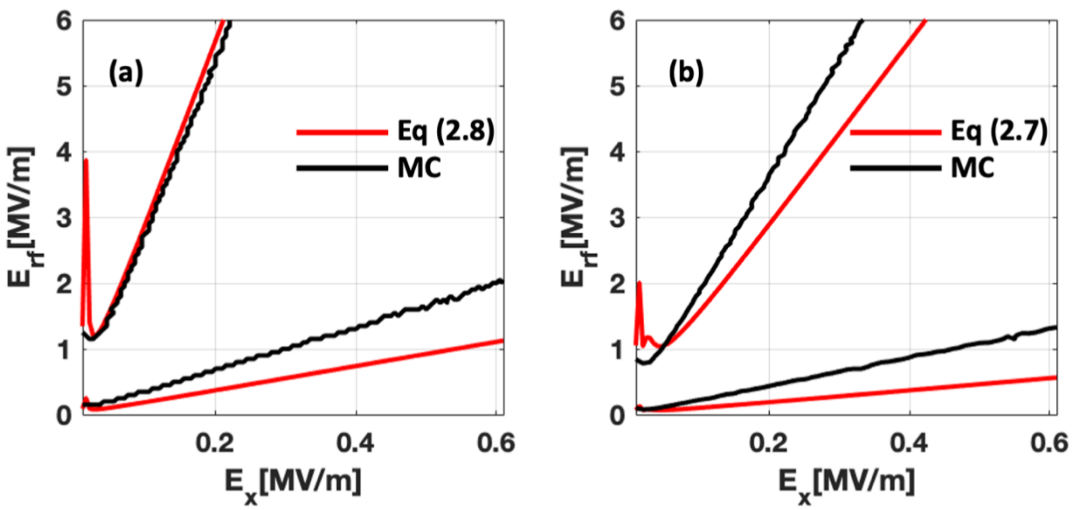

Figure 2.4. Multipactor susceptibility boundaries obtained from analytical calculation of Eqs. (2.8) and (2.7) (red lines) and from single particle Monte Carlo simulation (black lines) in the (E_x,E_{rf}) plane for $\delta_{max0} = 3, E_{0m}/E_{max0} = 0.005$, with (a) single frequency rf field, (b) two frequency rf field with $n = 2, \gamma = 0$, and $\beta = 1$. For both cases, we use a fundamental rf frequency, $f_{rf} = 1GHz$.

Figure 2.4 shows the multipactor region boundaries calculated from Eqs. (2.7) and (2.8) (red lines) and from the single particle MC simulation described in section 2.3 (black lines). The difference between the MC results and the analytical results is due to the simplified assumptions of the analytical solution. It is important to note that, implicit in the derivation of the analytical solution for the single surface multipactor susceptibility under two-frequency fields, we assume constant relative phase between the two carriers. In the early stage of multipactor discharge, or when the frequency ratio of the two carriers, n, is very close to unity, the evolution of relative phase is very slow with time, so that the relative phase may be regarded roughly as a constant.

2.5. Limitation of the Single Particle Monte Carlo Approach

Kishek *et al.* first employed the single particle Monte Carlo simulation approach for analyzing single surface multipactor susceptibility boundaries [3,4]. Later Ang *et al*. adopted this approach [57] for investigating time dependent physics of single surface multipactor.

To study the time dependent physics, a small normal electric field E_x is assigned only initially, and then calculated self-consistently as $E_{x,i} = \frac{\sigma_{e,i}}{2\epsilon_0}$ at the beginning of each flight i for the macroparticle, where $\sigma_{e,i} = \frac{q_{e,i}}{A}$ is the surface charge density, $q_{e,i}$ is the charge contained in the macroparticle producing this normal electric field, and A is the surface area ($1m^2$). The simulation is carried out for N impacts of the macroparticle on the surface. The temporal profiles of the rf electric field E_y, the electric field normal to the dielectric surface E_x, and the secondary electron yield δ are obtained by converting the iteration number N into the scale of time using the transit times τ_i for each iteration. Figure 2.5 shows these temporal profiles obtained from the single particle MC simulation.

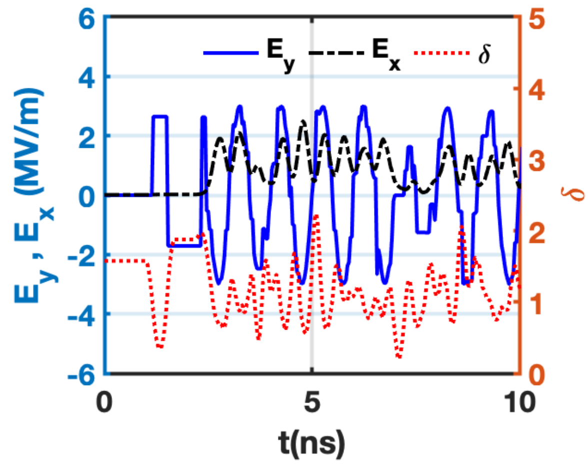

Figure 2.5. Instantaneous rf electric field, E_y (solid blue lines), normal electric field, E_x (broken black lines), and secondary electron yield, δ (dotted red lines), for single frequency rf field, $\beta = 0$ obtained from single particle MC simulation. The average secondary electron yield $\delta_{avg} = 1$ in the saturation regime. In the calculation, we set $f_{rf} = 1\text{GHz}$ and $E_{rf} = 3\text{MV/m}$.

As we can observe from Fig. 2.5, the temporal profiles of the rf (E_y) and the normal (E_x) electric fields, as well as the secondary electron yield (δ) obtained from the single particle MC simulation are of very low resolution. This is because the simulation is carried out with only one macroparticle and the total charge producing the normal electric field is assumed to be contained in that single macroparticle.

To overcome the limitation of single particle MC simulation, Kim and Verboncoeur adopted a variable number of particles approach [73], where the number of particles is varied in the simulation while the charge per particle is kept fixed. This allows for better statistics in a growing discharge, but is computationally costly [73], as the fixed time steps have to be set small compared to the time of flight of the particles between subsequent bounces on the surface.

2.6. Multiparticle Monte Carlo Simulation

In this section, we present a new one-dimensional multiparticle Monte Carlo (MC) simulation model [123] with *adaptive* time steps as a tool to investigate the time dependent physics of a single surface multipactor discharge.

In our model, we consider a system with many macroparticles. The number of macroparticles is held fixed throughout the simulation. Upon impact of each macroparticle onto the surface, the charge and mass in that macroparticle and the normal electric field to the dielectric surface are updated according to the secondary electron yield [10] and Gauss's law respectively. This approach captures the statistics better than the single particle approach. However, since the number of macroparticles is fixed in this model, it still offers a simpler and less costly implementation than the variable number of particles approach. More importantly, the time intervals between subsequent bounces of different macroparticles on the surface are calculated *exactly*.

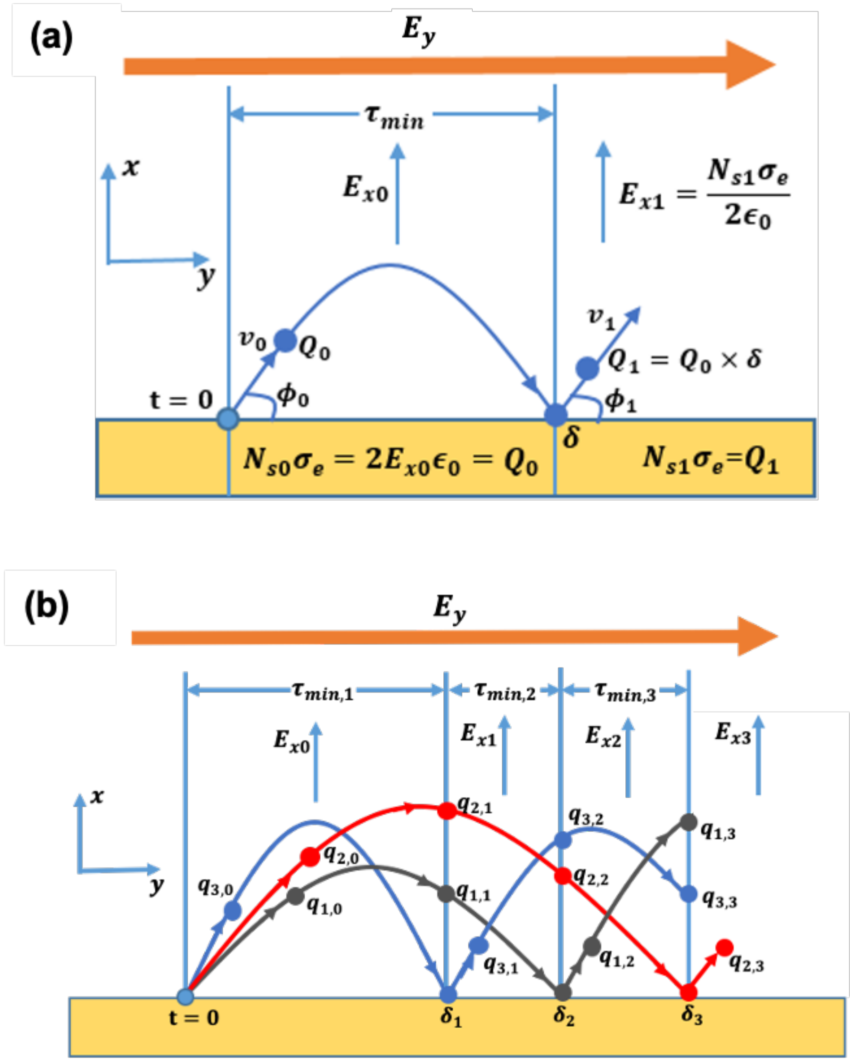

	Particle #1	Particle #2	Particle #3
Iteration #1	$q_{1,0}$	$q_{2,0}$	$q_{3,0}$
Iteration #2	$q_{1,1}$=$q_{1,0}$	$q_{2,1} = q_{2,0}$	$q_{3,1} = \delta_1 q_{3,0}$
Iteration #3	$q_{1,2} = \delta_2 q_{1,1}$	$q_{2,2} = q_{2,1}$	$q_{3,2} = q_{3,1}$
Iteration #4	$q_{1,3} = q_{1,2}$	$q_{2,3} = \delta_3 q_{2,2}$	$q_{3,3} = q_{3,2}$

Figure 2.6. Schematic of MC modeling of the single surface multipactor discharge: (a) single particle model; the number of electrons in flight, Q_i, total surface charge, N_{si}, and normal electric field, E_{xi}, are updated at each impact of a single macroparticle onto the surface. (b) multiparticle model; multiple macroparticles are in flight, each iteration traces one impact of a macroparticle onto the surface; the charge, q_i, and mass, m_i, of only the incident macroparticle hit on the surface is updated after each iteration. Total surface charge, N_{si}, and the normal electric field, E_{xi}, are calculated as described in the text.

A single dielectric surface is exposed to a parallel rf electric field, E_{rf}. An initial electric field E_{x0} is assigned normal to the dielectric surface. This initial normal electric field is very small compared to the rf amplitude ($E_{x0} \sim E_{rf0}/30$). From Gauss's Law we have, $E_{x0} = \frac{\sigma_e}{2\epsilon_0}$, where $\sigma_e = \frac{N_{s0}e}{A}$ is the surface charge density, N_{s0} is the initial positive surface charge producing this normal electric field, and A is the surface area ($1m^2$). Therefore, we can calculate $N_{s0} = \frac{2AE_{x0}\epsilon_0}{e}$ from E_{x0}. A number of macroparticles ($N = 200$) are emitted from the dielectric surface at time $t = 0$ (Fig.2.6). Each macroparticle is assigned a random emission energy E_0 and random emission angle ϕ according to the distributions given in Eq. (2.6).

For charge neutrality, the total number of electrons in these macroparticles in flight is equal to N_{s0}. These initial electrons are considered to be uniformly distributed in the macroparticles. Therefore, the initial charge in jth macroparticle is $q_{j,0} = eN_{s0}/N$, where e is the electronic charge. The trajectories of the macroparticles are governed by the force law:

$$m\frac{\partial \vec{v}}{\partial t} = -\mid e \mid \left[\vec{E}_y + \vec{E}_x\right], \tag{2.9}$$

The macroparticles gain energy from the electric fields while in flight. After the period of flight, a macroparticle strikes the surface to emit secondary electrons [10,126]. In each iteration, we record one impact of a macroparticle upon the dielectric surface, with the transit time being calculated exactly (Fig. 2.6).

During the ith iteration, we first calculate the transit time, τ_j, of each macroparticle from the force law. The particle with the minimum transit time, $\tau_{min,i}$, strikes the surface first, yielding secondary electrons. We use Vaughn's empirical formula [10,126] to calculate the secondary electron yield (SEY), δ, at each impact.

If the kth macroparticle with charge $q_{k,(i-1)}$ strikes the surface at the ith impact, and the secondary electron yield for this impact is δ_i, then the charge in the kth macroparticle is updated for the next iteration as $q_{k,i} = \delta_i q_{k,(i-1)}$. During this impact, $q_{k,(i-1)}$ negative charge strikes the surface and $\delta_i q_{k,(i-1)}$ negative charge is emitted from the surface. Therefore, the positive surface charge is updated for the next iteration as $N_{si} = N_{s(i-1)} + q_{k,(i-1)}(\delta_i - 1)$. The normal electric field is updated as $E_{xi} = \frac{N_{si}e}{2A\epsilon_0}$. The charge in all other macroparticles in flight remain unchanged by this impact, i.e., for any jth particle that does not strike the surface, the charge is updated as $q_{j,i} = q_{j,(i-1)}$ for the next iteration. We record the position, $x_{j,i}$, and the instantaneous velocity, $v_{j,i}$, of these macroparticles at each impact. These values are used as initial conditions to calculate transit times during the next iteration. The rf phase, θ, is updated self consistently [40] at each iteration.

The kth macroparticle, incident during the ith iteration, is then emitted from the surface again at the $(i+1)$th iteration with updated charge $q_{k,i}$, a new emission energy, E_0, and a new emission angle, ϕ, according to the distributions given by Eq. (2.6). We continue this process for n impacts (or iterations). The temporal profiles of the surface charge N_s and the normal electric field to the dielectric surface E_x are obtained by converting the iteration number n into the scale of time using the transit times $\tau_{min,i}$ for each iteration. E_x obtained at this stage is on a non-uniform grid in time. We divide the time scale in uniform bins and compute the average E_x in each of those bins.

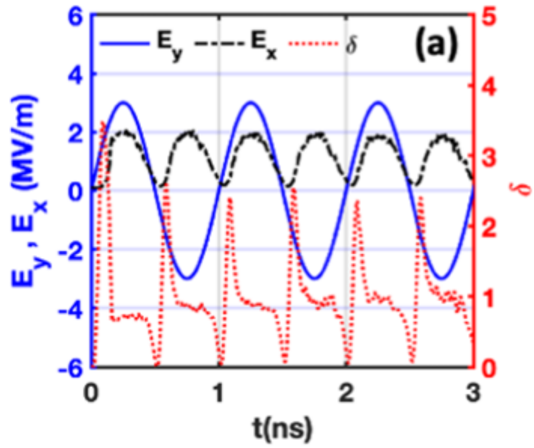

Figure 2.7. Instantaneous rf electric field, E_y (solid blue lines), normal electric field, E_x (broken black lines), and secondary electron yield, δ (dotted red lines), for single frequency rf field, $\beta = 0$ obtained from multiparticle MC simulation. The average secondary electron yield $\delta_{avg} = 1$ in the saturation regime. We set $f_{rf} = 1\text{GHz}$ and $E_{rf} = 3\text{MV/m}$ in the calculation.

As we can observe from Fig. 2.7, the multiparticle MC simulation scheme is able to resolve the statistics of the time dependent physics of single surface multipactor with much greater accuracy than the single particle MC simulation (Fig 2.5). The temporal profiles of the rf (E_y) and the normal (E_x) electric fields, as well as the secondary electron yield (δ) obtained from the multiparticle MC simulation are of high resolution. We observe that the temporal profiles of the normal electric (E_x) and the secondary electron yield (δ) oscillate at twice the rf frequency which agrees with the results obtained by Kim and Verboncoeur [73] from the variable number of particles approach and the Particle in Cell (PIC) simulations. In our MC model, the possible change of E_x during an iteration is not accounted for. The diagnostics are sampled over each iteration time step. In addition, space charge effects [58] are not considered. However, Fig. 2.8 shows that the temporal profiles of E_x obtained from the PIC simulation of Kim and Verboncoeur (Fig. 2(b) of [73]) which accounts for space charge effects and from our multiparticle MC technique (Fig. 2(a) of [123]) match almost exactly, for the special case of rf electric field amplitude $E_{rf0} = 3\text{MV/m}$ and rf frequency $f_{rf} = 1\text{GHz}$. This indicates that the effects of space charge may not be significant for the parameter space explored in this study. A detailed examination on the effects of space charge on single-surface multipactor dynamics and susceptibility is needed for future research, which is beyond the scope of this thesis.

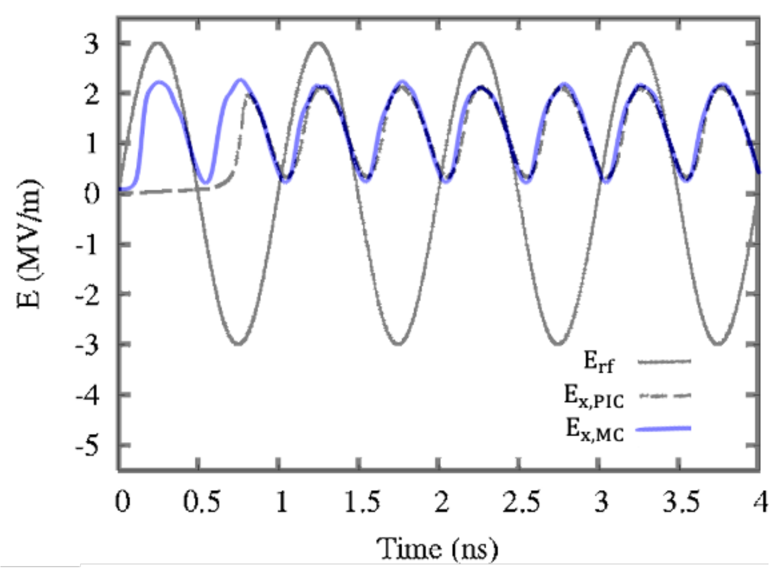

Figure 2.8. The temporal profiles of the normal electric field E_x for rf electric field amplitude $E_{rf0} = 3MV/m$ and rf frequency $f_{rf} = 1GHz$ from PIC simulation [73] (dashed black line) and the multiparticle MC simulation (solid blue line) [123]. The results from the MC simulations match almost exactly with that of the PIC simulation.

In this dissertation we will rely on the multiparticle Monte Carlo simulation model to study the single surface multipactor discharge.

CHAPTER 3: Time Dependent Physics of Single Surface Multipactor with Two-Frequency RF Fields

In this Chapter, we present a detailed analysis of the time-dependent physics [125] of multipactor discharge on a single dielectric surface with a transverse rf electric field of two carrier frequencies $E_y = [E_{rf} \sin(\omega t + \theta) + \beta E_{rf} \sin(n(\omega t + \theta) + \gamma)]$. We employ the multiparticle Monte Carlo simulation model presented in the Chapter 2 to analyze the temporal profiles of the secondary electron yield and the normal surface charging electric field. Next, we present the time averaged multipactor susceptibility diagrams for two frequency rf fields. We discuss the effect of the relative strength and phase of the second carrier mode on multipactor electron trajectories and examine the phase space evolution of multipactor electrons. Effect of frequency ratio on the time dependent physics is described in the last section of the Chapter [125]. This Chapter contains figures and excerpts from [125] which have been reproduced with permission from American Physical Society.

3.1. Time Dependent Electric Fields and Secondary Electron Yield

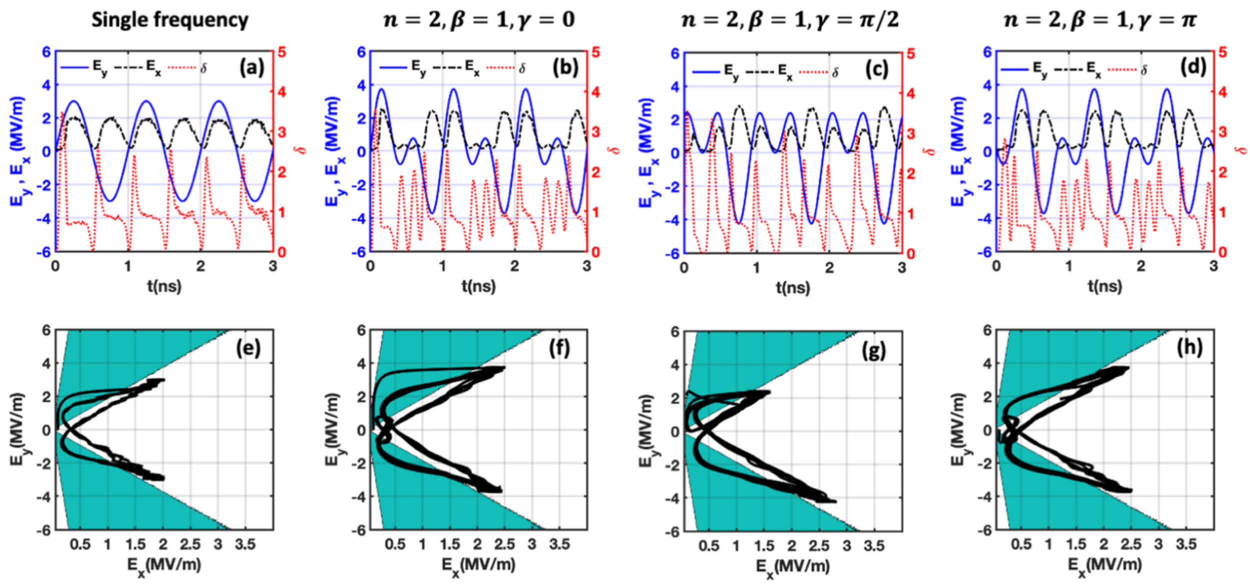

Figure 3.1. Top row: Instantaneous rf electric field, E_y (solid blue lines), normal electric field, E_x (broken black lines), and secondary electron yield, δ (dotted red lines), for (a) single frequency rf field, $\beta = 0$, (b) two carrier frequencies of the rf field with frequency ratio $n = 2$, relative strength of the second carrier frequency, $\beta = 1$, and initial relative phase of the second carrier frequency, $\gamma = 0$, (c) two carrier modes with $n = 2, \beta = 1, \gamma = \pi/2$, and (d) two carrier modes with $n = 2, \beta = 1, \gamma_0 = \pi$. Bottom row: The corresponding plots of trajectories of the electric field $(E_x(t), E_y(t))$. The cyan region is the multiapctor susceptibility region obtained by applying constant electric field, $E_{y,dc}$, parallel to the surface [73,123,127]. In (a) – (d), the average secondary electron yield $\delta_{avg} = 1$ in the saturation regime. In all the calculations, we set $f_{rf} = 1GHz$. For the single frequency case, we set $E_{rf} = 3MV/m$, and for the cases with two carrier frequencies, we set $E_{rf} = 3/\sqrt{2}\ MV/m$.

With the addition of the second carrier mode, the overall rf electric field will become periodically modulated, which is expected to distort the electrons' trajectory, leading to modified multipactor dynamics [123]. Figure 3.1 shows the temporal profiles of the rf signal, E_y (solid blue lines), secondary electron yield, δ (dotted red lines), and normal electric field, E_x, (broken black lines) for two-frequency excitations with various γ, and with fixed $n = 2$, $\beta = 1$, and $f_{rf} = 1GHz$. In Fig. 3.1(a), the single frequency rf signal E_y with amplitude $E_{rf,single} = 3MV/m$ produces the secondary electron yield δ and the normal electric field E_x that oscillate at twice the rf frequency as shown previously by Kim and Verboncoeur [73]. Figures 3.1(b)-(d) show the same plots for two-frequency rf signals. Individual carrier amplitudes of the two-frequency signals in Figs. 3.1(b)-(d) are chosen as $E_{rf,dual} = E_{rf,rms,single} = 3/\sqrt{2}\ MV/m$ so that the average rf power of a two-frequency signal is equal to the average rf power of the single-frequency signal. Figures 3.1(e)-(h) show the closed Lissajous curves for the field configurations of Figs. 3.1(a)-(d) respectively, describing the temporal relationship between the fields normal (E_x) and parallel (E_y) to the surface. The cyan region in the Lissajous curves indicates the parameter regime where the multipactor discharge grows. When both components of the electric field (E_x, E_y) are in this cyan regime, it is expected that the number of electrons N_s grows due to multipaction and the normal electric field E_x increases. Otherwise, the normal electric field E_x and hence the multipactor electron population N_s decrease. Careful examination of the temporal profiles shows that there is a slight overshoot when crossing the boundaries: the growth continues for a short time after the curve exits the cyan region, and likewise, decay continues for a short time after the curve enters the cyan region. This overshoot might be the result of the inertia of particles.

We find in Fig. 3.1(b) that when $n = 2, \beta = 1$, and $\gamma = 0$ the temporal profiles of the secondary electron yield δ and normal electric field E_x oscillate at four times the rf frequency [123] and consequently there are two large loops and two small loops in the closed Lissajous curve of Fig. 3.1(f). In Fig. 3.1(c), the temporal profiles of δ and E_x oscillate at three times the rf frequency for $\gamma = \pi/2$. As a result, there are two relatively small loops and one relatively large loop in the closed Lissajous curve of Fig. 3.1(g), resulting in a periodic asymmetry of electric field conditions in the horizontal y-direction. Figures 3.1(d) and 3.1(h) show the temporal profiles of E_y, δ, E_x and the corresponding closed Lissajous curve respectively, for $\gamma = \pi$. It is noteworthy that the rf fields (E_y) for $\gamma = 0$ and $\gamma = \pi$ are similar but acting in opposite directions. Therefore, the temporal profiles of δ and E_x in Fig. 3.1(d) have similar oscillation patterns to those of Fig. 3.1(b), so are for the Lissajous curves in Figs. 3.1(h) and 3.1(f).

By interpolating the values of E_y where the Lissajous curves cross the susceptibility boundaries and substituting these values in $E_y = [E_{rf}\sin(\omega t + \theta) + \beta E_{rf}\sin(n(\omega t + \theta) + \gamma)]$ for Figs. 3.1(e)- (h), we can determine the corresponding values of time t and quantify the amount of time in a period spent by the electric fields in the growth regime (cyan region of the susceptibility diagram) and in the decay regime (white region of the susceptibility diagram). We also compare the time averaged normal electric fields due to surface charging, corresponding to the multipactor strengths in the system, for the single- and two-frequency operations. The results are summarized in Table 3.1.

rf field configuration		**Percentage of time spent in growth (decay) regime during one rf period ($\mathbf{1}\boldsymbol{ns}$) of the fundamental frequency**		**Time averaged normal electric field $\boldsymbol{E_x}$ (MV/m)**
		in large loops	**in small loops**	
Single frequency		20% (80%)	0% (0%)	0.9
Two-frequency	$\boldsymbol{n = 2, \beta = 1, \gamma = 0}$	13% (54%)	17% (16%)	0.756
	$\boldsymbol{n = 2, \beta = 1, \gamma = \pi/2}$	8% (25%)	21% (46%)	0.775
	$\boldsymbol{n = 2, \beta = 1, \gamma = \pi}$	13% (54%)	17% (16%)	0.75

Table 3.1. Time spent by the electric fields in the growth and decay regions and the time averaged normal electric field values for different rf field configurations obtained from the temporal investigation of Fig. 3.1.

Note that for the two-frequency cases, the time in the growth regime in the small loops are relatively long, where the growth rate is low, resulting in a relatively small multipactor electron population during this time interval. In contrast, the time spent in the growth regime of the large loops in these cases are much shorter than that of the single frequency case. The time averaged normal electric field in the two-frequency cases (< 0.78MV/m), corresponding to the multipactor strength in the system, are reduced from that of the single frequency case (~0.9MV/m) for the same rf power.

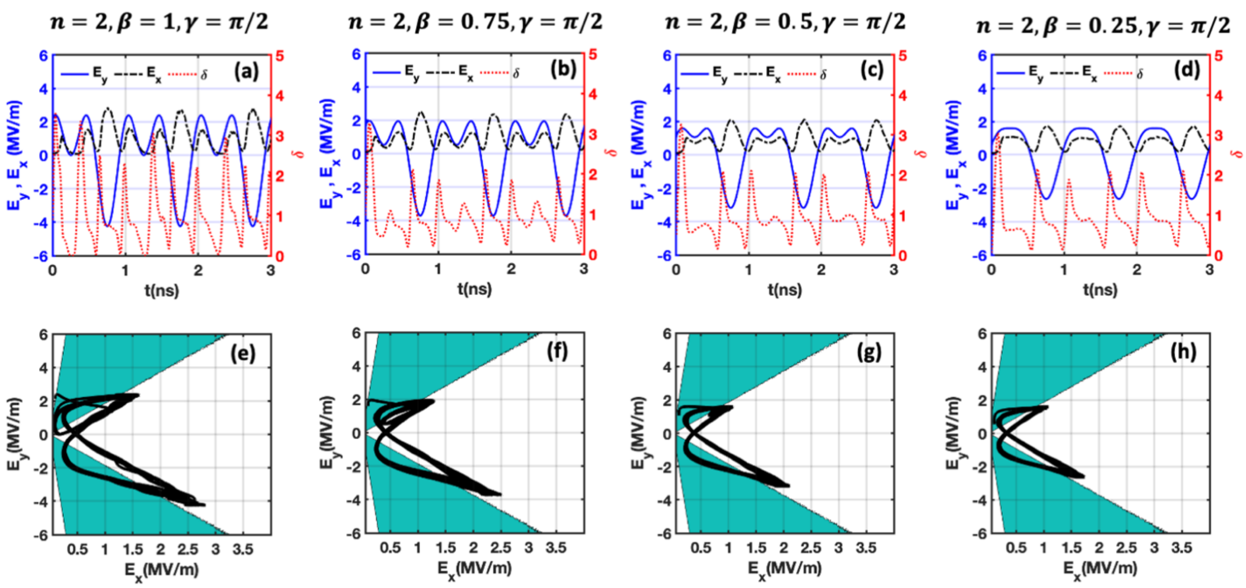

Figure 3.2. Top row: Instantaneous rf electric field, E_y (solid blue lines), normal electric field, E_x (broken black lines), and secondary electron yield, δ (dotted red lines), for two-frequency cases with frequency ratio $n = 2$, initial relative phase of the second carrier frequency, $\gamma = \pi/2$, and relative strength of the second carrier frequency, (a) $\beta = 1$, (b) $\beta = 0.75$, (c) $\beta = 0.5$, and (d) $\beta = 0.25$. Bottom row: The corresponding plots of trajectories of the electric field $(E_x(t), E_y(t))$. The cyan region is the multiapctor susceptibility region obtained by applying constant electric field, $E_{y,dc}$, parallel to the surface [73,123,127]. In (a) – (d), the average secondary electron yield $\delta_{avg} = 1$ in the saturation regime. In all the calculations, we set $f_{rf} =$ 1GHz and $E_{rf} = 3/\sqrt{2}$ MV/m.

Figure 3.2 shows temporal profiles of the rf signal, E_y (solid blue lines), secondary electron yield, δ (dotted red lines), and normal electric field, E_x, (broken black lines) for $n = 2$ and $\gamma = \pi/2$, when the relative strength β decreases from $1, 0.75, 0.5$ to 0.25. As β decreases from Fig. 3.2(a)-(d), the oscillation in the temporal profiles of E_x and δ gradually transfers from three times of the rf frequency to twice of the rf frequency. The third loop in the closed lissajous curve gradually disappears from Fig. 3.2(e)-(h) and two loops remain, resembling the single frequency case. This is consistent with the results of Iqbal *et al.* [40] that the effect of the second carrier mode on the multipactor susceptibility becomes less prominent as the relative strength of the second carrier mode decreases.

3.2. Time Averaged Multipactor Susceptibility

To calculate the multipactor susceptibility diagram, we use the multiparticle MC model described in Chapter 2, but keep the normal electric field E_x fixed at its input value throughout the simulation [4,5,40]. The average value of secondary electron yield over n_i impacts (or iterations) is calculated as $\bar{\delta} = (\delta_1 . \delta_2 \dots \delta_n)^{1/n_i}$, where a large n_i is used in the calculation ($n_i \sim 80000$ impacts for $N = 200$ macroparticles here) to estimate the $\bar{\delta}$ over a time duration corresponding to integer multiple of an rf period. This average value $\bar{\delta}$ represents either a growing ($\overline{\delta} > 1$) or decaying ($\overline{\delta} < 1$) trend in the number of electrons in the avalanche, which depends on the input parameters, E_x, E_{rf}, δ_{max0}, n, β, and γ. The boundaries of the multipactor susceptibility are determined where $\overline{\delta} = 1$.

For a two-carrier electric field, $E_y = [E_{rf} \sin(\omega t + \theta) + \beta E_{rf} \sin(n(\omega t + \theta) + \gamma)]$, During the early stage of multipactor discharge if the frequency ratio of the two carriers, $n,$ is very close to unity, the evolution of relative phase is very slow with time. In this case, we can assume that relative phase remains constant with time in the Monte Carlo simulation, as described in section 2.4 as well as in Ref [40]. In contrast, when the frequency ratio n is not close to unity, the relative phase evolves quickly with time, which has to be self-consistently considered in the Monte Carlo simulation. In this case, the relative phase evolves self-consistently as $(n-1)\theta_{i+1} + \gamma$ at each iteration, where i is iteration index.

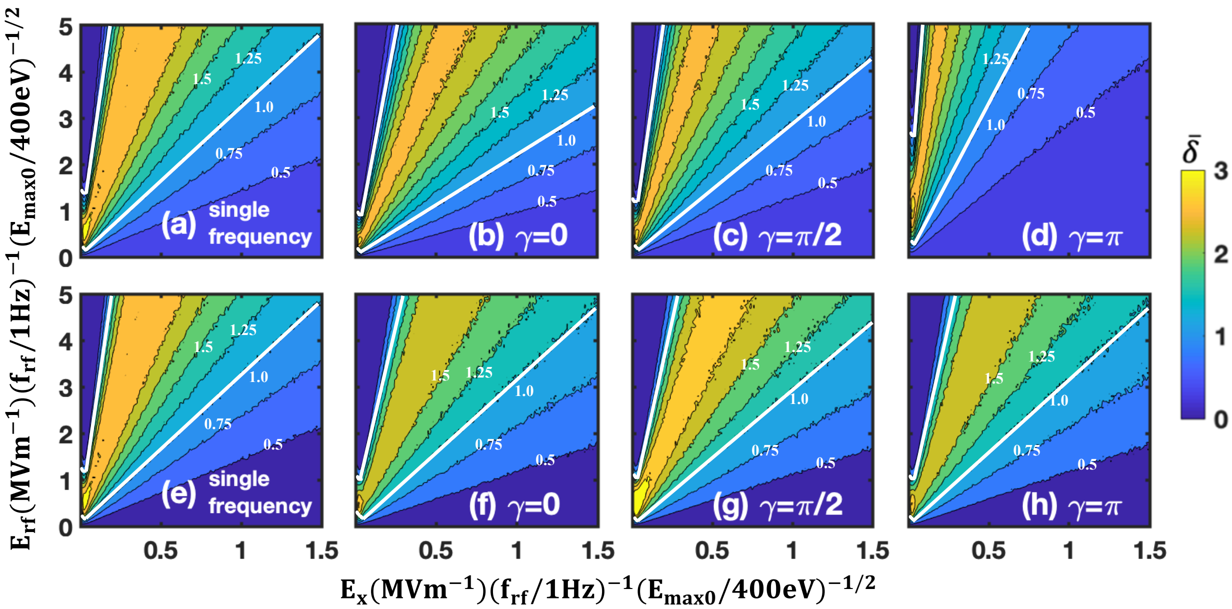

Figure 3.3. Multipactor susceptibility with two carrier frequencies of the rf field from MC simulation for different γ in Eq. (2.1), for $\delta_{max0} = 3, E_{0m}/E_{max0} = 0.005$, relative frequency of the second carrier, $n = 2$, and relative strength of the second carrier, $\beta = 1$. Top row: the relative phase is kept fixed at the initial value; bottom row: the relative phase evolves with time.

Figure 3.3 shows the comparison of the two-frequency fields induced multipactor susceptibility diagrams with constant relative phase of the two carriers as in Ref [40], and with evolving relative phase, for $n = 2$ and $\beta = 1$. For the cases of constant relative phase in Figs. 3.3(a)-(d), the slopes of both upper and lower susceptibility boundaries increase significantly, as γ increases from 0 to π [40]. However, for the cases of relative phase evolving with time in Figs. 3.3(e)-(h), the slope of the lower susceptibility boundary decreases slightly as γ increases from 0 to $\pi/2$ and then increases again with $\gamma = \pi$, while the upper susceptibility boundary remains almost unaffected by the change of γ. While Ref [40] concludes that the presence of a second carrier mode can change the multipactor susceptibility boundaries, with the highest threshold achieved at $\gamma = \pi$, our study here shows that the effect of γ on the susceptibility boundaries is not prominent when the relative phase between the two carriers evolves over time.

Note that the assumption of constant relative phase of the second carrier in Iqbal *et al.* [40] is reasonable during the early stage of multipactor discharge if the frequency ratio of the two carriers, n, is very close to unity and therefore the evolution of relative phase is slow with time. When the frequency ratio n is not close to unity, the relative phase evolves quickly with time, which has to be self-consistently considered, as in Figs. 3.3(e) – (h) from our multiparticle MC model.

For a given rf field E_{rf}, we can estimate the saturation levels of the normal electric field, E_x, at the lower susceptibility boundaries of the single- and two-frequency susceptibility diagrams of Figs. 3.3(e)-(h). For the single frequency case, the saturation level of E_x estimated from the susceptibility diagram of Fig. 3.3(e) is about $0.9\mathrm{MV/m}$ with $E_{rf,single} = 3\mathrm{MV/m}$. For the two-frequency cases with $E_{rf,dual} = 3/\sqrt{2}\ \mathrm{MV/m}$ for the same input power as of the single frequency case, the saturation levels of E_x estimated from the susceptibility diagrams of Figs. 3.3(f)-(h) are about $0.73\mathrm{MV/m}$, $0.76\mathrm{MV/m}$, and $0.73\mathrm{MV/m}$ respectively. These values are in excellent agreement with the values obtained from our temporal investigation shown in Table 3.1 above.

3.3. Multipactor Electron Trajectories

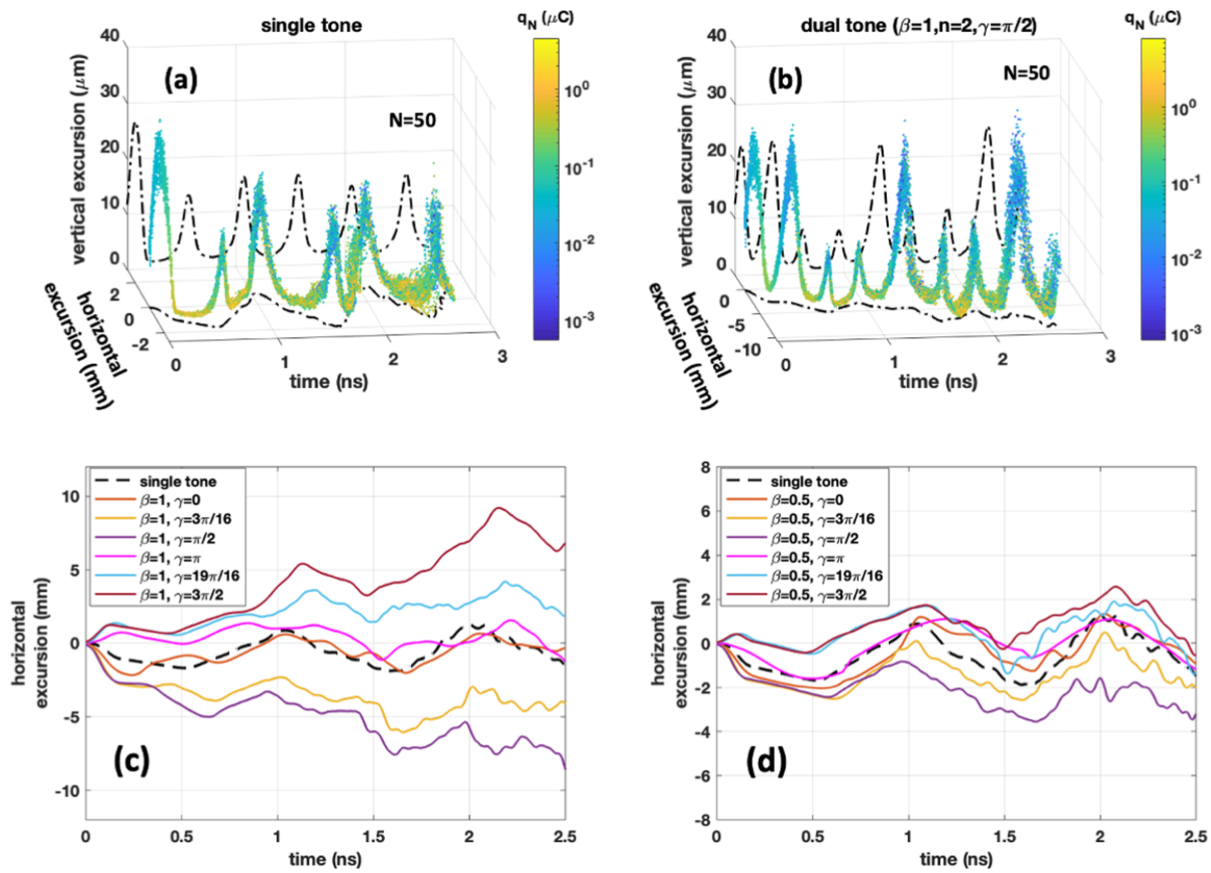

Figure 3.4. Top row: Horizontal (along the dielectric surface) and vertical (normal to the surface) excursions of $N = 50$ multipacting macroparticles with respect to time, for (a) single-frequency rf electric field with $f_{rf} = 1\text{GHz}$, and (b) two-frequency rf electric field with $f_{rf} = 1\text{GHz}, \theta = 0$, $\beta = 1, n = 2, \gamma = \pi/2$. Charge contained in the macroparticles are shown in the color bar. Mean displacements of the macroparticles with respect to time are shown as projections on the horizontal and vertical planes. Bottom row: Comparison of the mean horizontal displacements for the single- and two-frequency rf electric fields with $f_{rf} = 1\text{GHz}, \theta = 0, n = 2$, and $\gamma = 0, 3\pi/16, \pi/2, 19\pi/16, 3\pi/2$, for (c) $\beta = 1$ and (d) $\beta = 0.5$.

We have examined the multipacting particle trajectories for different rf field configurations when a second carrier mode is present in the rf field, as shown in Figs. 3.4(a) and 3.4(b). In our simulation, the vertical and horizontal excursions, controlled by the normal and parallel electric fields respectively, of $N = 50$ macroparticles are monitored over time. The charge contained in the macroparticles is shown in the color bar on the right side of each plot. For charge neutrality, the total charge contained in the macroparticles is equal to the total surface charge N_s, which corresponds to the normal electric field E_x at x = 0. In both plots of Figs. 3.4(a) and (b), as the normal electric field (or total surface charge N_s) increases, the particles are drawn close to the surface and consequently their vertical excursions are small. During this period, their flight times are reduced, and they impact the surface with less energy. As a result, the SEY drops (see Fig. 3.1(a)-(b)) and the normal electric field grows weaker. When the normal electric field is weak, the macroparticles containing less charge than before make farther excursions from the surface. Their flight times increase, allowing them to gain more energy from the rf electric fields, which consequently increases the SEY of the impacts (Fig. 3.1(a)-(b)). As a result, the normal electric field increases again and brings the trajectories of the particles closer to the surface. This process continues periodically, at twice the rf frequency for the single frequency operation in Fig. 3.4(a), and at three times the fundamental rf frequency for the two-frequency operation with $\beta = 1, n = 2,$ and $\gamma = \pi/2$ in Fig. 3.4(b).

The horizontal excursions of the particles depend on the rf electric field acting parallel to the surface. The macroparticles, containing negatively charged electrons, accelerate in the opposite direction of the rf electric field. For the single frequency case, the rf field has periodic symmetry in the positive and negative y-directions. Therefore, the horizontal excursion of the particles during the positive half cycle of the rf period is compensated during the negative half cycle of the rf period and the mean horizontal displacement of the particles is almost negligible over the complete rf period, as evident from Fig. 3.4(a). However, for the two-frequency case, the periodic symmetry of the rf field in the y-direction is typically not present, as seen from Figs. 3.1(b)-(d) and 3.2(b)-(d). During an rf period of 1 ns of the fundamental mode carrier for $\beta = 1, n = 2,$ and $\gamma = \pi/2$, the rf field acts in the $+y$ direction for roughly 0.67ns and in the $-y$ direction for roughly 0.33ns.

Due to the periodic asymmetry of the rf field, a mean horizontal excursion of the negative charges in the -y direction in one rf period of the fundamental carrier is observed, as shown in Fig. 3.4(b).

The mean horizontal displacements with time for various two-frequency fields are summarized in Figs. 3.4(c)-(d). Figure 3.4(c) shows that for three cases: the single frequency field (dashed black line), i.e., $\beta = 0$, as well as for the two-frequency rf fields with $\beta = 1, n = 2,$ and $\gamma = 0$ (solid red line) and π (solid magenta line), the mean horizontal displacement of the macroparticles is almost negligible over the complete rf period. This is due to the periodic symmetry of the rf electric fields, as shown in Figs. 3.1(a)-(b) and (d). For $0 < \gamma < \pi$, the periodic asymmetry of the rf field causes a mean horizontal displacement of the macroparticles in the $-y$ direction and the maximum horizontal displacement occurs for $\gamma = \pi/2$. On the other hand, for $\pi < \gamma < 2\pi$, the periodic asymmetry of the rf field causes a mean horizontal displacement of the macroparticles in the $+y$ direction and the maximum horizontal displacement occurs for $\gamma = 3\pi/2$. When the relative strength of the second carrier mode is lower, i.e. $\beta = 0.5$ in Fig. 3.4(d), the magnitudes of the mean horizontal displacement of the macroparticles decrease compared to those of $\beta = 1$. However, the directions of the mean horizontal displacements for $0 < \gamma < \pi$ and $\pi < \gamma < 2\pi$ remain the same for both $\beta = 1$ and $\beta = 0.5$. Therefore, we can summarize that the magnitude and the direction of the mean horizontal displacement of the macroparticles depend on the relative strength, β, and initial relative phase, γ, of the second harmonic carrier mode, respectively. This capability of migrating multipactor trajectories has been referred to as the steerability-to-zero criterion [121] and it can be of interest to rf system operators in applications such as cleaning a given location in a structure to reduce further susceptibility to multipactor, or for directing multipacting electrons to a specific desirable location in the geometry [121].

3.4. Multipactor Electron Phase Spaces

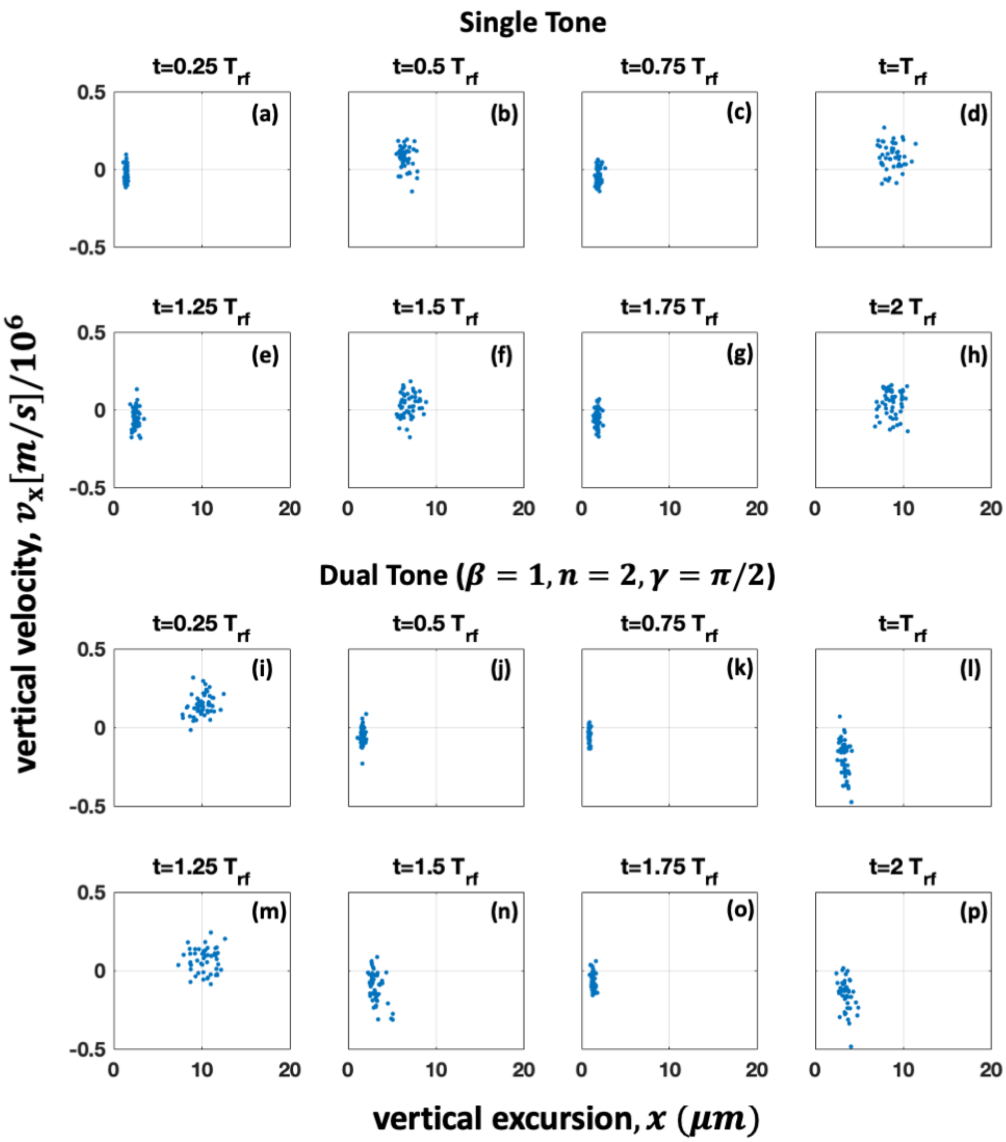

Figure 3.5. Top two rows: v_x vs x for the single frequency case at times (a) $t = 0.25T_{rf}$, (b) $t = 0.5T_{rf}$, (c) $t = 0.75T_{rf}$, (d) $t = T_{rf}$, (e) $t = 1.25T_{rf}$, (f) $t = 1.5T_{rf}$, (g) $t = 1.75T_{rf}$, (h) $t = 2T_{rf}$, where $T_{rf} = 1\text{ns}$ is the rf period. Bottom two rows: (i)-(p) v_x vs x for the two-frequency case with $\beta = 1, n = 2$, and $\gamma = \pi/2$ at the same times as (a)-(h) respectively.

Figures 3.5 and 3.6 show the velocity-position phase space of $N = 50$ macroparticles during two rf periods in the vertical and horizontal directions respectively, for both single-frequency and two-frequency operation. In the $x - v_x$ phase space in Fig. 3.5, there is a periodic bunching and de-bunching of the macroparticles within an rf period. This happens because in our simulation, secondary macroparticles emitted from the $x = 0$ position are assigned random emission velocities in the $+x$ direction and the normal electric field E_x always acts in the $-x$ direction. When the normal field E_x is weak (e.g. $t = 0.5T_{rf}$, T_{rf} for single frequency operation, cf. Fig. 3.1(a); and $t = 0.25T_{rf}$ for two-frequency operation, cf. Fig. 3.1(c)), the randomness of emission velocities results in a larger span of vertical positions of the macroparticles, and the vertical excursions of the macroparticles are large. However, when the normal field E_x is very strong (e.g. $t = 0.25T_{rf}$, $0.75T_{rf}$ for single frequency operation, cf. Fig. 3.1(a); and $t = 0.75T_{rf}$ for two-frequency operation, cf. Fig. 3.1(c)), it exerts more force and causes the macroparticles to stay closer to the surface, reducing the effect of the randomness of their emission velocities and resulting in a bunching effect in the $x - v_x$ phase space. The periodicity of bunching and de-bunching of the macroparticles in the phase space results from the periodic increase and decrease of the strength of the normal electric field. Note that including the space charge shielding in the model would increase the distribution in vertical positions, since the most distant particles would see a weaker restoring field than the particles closer to the surface.

In contrast to Fig. 3.5, we observe in Fig. 3.6 a gradual de-bunching effect taking place in the horizontal velocity-position $y - v_y$ phase space. This is because the horizontal displacement is determined by the rf electric field that not only changes in strength but also changes in direction periodically. The emitted secondary macroparticles are assigned random emission angles uniformly distributed in the range of $[0, \pi]$. Therefore, the directions of emission velocities of the macroparticles may be the same as or opposite to that of the rf field, causing a dispersion in the $y - v_y$ phase space. This span increases with time as new generations of secondary macroparticles are emitted from different y-locations and their emission velocities and emission angles add more randomness to the phase space.

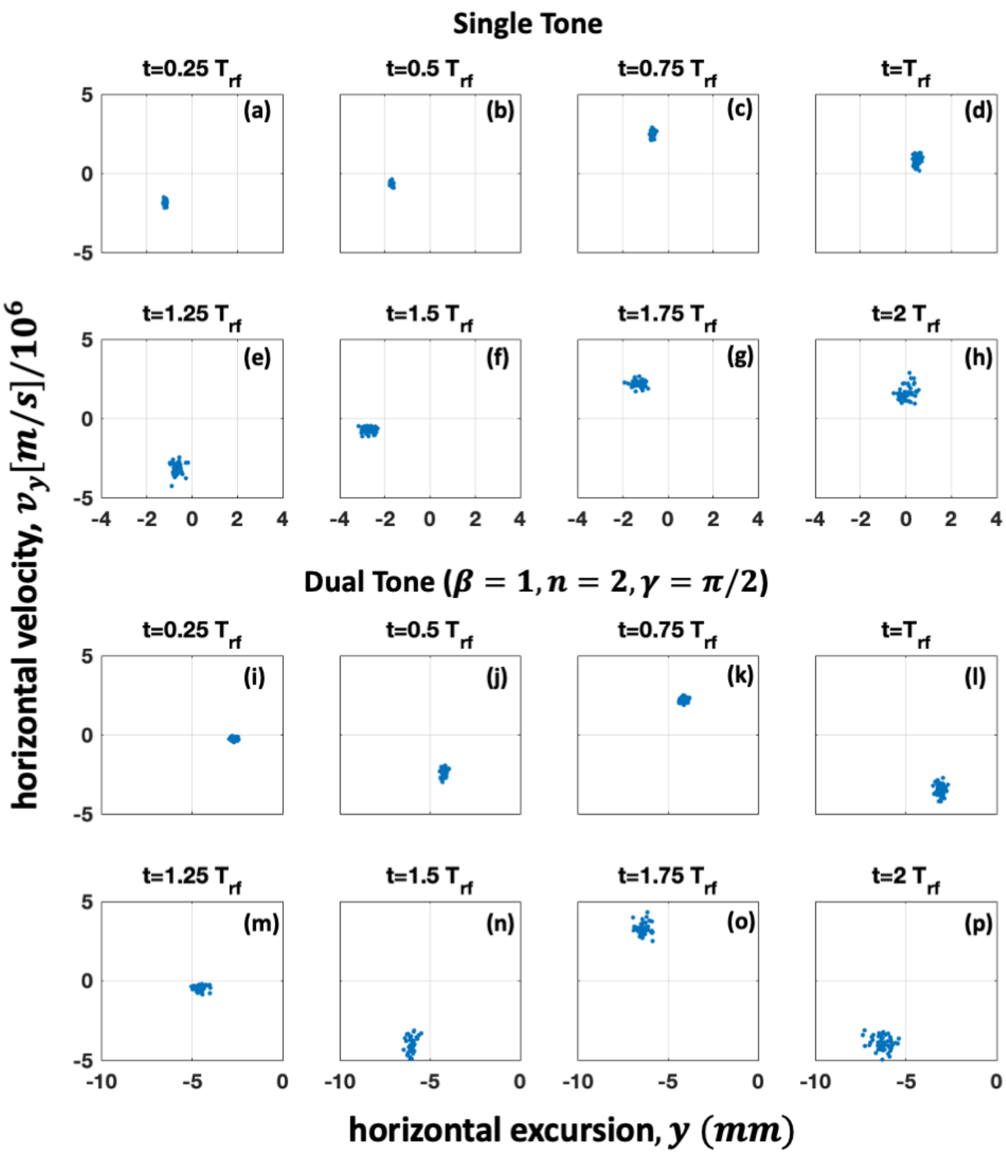

Figure 3.6. Top two rows: v_y vs y for the single frequency case at times (a) $t = 0.25T_{rf}$, (b) $t = 0.5T_{rf}$, (c) $t = 0.75T_{rf}$, (d) $t = T_{rf}$, (e) $t = 1.25T_{rf}$, (f) $t = 1.5T_{rf}$, (g) $t = 1.75T_{rf}$, (h) $t = 2T_{rf}$, where $T_{rf} = 1ns$ is the rf period. Bottom two rows: (i)-(p) v_y vs y for the two-frequency case with $\beta = 1, n = 2$, and $\gamma = \pi/2$ at the same times as (a)-(h) respectively.

Another important observation of Fig. 3.6 is the migration of multipactor trajectories for the dual-frequency operation. For the single frequency case, the velocities of the macroparticles are in the $-y$ direction during the positive half cycle of the rf-period (Fig. 3.6(a)-(b)), and in the $+y$ direction during the negative half cycle of the rf-period (Fig. 3.6(c)-(d)). The macroparticles do not have obvious net horizontal displacement due to this symmetry in the direction of velocities within a period. However, for the two-frequency case, the velocities of the macroparticles are in the $-y$ direction during most of the rf cycle (Figs. 3.6(i), 3.6(j), and 3.6(l)). As a result, there is a net horizontal displacement of the particles in the $-y$ direction, which is consistent with Fig. 3.4(c).

3.5. Effect of Frequency Separation

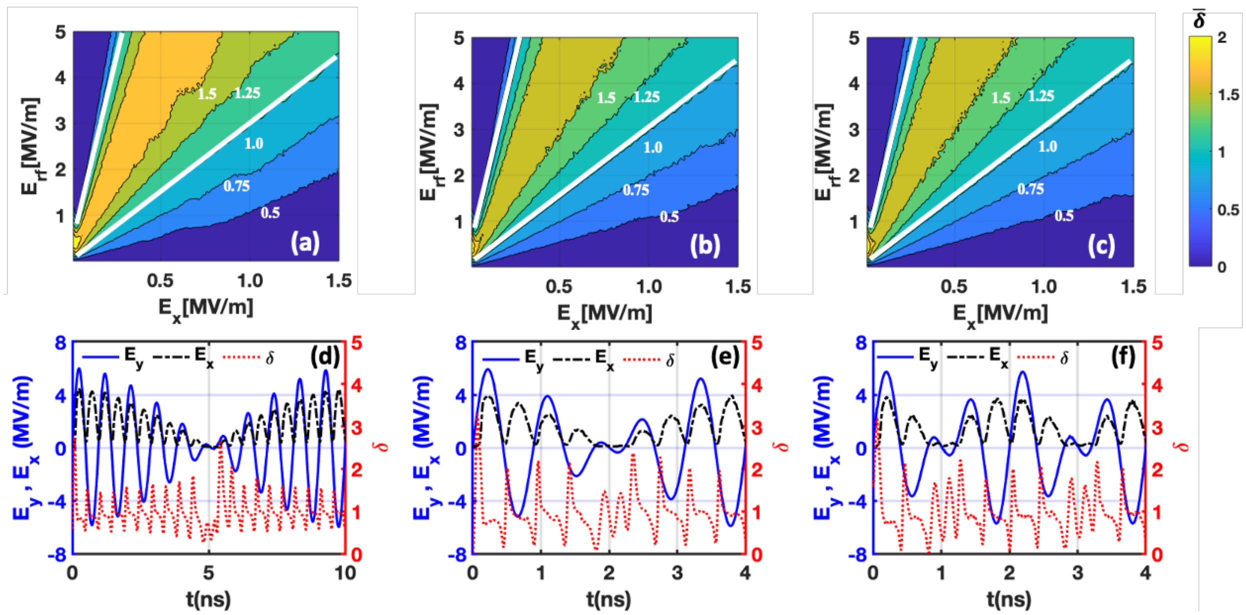

Figure 3.7. Top row: Multipactor susceptibility diagrams for two-frequency rf fields with frequencies, (a) $f_1 = 1GHz$ and $f_2 = 1.1GHz$, (b) $f_1 = 1GHz$ and $f_2 = 1.25GHz$, and (c) $f_1 = 1GHz$ and $f_2 = 1.5Hz$. Bottom row: (d)-(f): The instantaneous rf electric field, E_y (solid blue lines), normal electric field, E_x (broken black lines), and secondary electron yield, δ (dotted red lines) for rf field configurations of plots (a)-(c) respectively. In (d) – (f), the average secondary electron yield $\delta_{avg} = 1$ in the saturation regime. In all the calculations, we set $E_{rf} = 3MV/m$, $\gamma = 0$, and $\beta = 1$.

Figure 3.7 shows the two-frequency susceptibility diagrams and temporal profiles of E_y, E_x, and δ for three cases with non-integer frequency ratio. The first, second, and third column shows the results for the case with $f_1 = 1$GHz and $f_2 = 1.1$GHz, $f_2 = 1.25$GHz, and $f_2 = 1.5$GHz, respectively. Figures 3.7(a)-(c) have little difference, showing that multipactor susceptibility is relatively insensitive to the frequency separation, which is consistent with previous results in [40].

The reason for this insensitivity can be inferred from the temporal profiles of E_y and E_x in Figs. 3.7(d)-(f). Due to the frequency separation the rf envelopes for the three cases are different. However, for the given $E_{rf} = 3$ MV/m, the time averaged values of the resulting normal electric fields are almost the same, being $1.02\ \mathrm{MV/m}$ for Fig. 3.7(a), $1.03\mathrm{MV/m}$ for Fig. 3.7(b) and $1.03\mathrm{MV/m}$ for Fig. 3.7(c), respectively. From the susceptibility diagrams of Fig. 3.7(a)-(c), the saturation levels for the three cases are estimated to be ~$1.0\mathrm{MV/m}$, ~$1.0\mathrm{MV/m}$, and ~$1.01\mathrm{MV/m}$, respectively.

The periodic beating of the rf electric field E_y produces a beat wave in the temporal profiles of the normal surface charging electric field E_x. The beat frequency of such waves depends on the frequency separation, $\Delta f = f_2 - f_1$. The three representative cases with frequency separation of $100\mathrm{MHz}$, $250\mathrm{MHz}$, and $500\mathrm{MHz}$ have beat wave periods of $10\mathrm{ns}$, $4\mathrm{ns}$, and $2\mathrm{ns}$ respectively. It is evident that multiple frequency components are present in the temporal profiles of the normal electric fields. These frequency components of the normal electric fields are analyzed through the frequency domain analysis of single surface multipactor [124], which will be discussed in Chapter 4 in details.

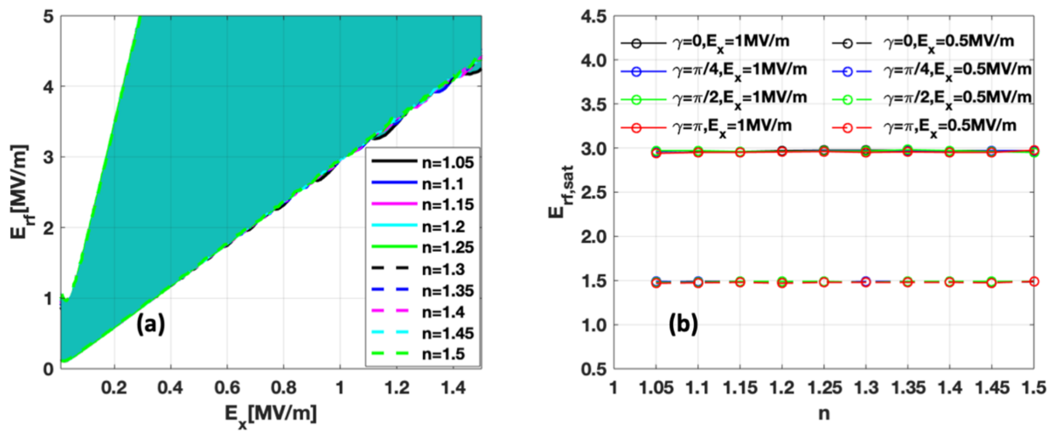

Figure 3.8. (a) Multipactor susceptibility diagrams for two-frequency rf fields with $\beta = 1, \gamma = 0$, and frequency ratio $1.05 \leq n \leq 1.5$. The cyan region shows the parameter regime where the multipactor discharge develops. The upper and lower susceptibility boundaries for different frequency ratio n are largely overlaid with one another. (b) rf carrier amplitude at the lower susceptibility boundary in ac saturation state, $E_{rf,sat}$, for two-frequency rf operation with $\beta = 1$, $\gamma = 0, \pi/4, \pi/2$, and π for time averaged saturation values of the normal electric field, $E_x = 0.5\text{MV/m}$ (dashed lines) and 1.0MV/m(solid lines). For a fixed value of E_x (0.5MV/m or 1MV/m), the E_{rf} vs n plots corresponding to different values of γ are overlaid with one another.

The insensitivity of multipactor susceptibility to the frequency separation of the two carrier modes is evident from Figure 3.8. In Fig. 3.8(a), we observe that when the relative strength and phase of the second carrier mode is kept fixed at $\beta = 1$ and $\gamma = 0$ respectively, and the frequency ratio changes from $n = 1.05$ to $n = 1.5$, the two-frequency multipactor susceptibility boundaries remain almost unchanged. Figure 3.8(b) shows that for a fixed time averaged saturation value of the normal electric field E_x, the rf carrier amplitude at the lower susceptibility boundary in ac saturation state, $E_{rf,sat}$, is insensitive to the frequency ratio n as well as to the relative phase of the second carrier mode γ. When $E_x = 0.5\text{MV/m}$ (dashed lines in Fig. 3.8(b)), for frequency ratio, $1.05 \leq n \leq 1.50$, and relative phase of the second carrier mode, $0 \leq \gamma \leq \pi$, the rf carrier amplitude in ac saturation is found to be $E_{rf,sat}$~1.49MV/m. When E_x in increased to $E_x = 1.0\text{MV/m}$ (solid lines in Fig. 3.8(b)), the $E_{rf,sat}$ increases to $E_{rf,sat}$~2.98MV/m, remaining insensitive to both n and γ. These results have been spot checked against one dimensional Particle-in-cell (PIC) simulations.

CHAPTER 4: Frequency Domain Analysis of Single Surface Multipactor

As mentioned in Chapter 1, the frequency domain analysis of multipactor discharge is important to understand the effect of multipactor on device operations. In this chapter, we examine multipactor discharge in the frequency domain on a single dielectric surface with single- and two-frequency rf fields [124]. This Chapter contains figures and excerpts from [124] which have been reproduced with permission from IEEE.

We employ the multiparticle Monte Carlo (MC) simulation model [123] to obtain the temporal profiles of the normal electric field to the surface that corresponds to the multipactor strength in the system. We then employ Fast Fourier Transform (FFT) algorithm using MATLAB to obtain the Discrete Fourier Transform (DFT) (also called the amplitude spectrum) of the temporal profiles of the normal electric field E_x in the ac saturation state.

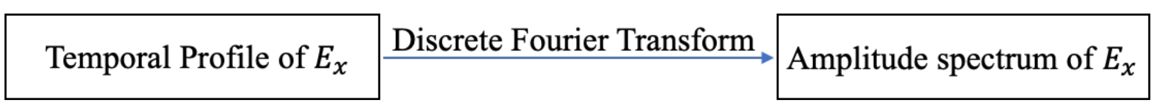

4.1. Analysis for Single Frequency RF field Induced Multipactor

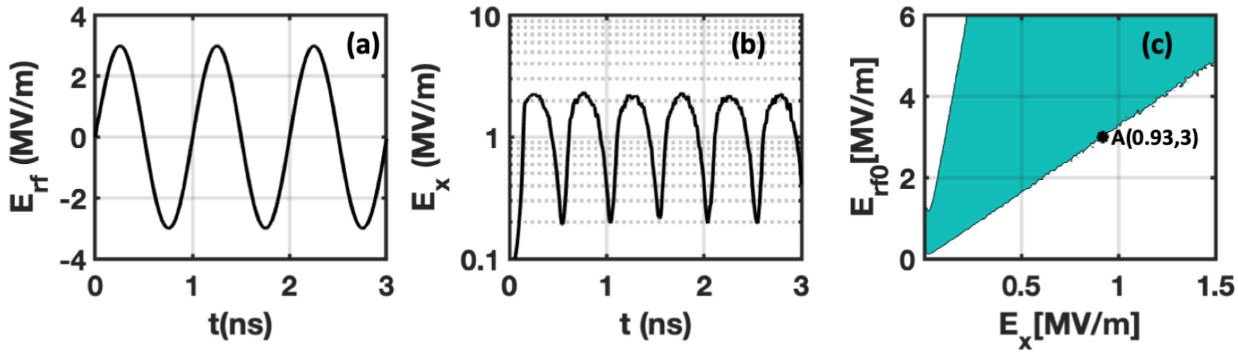

Figure 4.1. (a) Temporal profile of the rf field with frequency $f_{rf} = 1\text{GHz}$ and amplitude $E_{rf0} = 3\text{MV/m}$. (b) Temporal profile of the normal electric field E_x in the ac saturation state obtained from the MC simulation. (c) Multipactor susceptibility boundaries (cyan region is subject to multipactor susceptibility) in the (E_x, E_{rf0}) plane from Monte Carlo simulation with single frequency rf field. Here, the maximum secondary electron yield, $\delta_{max0} = 3$, occurring at impact energy $E_{max0} = 420\text{eV}$, and $E_{0\text{m}}/E_{max0} = 0.005$, where $2E_{0\text{m}}$ is the average emission energy of secondary electrons. In the calculation of (c), E_x is kept as a constant for each case, and the susceptibility is recorded when $\delta_{avg} > 1$.

Previous studies conducted by Kim and Verboncoeur [73] and Iqbal *et al.* [123] showed that for a single frequency rf electric field (Fig. 4.1(a)), the temporal profile of the normal electric field E_x oscillates at twice the rf frequency in the ac saturation state (Figure 4.1(b)). It is also understood [4,40,123] that the ac saturation for a given rf amplitude occurs at the lower multipactor susceptibility boundary, as shown in Fig. 4.1(c). For instance, for the rf amplitude $E_{rf0} = 3\text{MV/m}$ of Fig. 3(a), the ac saturation occurs at point "*A*" in Fig. 4.1(c) where the time averaged normal electric field is $E_x = 0.93\text{MV/m}$. This is very close to the time averaged value of 0.9 MV/m obtained from Fig. 4.1(b). It is evident from Fig 4.1(b) that the oscillation in the normal electric field profile is not purely sinusoidal and thus is expected to have multiple frequency components. We employ DFT to obtain the amplitude spectrum of the normal electric field E_x and observe its frequency components for different rf amplitudes and frequencies.

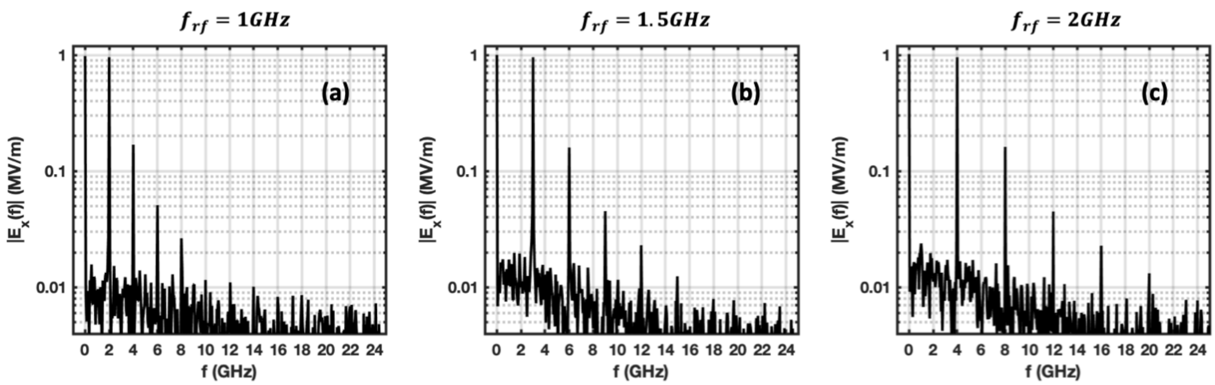

Figure 4.2. Amplitude spectrum of the normal electric field in the ac saturation state induced by a single frequency rf field with amplitude, $E_{rf0} = 3\text{MV/m}$ and frequencies f_{rf} = (a) 1GHz, (b) 1.5GHz, and (c) 2GHz. Pronounced spectral peaks are observed at even harmonics of the rf frequency in each case. The heights of the spectral peaks are independent of the rf frequency.

Figure 4.2 shows the amplitude spectrum of the normal electric field E_x for three different cases of a single frequency rf field. The rf amplitude is kept fixed at $E_{rf0} = 3\text{MV/m}$ and the rf frequency is varied as $f_{rf} = 1G$Hz, 1.5GHz, and 2GHz from Figs. 4.2(a)-(c) respectively.

As shown in Fig. 4.2, the peaks in the amplitude spectrum of E_x appear at even harmonics of the rf frequency, $2lf_{rf}$, where l is a positive integer. We also observe that the heights of the spectral peaks gradually decrease with the increase of their frequencies. However, the heights of the spectral peaks are almost independent of the rf frequency. It is noteworthy that, the normal surface charging field E_x consist of only even harmonics of the rf frequency. This is expected since surface charging due to multipactor discharge from the single dielectric surface is independent of the direction (i.e. either positive or negative) of the parallel rf electric field E_{rf}, and the normal surface charging field E_x must be symmetric in the positive and negative half cycles of E_{rf}.

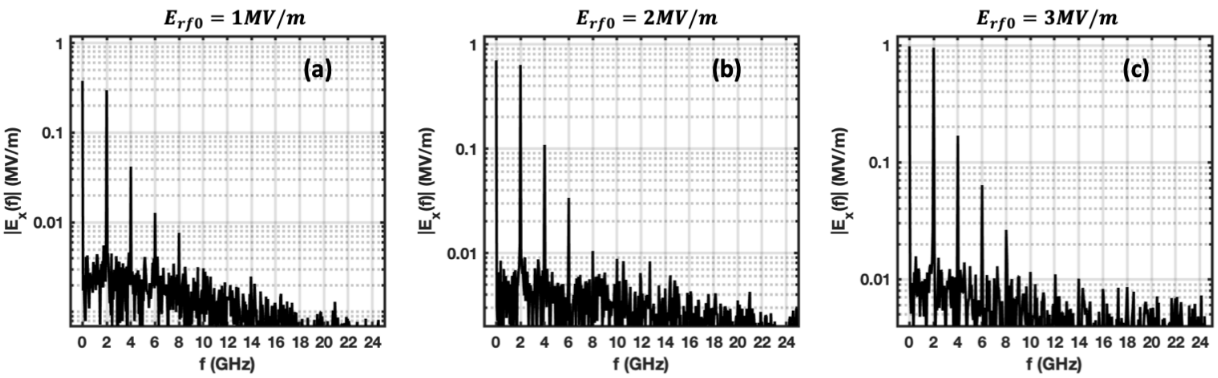

Figure 4.3. Amplitude spectrum of the normal electric field in the ac saturation state induced by a single frequency rf field with rf frequency $f_{rf} = 1$GHz and rf amplitudes, $E_{rf0} =$ (a)1MV/m, (b) $2M$V/m, (c) 3MV/m. Pronounced spectral peaks are observed at even harmonics of the rf frequency in each case. The heights of the spectral peaks increase linearly with the increase of the rf amplitude.

In Fig. 4.3, we plot the amplitude spectrum of E_x for rf amplitudes $E_{rf0} = 1\text{MV/m}, 2\text{MV/m}$, and 3MV/m while the rf frequency is kept fixed at $f_{rf} = 1$GHz. It is clear from these plots that the heights of the spectral peaks at even harmonics increase as the rf amplitude increases. We can express the relation between the heights of the spectral peaks, E_{xl}, at even harmonic frequencies of the rf frequency, $f = 2lf_{rf}$, and the rf amplitude, E_{rf0}, with the following linear equation,

$$E_{xl}(\text{MV/m}) = A_l E_{rf0}(\text{MV/m}) + B_l \tag{4.1}$$

By curve fitting, we obtain the following empirical formula for the coefficients A_l and B_l.

$$A_l = a(2l)^b \tag{4.2a}$$

$$B_l = c(2l) + d \tag{4.2b}$$

For the DFT results in Figs. 4.2 and 4.3, we find $a = 1.709, b = -2.379, c = 0.004$, and $d = -0.036$. The temporal profiles of the normal electric field can be expressed in terms of the DFT peaks as,

$$E_x \cong E_{x,avg} + \sum_{l=1}^{4} E_{xl} \sin(2l\omega_0 t). \tag{4.3}$$

Here, $E_{x,avg}$ is the time averaged value of the normal electric field in the ac saturation state, which is the peak observed at frequency $f = 0$ in the amplitude spectrum of E_x and $\omega_0 = 2\pi f_{rf}$ is the angular frequency of the rf field. It is noteworthy that, for a given E_{rf0}, the value of $E_{x,avg}$ can also be interpolated at point "A" from the lower susceptibility boundary of the susceptibility diagram of Fig. 4.1(c).

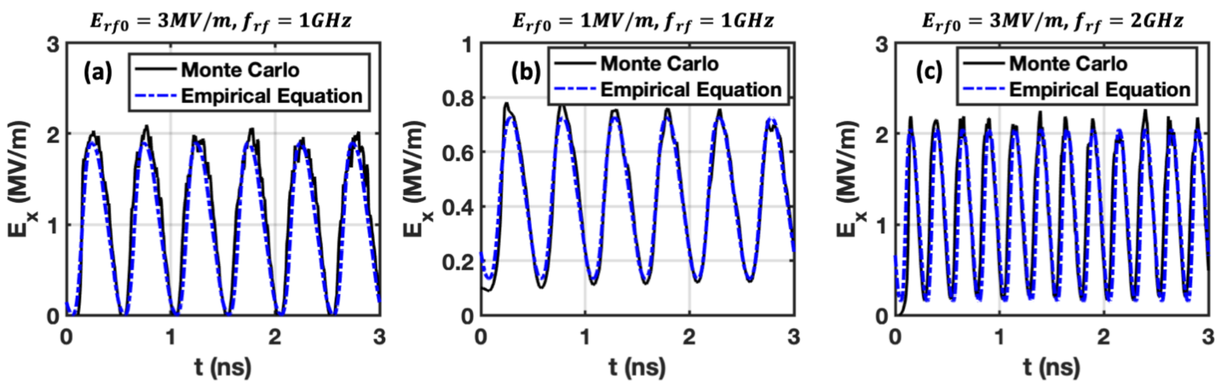

Figure 4.4. Temporal profiles of the normal electric field E_x in the ac saturation state obtained from the MC simulation (black solid lines) and the empirical relation in Eq. (4.3) (blue dashed lines) for single frequency rf fields with (a) rf amplitude $E_{rf0} = 3\text{MV/m}$ and rf frequency $f_{rf} = 1\text{GHz}$, (b) $E_{rf0} = 1\text{MV/m}$ and $f_{rf} = 1\text{GHz}$, and (c) $E_{rf0} = 3\text{MV/m}$ and $f_{rf} = 2\text{GHz}$. The time averaged saturation values used in these cases are $E_{x,avg} = 0.93\text{MV/m}, 0.42\text{MV/m}$, and 1.03MV/m respectively.

In Fig. 4.4, we have the temporal profiles of the normal electric fields obtained from Eq. (4.3) (blue dashed lines) and from the MC simulation (black solid lines), showing very good agreement. The differences are due to the fact that in Eq. (4.3) we only included the first four even harmonics which were the most pronounced in the amplitude spectrums. The higher harmonics of E_x could not be recovered with confidence due to the background noises of the FFT. Here, it is important to note that even though the coefficients used in Eq. (4.2) are obtained by fitting the data in Figs. 4.2 and 4.3, they remain applicable to new cases in Fig. 4.4.

4.2. Analysis for Two-Frequency RF Field Induced Multipactor

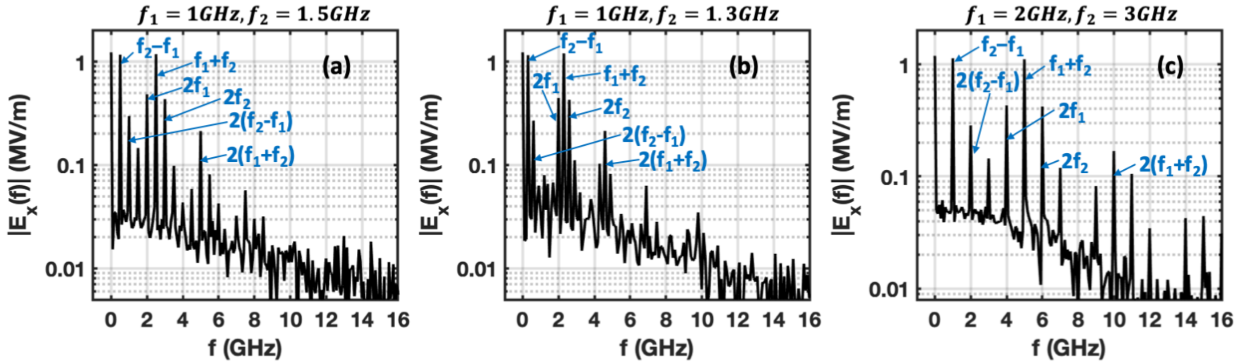

Figure 4.5. Amplitude spectrum of the normal electric field in the ac saturation state induced by a two-frequency rf field with individual carrier amplitude, $E_{rf0} = 3\text{MV/m}$ (with $\beta = 1$ in Eq. (2.1)) and carrier frequencies (a) $f_1 = 1\text{GHz}, f_2 = 1.5\text{GHz}$, (b) $f_1 = 1\text{GHz}, f_2 = 1.3\text{GHz}$, (c) $f_1 = 2\text{GHz}, f_2 = 3\text{GHz}$. Pronounced spectral peaks are observed at frequencies $(f_2 \pm f_1)$, $2f_{1,2}$, and $2(f_2 \pm f_1)$.

We extend our analysis to multipactor due to two-frequency rf fields. Figure 4.5 shows the amplitude spectrum of the normal electric field E_x for three cases of a two-frequency rf field. The individual rf amplitude is kept fixed at $E_{rf0} = 3\text{MV/m}$ (with $\beta = 1$ in Eq. (2.1)) for all three cases. The carrier frequencies are varied as $f_1 = 1\text{GHz}$ and $f_2 = 1.5\text{GHz}$ (Fig 4.5(a)), $f_1 = 1\text{GHz}$ and $f_2 = 1.3\text{GHz}$ (Fig 4.5(b)), and $f_1 = 2\text{GHz}$ and $f_2 = 3\text{GHz}$ (Fig 4.5(c)), corresponding to $n = f_2/f_1$ = 1.5, 1.3, and 1.5 in Eq. (2.1), respectively. We observe spectral peaks at various frequencies of intermodulation products in the amplitude spectrum of E_x. Pronounced peaks are observed at the sum and difference frequencies of the carrier frequencies, at multiples of those frequencies, and at multiples of the individual carrier frequencies. We list the frequencies of the most pronounced peaks observed in Figs. 4.5(a)-(c) in Table 4.1.

RF frequencies		Frequencies of the strongest peaks		Frequencies of the 2nd strongest peaks		Frequencies of the next two strongest peaks	
f_1	f_2	$f_2 - f_1$	$f_1 + f_2$	$2f_1$	$2f_2$	$2(f_2 - f_1)$	$2(f_1 + f_2)$
1	1.5	0.5	2.5	2	3	1	5
1	1.3	0.3	2.3	2	2.6	0.6	4.6
2	3	1	5	4	6	2	10

Table 4.1. Frequencies of prominent spectral peaks in Fig. 4.5. All the frequencies are in GHz.

We observe from Fig. 4.5 that the heights of the different intermodulation peaks, $f_2 \pm f_1$, $2f_{1,2}$, and $2(f_2 \pm f_1)$, remain unchanged with the change of the carrier frequencies. For all three cases, the two strongest peaks have equal spectral heights and appear at the sum and difference frequencies of the carrier frequencies, $f_2 \pm f_1$. The two second strongest peaks with equal heights appear at twice the carrier frequencies, $2f_{1,2}$. The third and fourth strongest peaks appear at twice the difference, $2(f_2 - f_1)$, and twice the sum, $2(f_2 + f_1)$, of the carrier frequencies, respectively. A number of weaker peaks are also observed at various intermodulation products of the carrier frequencies. For instance, we find weaker peaks at frequencies $3f_1 - f_2 = 1.5\text{GHz}$, $3f_2 - f_1 = 3.5\text{GHz}$, $3f_1 + f_2 = 3f_2 = 4.5\text{GHz}$, $f_1 + 3f_2 = 5.5\text{GHz}$, $3f_1 + 2f_2 = 6\text{GHz}$ and $3(f_1 + f_2) = 7.5\text{GHz}$ in Fig. 4.5(a), at frequencies $3f_2 - f_1 = 2.9\text{GHz}$, $3f_1 + f_2 = 4.3\text{GHz}$, $f_1 + 3f_2 = 4.9\text{GHz}$, and $3(f_1 + f_2) = 6.9\text{GHz}$ in Fig. 4.5(b), at frequencies $3f_1 - f_2 = 3\text{GHz}$, $3f_2 - f_1 = 7\text{GHz}$, $3f_2 = 9\text{GHz}$, $f_1 + 3f_2 = 11\text{GHz}$, $3f_1 + 2f_2 = 12\text{GHz}$, $f_1 + 4f_2 = 14\text{GHz}$, and $3(f_1 + f_2) = 15\text{GHz}$ in Fig. 4.5(c).

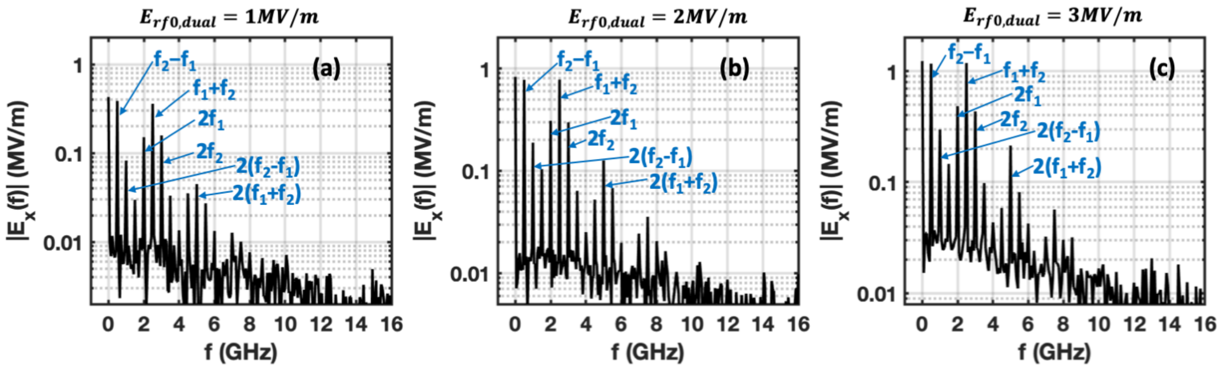

Figure 4.6. Amplitude spectrum of the normal electric field in the ac saturation state induced by a two-frequency rf field with carrier frequencies $f_1 = 1$GHz, $f_2 = 1.5$GHz (i.e. $n = 1.5$ in Eq. (2.1)) and equal rf amplitudes ($\beta = 1$ in Eq. (2.1)) for the two carriers, $E_{rf0,dual} =$ (a)1MV/m, (b) 2MV/m, (c) 3MV/m. Pronounced spectral peaks are observed at frequencies $(f_2 \pm f_1)$, $2f_{1,2}$, and $2(f_2 \pm f_1)$. The heights of the spectral peaks increase with the rf amplitude.

In Fig. 4.6, we plot the amplitude spectrum of the normal electric field by a dual-frequency rf field with carrier frequencies $f_1 = 1$GHz and $f_2 = 1.5$GHz and equal amplitudes for the two carriers (i.e. $n = 1.5$, and $\beta = 1$ in Eq. (2.1)), for $E_{rf0} = 1$MV/m, 2MV/m, and 3MV/m. It is clear that the heights of the spectral peaks increase as the rf amplitude increases. The relation between the spectral peak heights at different frequencies of intermodulation products and the rf amplitude can still be fitted with the linear Eq. (4.1), with the coefficients A_l and B_l listed in Table 4.2.

l	Frequency (f_l^{IM})	Coefficient A_l	Coefficient B_l
1	$f_2 - f_1$	0.4005	−0.02547
2	$f_1 + f_2$		
3	$2f_1$	0.1518	−0.001782
4	$2f_2$		
5	$2(f_2 - f_1)$	0.1073	−0.02528
6	$2(f_1 + f_2)$	0.08427	−0.04026

Table 4.2. Empirical values of coefficients A_l and B_l at frequencies of intermodulation products with the strongest peaks.

For dual-frequency operation, the temporal profiles of the normal electric field is approximated as,

$$E_x \cong E_{x,avg} + \sum_{l=1}^{6} E_{xl} \sin\left(2\pi f_l^{IM} t\right). \tag{4.4}$$

Here, $E_{x,avg}$ is the time averaged value of the normal electric field in the ac saturation state, which is the peak observed at frequency $f = 0$ in the amplitude spectrum of E_x, and f_l^{IM} denotes the frequencies of intermodulation products, as shown in Figs. 4.5 and 4.6. Figure 4.7 plots the temporal profiles of E_x obtained from Eqs. (4.1) and (4.4) with coefficients in Table 4.2 (blue dashed lines) and from the MC simulation (black solid lines), showing very good agreement. The differences are due to the fact that only the first six strongest frequency peaks are included in Eq. (4.4). More frequency components can be added to Eq. (4.4) to give better predictions.

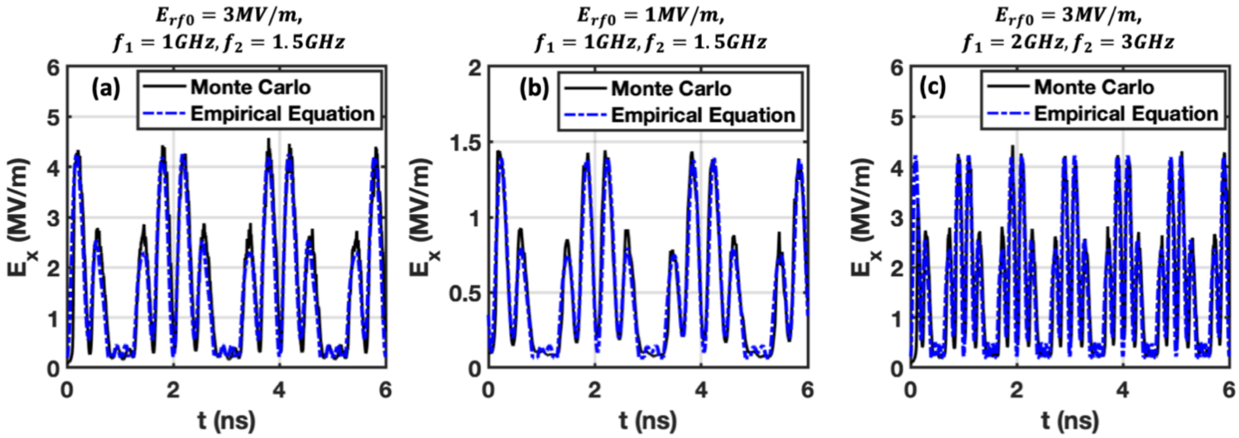

Figure 4.7. Temporal profiles of the normal electric field E_x in the ac saturation state obtained from the MC simulation (black solid lines) and empirical Eq. (4.4) (blue dashed lines) for dual-frequency rf fields with (a) $E_{rf0,dual} = 3\text{MV/m}$, $f_1 = 1\text{GHz}$, $f_2 = 1.5\text{GHz}$, (b) $E_{rf0,dual} = 1\text{MV/m}$, $f_1 = 1\text{GHz}$, $f_2 = 1.5\text{GHz}$, and (c) $E_{rf0,dual} = 3\text{MV/m}$, $f_1 = 2\text{GHz}$, $f_2 = 3\text{GHz}$. The time-averaged saturation values used in these cases are $E_{x,avg} = 1.3\text{MV/m}$, 0.52MV/m, and 1.3MV/m, respectively.

CHAPTER 5: Two Surface Multipactor with Two-Frequency RF Fields

In this Chapter, we present a study on two surface multipactor discharge with two-frequency rf fields. We discuss the electron dynamics of parallel plate resonant multipactor for single- and two-frequency rf operation. We present the analytical model as well as the Monte Carlo and CST simulation methods used to construct multipactor susceptibility charts. We analyze the effects of the relative strength and phase of the second carrier mode on multipactor susceptibility. The effect of space charge on multipactor susceptibility and the time dependent physics is also studied. This Chapter is based on a manuscript under preparation titled, "Two surface multipactor discharge with two-frequency rf fields", by A. Iqbal, *et al*.

5.1. Analysis for Single Frequency RF Field Induced Multipactor

5.1.1. Electron Dynamics

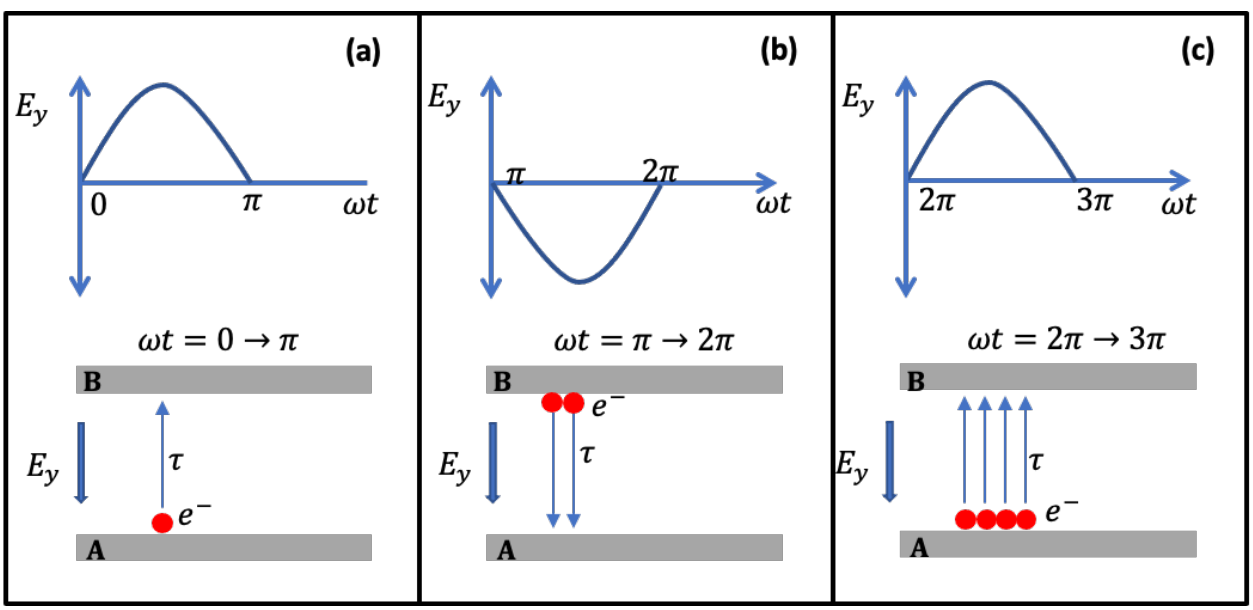

Figure 5.1. Multipactor discharge with an electric field oscillating between two metal electrodes A and B. Upon each electron impact, secondary electrons are emitted from the surface, multiplying the total number of electrons at each half cycle.

Figure 5.1 depicts the simplified schematic of two surface multipactor discharge for single frequency rf operation. An rf electric field $E_y = E_{rf}\sin(\omega t + \theta)$ is applied normal to the parallel plates A and B along the *y*-direction. Here E_{rf} is the peak electric field strength, ω is the angular frequency, and θ is the initial phase of the electric field. In panel (a) of Fig. 5.1, an electron is born in plate A and then accelerated by the RF electric field. Assuming 1-D motion in the *y*-direction, the flight trajectory of a multipactor electron is governed by the force law,

$$a(t) = \frac{eE_{rf}}{m} sin(\omega t + \theta) = \frac{eV_{rf}}{md} sin(\omega t + \theta), \tag{5.1}$$

where $a(t)$ is the acceleration, V_{rf} is the peak voltage, and d is the gap distance between plates A and B. The velocity of the electron is obtained as,

$$v = \frac{eV_{rf}}{m\omega d}[cos\theta - \cos(\omega t + \theta)] + v_0, \tag{5.2}$$

From Eq. (5.2), we obtain the instantaneous position of a multipactor electron as,

$$y = \frac{eV_{rf}}{m\omega^2 d}\{\omega t cos\theta - \sin(\omega t + \theta) + sin\theta\} + v_0 t + y_0. \tag{5.3}$$

Here y_0 accounts for initial position of the particles at $t = 0$. The transit time τ_{AB} of an electron in flight from plate A to plate B, is calculated by solving Eq. (5.3) for $y = d$.

Let us assume that the electron hits the opposite electrode (plate B) with sufficient energy for emission of more than one electron. This emission occurs near the time when the field reverses direction at $\omega t = \pi$, and each of the emitted secondary electrons, as shown in panel (b), is then accelerated across the gap in the reverse direction. Again, these electrons traverse the gap in half the cycle time and impact plate A with enough energy to cause further electron multiplication by secondary emission. This process continues with each half cycle as the multipactor develops.

Several conditions need to be satisfied for the successful development of the two surface multipactor discharge as depicted in Fig. 5.1. Firstly, the rf frequency and system geometry coupled with the accelerating electric field must give rise to this type of resonant electron motion. If the rf electric field is too high for a given frequency and electrode spacing, the initial electron will impact too early, the secondary electrons will be emitted against the electric field, and they will not be able to accelerate back across the electrode gap. On the other hand, if the electric field is too low, the electron may not be able to reach the opposite electrode during half cycle of the rf field, or it may impact with insufficient energy for secondary electron. As a result, electrons which sustain the multipactor are focused into a narrow sheet over many cycles, impacting with the required phase range to sustain the resonance. Secondly, the impacted surfaces must allow for a gain in the number of electrons by secondary emission, i.e., the secondary electron yield must be greater than unity for the impacting multipactor electrons. Lastly, it is necessary for this discharge to occur under vacuum pressures, typically less than 1 mtorr [17], as frequent collisions with background gas can prevent the necessary resonant electron motion.

5.1.2. Analytical Solution

The multipactor resonant condition specifies that the electron must traverse the electrode spacing, d, and impact the opposing surface near the time the electric field changes direction. The electric field changes direction at $\omega t = N\pi + \theta$, where N is a positive odd integer, i.e., $y = d$ at $\omega t = N\pi + \theta$. Invoking this condition in Eq. (5.3), the multipactor condition for the voltage in a parallel plate geometry is given by,

$$V_{rf} = \frac{m}{e}\frac{\omega d(\omega d - v_0 N\pi)}{N\pi cos\theta + 2sin\theta} \tag{5.4}$$

The minimum voltage necessary to sustain a multipactor will occur at the phase that maximizes $N\pi cos\theta + 2sin\theta$ regardless of the value of v_0. This maximum occurs when

$$\theta = \arctan\left(\frac{2}{N\pi}\right) \tag{5.5}$$

Equations (5.4) and (5.5) give the conditions for the lower multipactor boundary [2]. The upper boundaries are given by equation (5.4) too, but with the maximum negative value of the angle θ, determined by the condition that the initial emission velocity v_0 just allows the electron to escape against the initially retarding field (Fig. 5.2) [2].

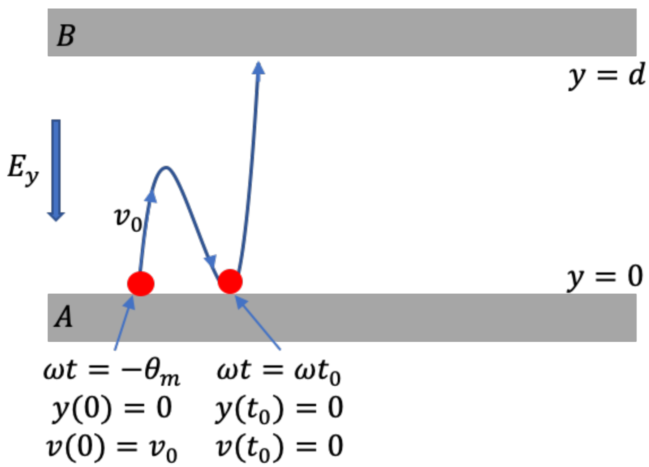

Figure 5.2. Trajectory of an electron for the upper multipactor boundary. Electron emitted from surface A at rf phase $\theta = -\theta_m$ reaches position $y = 0$ with velocity $v = 0$ as the electric field changes direction at time $t = t_0$. The electron does not impact surface A. It is accelerated by the reversed electric field, traverses the electrode spacing d and impacts surface B.

If an electron is launched from plate A at phase $\theta = -\theta_m$ ($0 \leq \theta_m \leq \pi$) and reaches position $y = 0$ with velocity $v = 0$ as the electric field changes direction at time $t = t_0$, then from Eqs. (5.2) and (5.3) we have,

$$v(t_0) = \frac{e}{m}\frac{V_{rf}}{\omega d}(\cos(-\theta_m) - \cos(\omega t_0 - \theta_m)) + v_0 = 0, \tag{5.6}$$

$$y(t_0) = \frac{e}{m}\frac{V_{rf}}{\omega^2 d}[cos(-\theta_m)(\omega t_0) - sin(\omega t_0 - \theta_m) + sin\,(-\theta_m)] + v_0 t_0 = 0. \tag{5.7}$$

These equations can be normalized as follows,

$$\cos(\overline{\omega}\overline{\tau} - \theta_m) - cos\theta_m = \frac{\overline{\omega}}{\overline{\overline{V_{rf}}}}, \tag{5.8}$$

$$\frac{\overline{V_{rf}}}{\overline{\omega}^2}[(\overline{\omega}\overline{t_0})cos\theta_m - sin(\overline{\omega}\overline{t_0} - \theta_m) - sin\theta_m] + \overline{t_0} = 0, \tag{5.9}$$

where $\overline{\omega} = \frac{\omega}{v_0}d$, $\overline{V_{rf}} = \frac{\overline{\omega}^2\left(1-\frac{N\pi}{\overline{\omega}}\right)}{-2sin\theta_m+N\pi cos\theta_m}$, and $\overline{t_0} = \frac{t_0 v_0}{d}$. From Eq. (5.8) we get,

$$\overline{\omega}\overline{t_0} = \theta_m \pm acos\left(\frac{\overline{\omega}}{\overline{V_{rf}}} + cos\theta_m\right). \tag{5.10}$$

Substituting Eq. (5.10) in Eq. (5.9), we get,

$$\left[\theta_m \pm \text{acos}\left(\frac{\overline{\omega}}{\overline{V_{rf}}} + \cos\theta_m\right)\right] cos\theta_m - \sin\left[\pm \text{acos}\left(\frac{\overline{\omega}}{\overline{V_{rf}}} + \cos\theta_m\right)\right] + \frac{\overline{\omega}}{\overline{V_{rf}}}\left[\theta_m \pm \text{acos}\left(\frac{\overline{\omega}}{\overline{V_{rf}}} + \cos\theta_m\right)\right] - sin\theta_m = 0. \tag{5.11}$$

We can solve Eq. (5.11) to find the angle θ_m, and the upper multipactor boundary can then be found by substituting $\theta = -\theta_m$ in Eq. (5.4). Figure 5.3 shows the multipactor upper and lower boundaries for the first three modes, $N = 1{,}3{,}$ and 5 for emission energy, $V_0 = \frac{1}{2}mv_0^2 = 2\text{eV}$, where v_0 is the emission velocity.

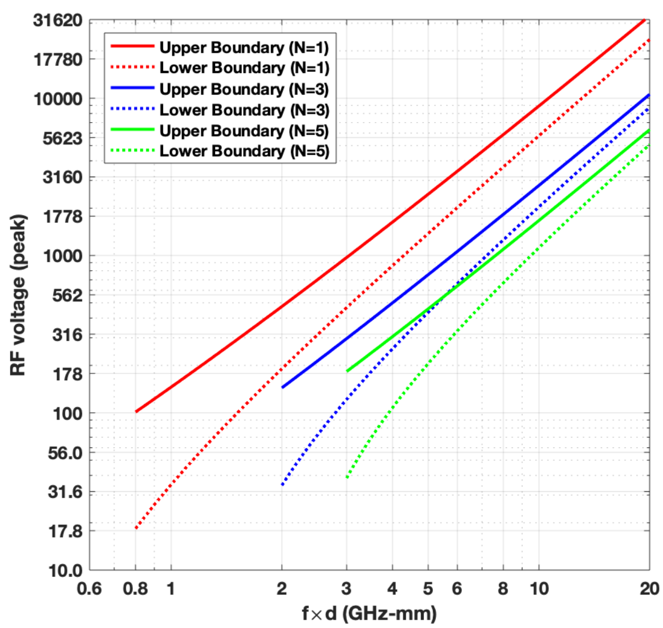

Figure 5.3. Multipactor upper and lower boundaries for the first three modes, $N = 1{,}3{,}$ and 5 for emission energy, $V_0 = \frac{1}{2}mv_0^2 = 2\text{eV}$, where v_0 is the emission velocity. The lower boundary for each mode is determined by Eqs (5.4) and (5.5); and the upper boundary for each mode is determined by Eqs (5.4) and (5.11).

As previously discussed in section 5.1, the secondary electron yield must be greater than unity for the impacting multipactor electrons for the development of the two surface multipactor discharge. In this study, we assume copper (Cu) as the electrode material and employ Vaughan's model for secondary electron emission as described in Chapter 2 Section 2.2. As shown in Fig. 5.4a, we use a first crossover incident energy $V_1 = 42$ eV, a second crossover incident energy $V_2 = 3054$ eV, a peak incident energy $V_{max0} = 277.5$ eV, and a peak SEY $\delta_{max0} = 2.0887$; all of these values are for normal incidence. The impact velocities corresponding to the first and second crossover incident energies lead to two more boundaries [128],

$$V_{rf}\left(V_0; V_{1,2}, fd, N\right) = \frac{m\omega d}{2e} \times \sqrt{\frac{(N\pi)^2+4}{2m}\left(\sqrt{V_{1,2}} - \sqrt{V_0}\right)^2 + \left(\omega d - N\pi\sqrt{\frac{2V_0}{m}}\right)^2 - N\pi\left(\sqrt{\frac{2V_{1,2}}{m}} - \sqrt{\frac{2V_0}{m}}\right)\left(\omega d - N\pi\sqrt{\frac{2V_0}{m}}\right)}, \tag{5.12}$$

which are shown in Fig. 5.4b.

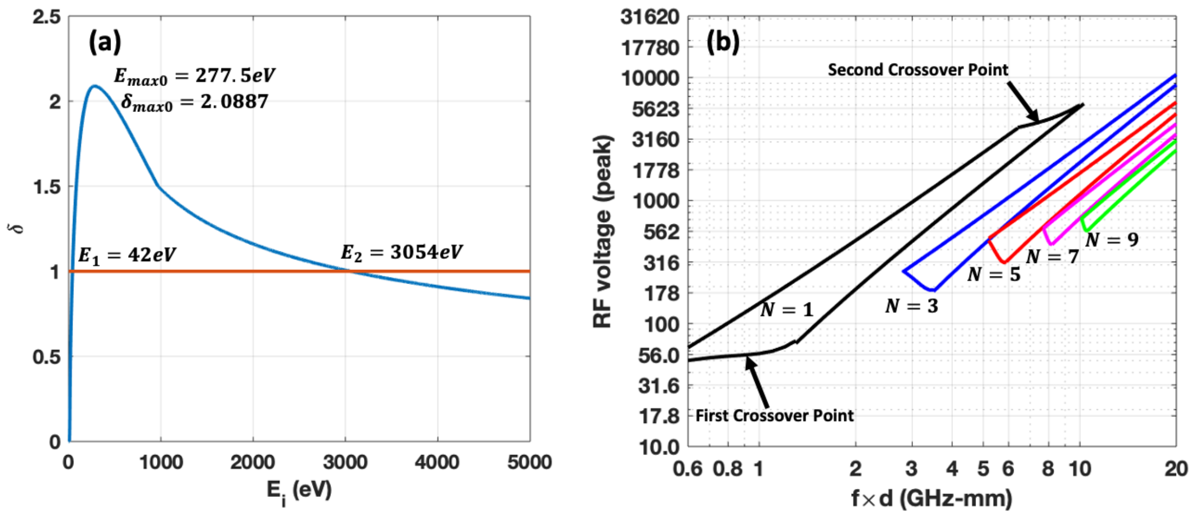

Figure 5.4. (a) SEY vs. incidence energy curves for copper electrode from Vaughan's models for impact angle $\xi = 0$. Here, the first crossover incident energy $V_1 = 42$ eV, the second crossover incident energy $V_2 = 3054$ eV, the peak incident energy $V_{max0} = 277.5$ eV, and the peak SEY $\delta_{max0} = 2.0887$. (b) The corresponding multipactor susceptibility chart for the first five modes, $N = 1, 3, 5, 7$ and 9 with emission energy, $V_0 = \frac{1}{2}mv_0^2 = 2$eV. The boundaries corresponding to the first and second crossover points are calculated from Eq. (5.12)

5.1.3. Monte Carlo (MC) Simulation

To calculate the growth rate of the multipactor discharge, we follow the trajectory of a weighted macroparticle over a large number of impacts in a MC simulation [4,5,57]. The initial rf phase, θ, is uniformly distributed over $0 \leq \theta < 2\pi$. Each time a macroparticle leaves the surface of an electrode, we assign it a random initial energy $E_0 = (½)mv_e^2$ and angle ϕ according to the distributions given in Eq. (2.6). As described in Section 5.1, the transit time $t = \tau_{AB}$ of an electron in flight from plate A to plate B, is calculated by solving Eq. (5.3) for $v_0 = v_e sin\phi, y_0 = 0$, $y(t = \tau_{AB}) = d$. The transit time $t = \tau_{AA}$ for single surface impact on plate A is calculated by solving Eq. (5.3) for $v_0 = v_e sin\phi, y_0 = 0$, and $y(t = \tau_{AA}) = 0$. The transit time $t = \tau_{BA}$ of an electron in flight from plate B to plate A, is calculated by solving Eq. (5.3) for $v_0 = -v_e sin\phi, y_0 = d, y(t = \tau_{BA}) = 0$, and the transit time $t = \tau_{BB}$ for single surface impact on plate B is calculated by solving Eq. (5.3) for $v_0 = -v_e sin\phi, y_0 = d$, and $y(t = \tau_{BB}) = d$. We substitute the random values of initial velocity and angle into Eqs. (5.2) to calculate the impact energy, E_i, and hence, the secondary electron yield, δ, from Eq. (2.4). We use this value of the yield to adjust the charge and mass on the macroparticle and then emit it again with a random velocity. We repeat the process to obtain a series of yields ($\delta_1 . \delta_2 \dots \delta_N$) for a large number of impacts. The rf phase θ is calculated self-consistently ($\theta_{i+1} = \theta_i + \omega\tau_i$) at the beginning of each flight for a given macroparticle. The average value of secondary yield over N impacts is then calculated as $\bar{\delta} = (\delta_1 . \delta_2 \dots \delta_N)^{1/N}$, where a $N = 20$ is used in the calculation, corresponding to 10 rf periods. For a specific combination of rf frequency ω , gap distance d, and accelerating voltage V_{rf}, if we find a valid electron trajectory for which $\bar{\delta} > 1$, we conclude that multipactor discharge develops in the system for these parameters.

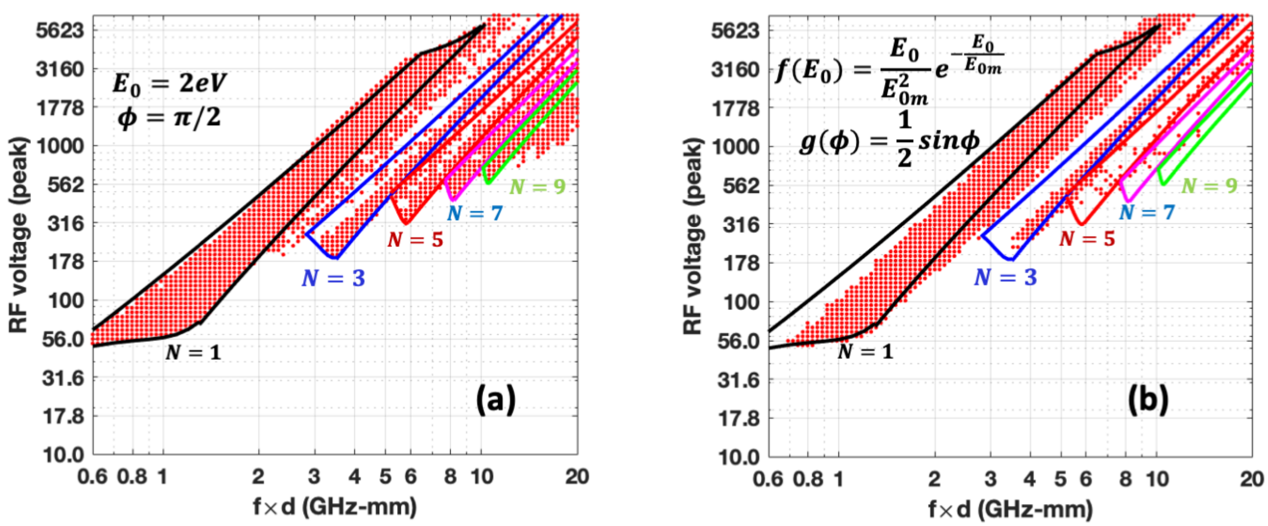

Figure 5.5. (a) Multipactor susceptibility chart calculated from MC simulation (red dotted regions) for fixed emission energy, $V_0 = \frac{1}{2}mv_0^2 = 2\text{eV}$ and emission angle $\phi = \pi/2$ along with analytical boundaries for the first five modes, $N = 1$ (solid black line), 3 (solid blue line), 5 (solid red line), 7 (solid magenta line) and 9 (solid green line) calculated as described in Section 5.1.2. (b) Same plot as in (a) but for random emission energy and emission angle given by Eq. (2.6). These simulations were produced using SEY Vaughan's model parameters for copper $E_{max0} = 277.5\text{eV}$, $\delta_{max0} = 2.088, T_e = 2\text{eV}$. For all cases, we use rf frequency, $f = 1\text{GHz}$, and variation of fd is obtained by varying the gap distance, d.

Figure 5.5 shows the comparison of the susceptibility chart obtained from the analytical calculations described in section 5.1.2 and the MC simulation described in this section. In Fig. 5.5(a), the MC simulation is conducted for secondary electrons with fixed emission energy, $V_0 = \frac{1}{2}mv_0^2 = 2\text{eV}$ and emission angle $\phi = \pi/2$ which is similar to the analytical prediction. Therefore, in this case, the susceptibility chart obtained from the MC simulation and the analytical calculation are in good agreement with each other. In Fig. 5.5(b), the MC simulation is conducted with random emission energy and emission angle for secondary electrons given by Eq. (2.6), which leads to a shift in the boundaries of multipactor susceptibility between the MC simulation and the analytical calculation in this case. It is also found that allowing random emission energy and angle for secondary electron emission results in a relatively smaller region of multipactor susceptibility.

5.1.4. Electron Trajectory and Multipactor Modes

To explain the differences between the analytical and the MC simulation results in Fig 5.5, in Fig 5.6, we show the trajectories of the macroparticle for different points in the susceptibility chart obtained from the MC simulation invoking Eq. (5.3).

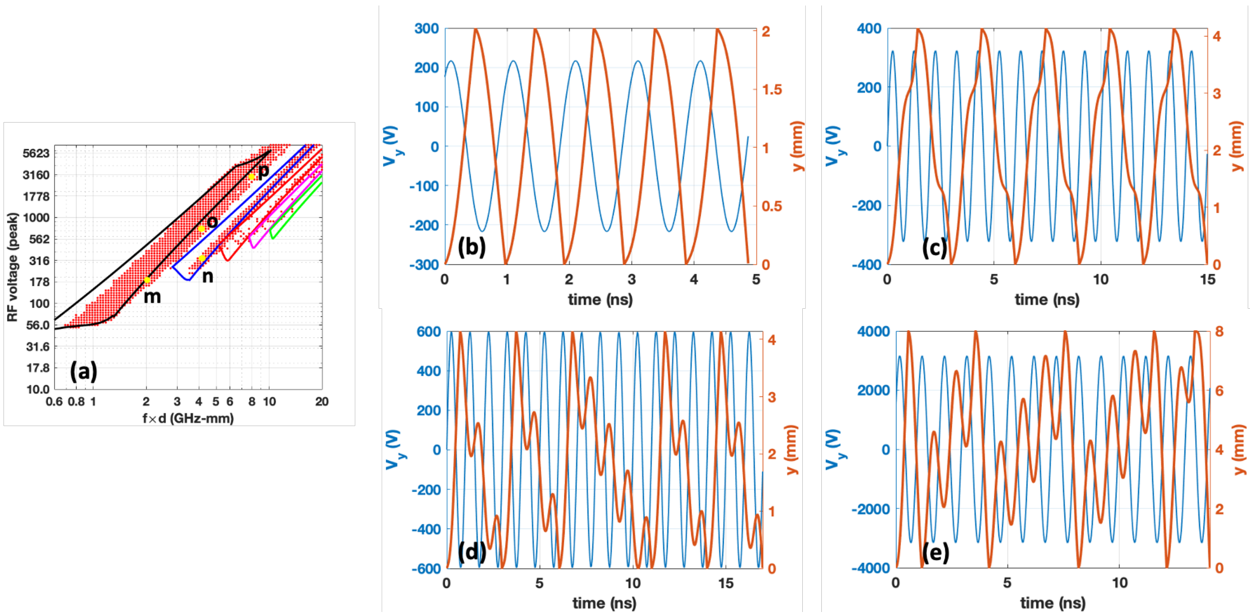

Figure 5.6. (a) Multipactor susceptibility chart calculated from MC simulation (red dotted regions) for random emission energy and emission angle along with analytical boundaries for the first five modes, $N = 1$ (solid black line), 3 (solid blue line), 5 (solid red line), 7 (solid magenta line) and 9 (solid green line) calculated as described in in section 5.1.2. (b)-(e): Instantaneous rf voltage (blue lines) and the corresponding macroparticle trajectories (red lines) for (b) $V_{rf} = 216.5\text{V}$, $fd = 2.025$ GHz · mm, (c) $V_{rf} = 323.3\text{V}$, $fd = 4.143$ GHz · mm, (d) $V_{rf} = 600\text{V}$, $fd = 4.143$ GHz · mm, and (e) $V_{rf} = 3160\text{V}$, $fd = 8$ GHz · mm. For all the cases, we use rf frequency, $f = 1\text{GHz}$, and variation of fd is obtained by varying the gap distance, d. Plots (b)-(e) correspond to the points m, n, o, and p in the susceptibility chart of plot in (a), respectively.

In Figs 5.6(b)-(e), we consider a few cases of successful multipactor development from the MC simulation with different combinations of V_{rf} and fd. For the cases in Figs. 5.6(b)-(c) corresponding to the points m and n in the susceptibility chart of Fig. 5.6(a), we observe that the transit time of the macroparticle from the top plate to the bottom plate is equal to the transit time of the macroparticle from the bottom plate to the top plate. For the case in Fig 5.6(b), multipactor develops for an emission angle $\theta = 0.9468 = 0.3014\pi$ and the macroparticle crosses the gap distance in $N = 1$ half cycle of the rf period. Therefore, the corresponding point m in Fig 5.6(a) lies inside the analytical susceptibility region of $N = 1$ mode. For the case in Fig 5.6(c), multipactor develops for an emission angle $\theta = 0$ and the macroparticle crosses the gap distance in $N = 3$ half cycles of the rf period. Therefore, the corresponding point n in Fig 5.6(a) lies inside the analytical susceptibility region of $N = 3$ mode.

However, for the cases of Figs 5.6(d)-(e) where multipactor develops for emission angles of $\theta = 0,$ and 0.4974 $(= 0.1583\pi)$ respectively, the transit times of the macroparticle from the top plate to the bottom plate are not equal to the transit times of the macroparticle from the bottom plate to the top plate. Therefore, these cases give rise to mixed multipactor modes and the corresponding points o and p in Fig 5.6(a) lie outside the analytical susceptibility region. From this examination, it is clear that the difference between the analytical and the MC simulation results is largely due to the mixed multipactor modes, which are not considered in the analytical calculations. Due to the simplified assumption that electrons take odd integer multiples of the rf half cycles to transit the gap distance, the analytical model is unable to resolve the mixed multipactor modes.

5.1.5. CST Simulation

CST Particle Studio (CST PS) [129] is a particle-in-cell (PIC) code that includes secondary electron emission and has been widely used for the simulation of rf vacuum electronics [130–132] as well as multipactor discharge [88]. For the simulation of two-surface multipactor using CST, we consider a simple parallel plate structure as shown in Fig 5.7(a). Plates **A** and **B** are made of copper with a vacuum gap between them. Each plate has a length $l = 20mm$, width $w = 20mm$, and thickness $t_p = 0.2mm$. A constant amplitude of 1-GHz excitation is applied to the waveguide port on one end (port 1 in Fig. 5.7(b)) of the parallel plate structure and exits through a waveguide port on the opposite end (port 2 in Fig. 5.7(b)). For single frequency rf operation, the excitation signal is defined as $E_y = \frac{V_{rf}}{d} \sin \omega t$. A variation in fd is achieved in the simulation by varying the gap distance, d.

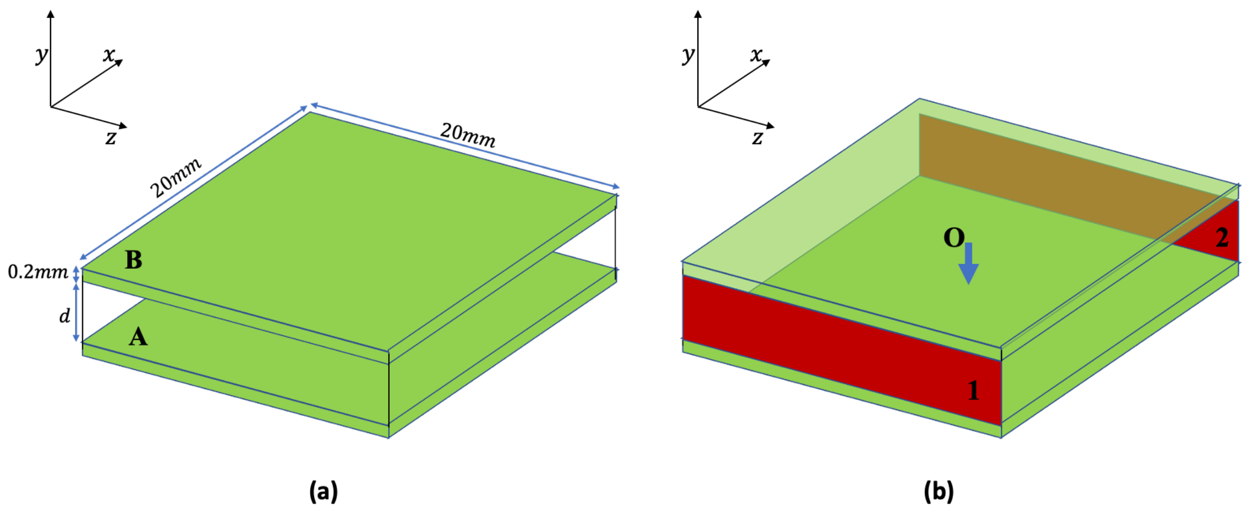

Figure 5.7. (a) Schematic of the parallel plate geometry used in the CST simulation for two surface multipactor. A and B are the bottom and top plates, respectively. The plates are separated by a gap distance d. (b) Waveguide ports 1 and 2 used to apply the 1-GHz excitation shown as red planes. O is the particle source with an emission area of $10^{-4}mm^2$.

A particle source O with an emission area of $10^{-4}\mathrm{mm}^2$ is located at the center of the top plate pointed toward the $-y$ direction. We run the simulation for $t = 10ns$ which corresponds to 10 cycles of the excitation signal. The time step is $0.01ns$. The particle source emits seed electrons into the vacuum gap between the plates during the first period of the excitation at a constant rate of 1515 particles/ns and remains inactive during the rest of the simulation. In the simulation, each macroparticle contains 1 electron, which is kept fixed for all the macroparticles throughout the simulation. Each injected electron has an initial kinetic energy, $E_{k0} = 0eV$. In this simulation, we turn off space charge effect in CST.

For secondary electron emission, we use the built-in Vaughan model in CST, which assumes an emission energy distribution that is gamma distributed and weighted by a temperature T_e [133]. For the simulations in this study, we assume a temperature of $T_e = 2$eV, which provides an emission energy probability distribution function (PDF) similar to the distribution given in Eq.

2.6(a) provided by Kishek and Lau [4]. Secondary electrons are emitted at angles relative to the surface normal with the following probability distribution function [133],

$$f(\theta) = cos\theta, \theta \in [0, \pi/2]. \tag{5.13}$$

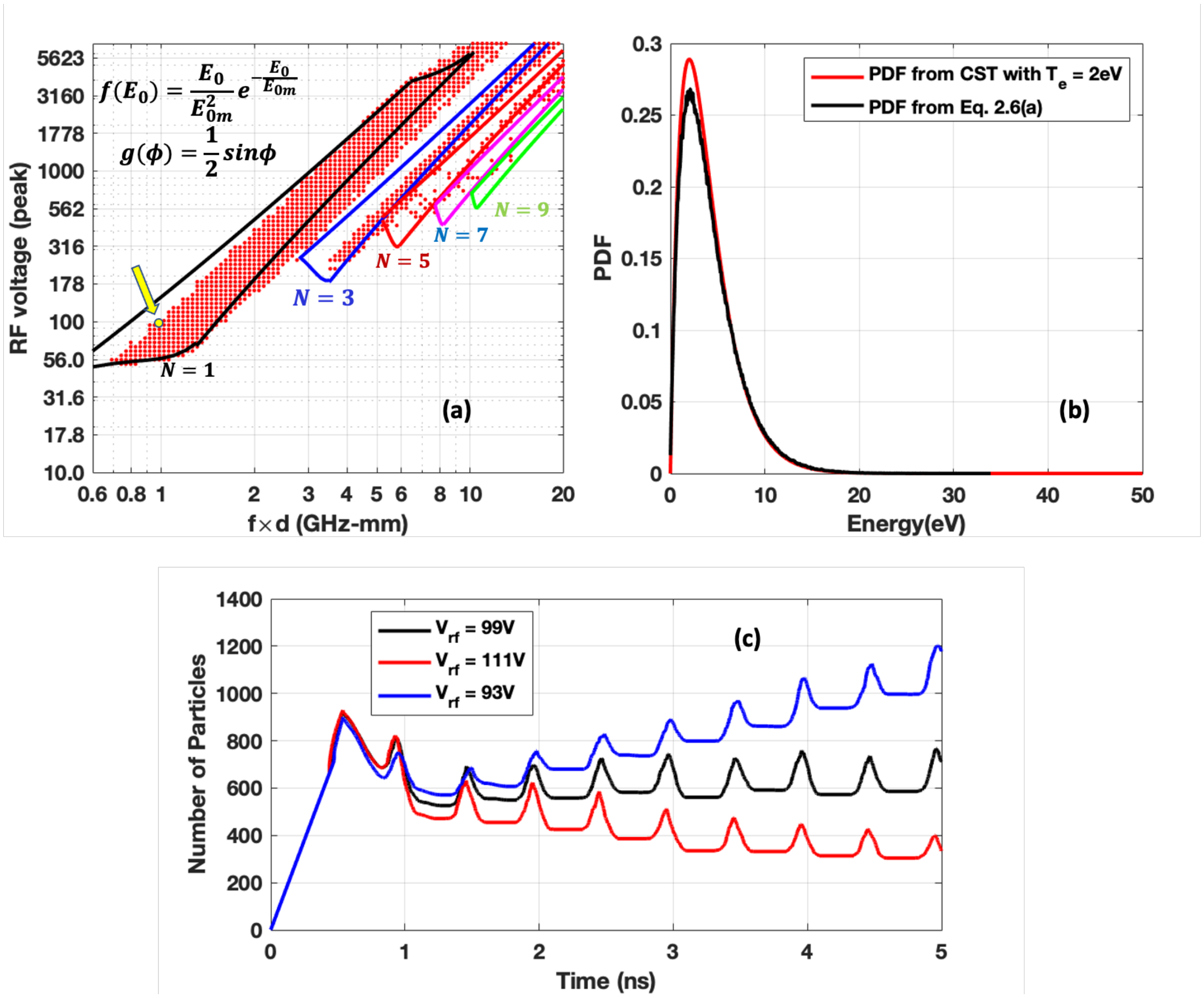

Figure 5.8. (a) Multipactor susceptibility chart calculated from MC simulation (red dotted regions) for random emission voltage and emission angle given by Eq. (2.6) along with analytical boundaries for the first five modes, $N = 1$ (solid black line), 3 (solid blue line), 5 (solid red line), 7 (solid magenta line) and 9 (solid green line) calculated as described in in section 5.1.2. (b) Emission energy probability distribution functions (PDF) obtained from CST with $T_e = 2eV$ (red curve) and from Eq. 2.6(a) (black curve). (c) Evolution of the electron population at gap voltage amplitudes, $V_{rf} = 99$V (black curve), 111V (red curve), and 93V (blue curve). These simulations were produced with $fd = 0.9902$ GHz·mm ($f = 1$ GHz, $d = 0.9902$ mm) using the peak incident energy $V_{max0} = 277.5$eV, peak SEY $\delta_{max0} = 2.088$, and $T_e = 2$eV as Vaughan's model parameters in CST.

It is known that multipactor discharge causes the electron population to increase exponentially. An example of this is shown in Fig. 5.8(c) at different applied voltage levels, with $fd = 0.9902$ GHz·mm. For all the applied voltages, an initial growth of electron population is observed at a constant rate as the particle source emits seed electrons during the first excitation period. After this initial increase, we observe an increase of electron population at a higher rate and then a decrease as seeded electrons with favorable phase and velocity are multiplied and electrons with unfavorable phase and velocity are absorbed by the boundaries. In the $V_{rf} = 99$V case (black curve in Fig. 5.8(c)), the electron population is periodically increasing and decreasing maintaining a time-averaged steady saturation level. Therefore, this voltage is expected to be very close to the multipactor threshold. In the $V_{rf} = 93$V case (blue curve in Fig. 5.8(c)), the electron population slowly increases, suggesting the voltage is within the multipactor susceptibility regime and still close to multipactor threshold. In the $V_{rf} = 111$V case (red curve in Fig. 5.8(c)), the electron population slowly decreases, suggesting multipactor will not be sustained in the long term.

As we can observe from Fig 5.8(a), the three points are indeed very close to the upper multipactor threshold boundary obtained from the MC simulation, justifying the slow growth and decay of electron population in Figs. 5.8(c). The case shown by the black curve in Fig 5.8(c) is the closest to the susceptibility boundary shown by yellow circle in Fig 5.8(a).

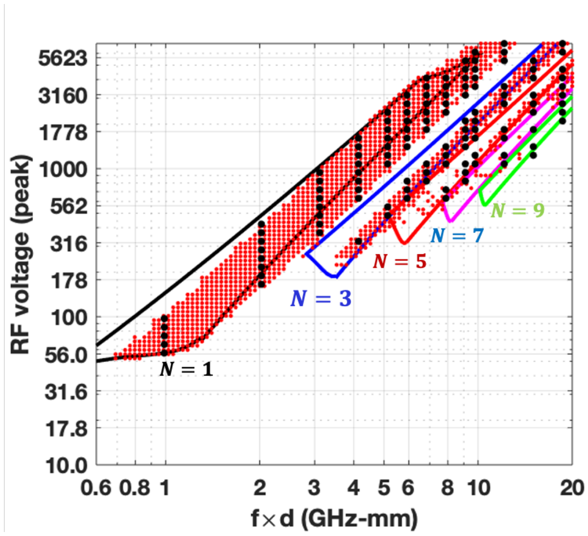

Figure 5.9. Comparison of the multipactor susceptibility chart obtained from analytical calculations (solid lines), MC simulation (red dotted regions), and CST simulation (black dotted regions). The CST simulation is conducted for $fd = 1, 2, 3, 4, 5, 6, 7, 8, 9, 10, 12, 15,$ and 18 GHz·mm. For all the cases, we use rf frequency, $f = 1$GHz, and variation of fd is obtained by varying the gap distance, d.

Figure 5.9 shows the comparison of the full susceptibility chart obtained from analytical calculations described in section 5.1.2 (solid lines), MC simulation described in section 5.1.3 (red dotted regions), and the CST simulation described in this section (black dotted regions). We observe that there is excellent agreement between the MC and the CST simulation. Typical simulation times to generate a full susceptibility diagram (black dots in Fig. 5.9) were on the order of a few hours to a day using a PC with two 12-core Intel Xeon E5-2687WV4 processors.

The difference between the MC and CST simulation is mainly due to the fact that the MC model used here is a simplified single macroparticle model. Another reason is the different energy distribution of secondary electron emission used: in MC, all the emitted secondary electrons are assumed to be contained in a single macroparticle which is then emitted from the surface following the energy and angle distributions given by Eq (2.6); whereas in CST, discrete secondary electrons are emitted with energies following the gamma distribution (red curve in Fig. 5.8(b)) which is different from the distribution used in the MC simulation (black curve in Fig. 5.8(b)). In addition, as a result of the polar angle distribution of the emitted secondary electrons in CST given by Eq. (5.13), there is a lateral diffusion of electrons in the 3-dimensional CST simulation, as can be observed from Fig. 5.10.

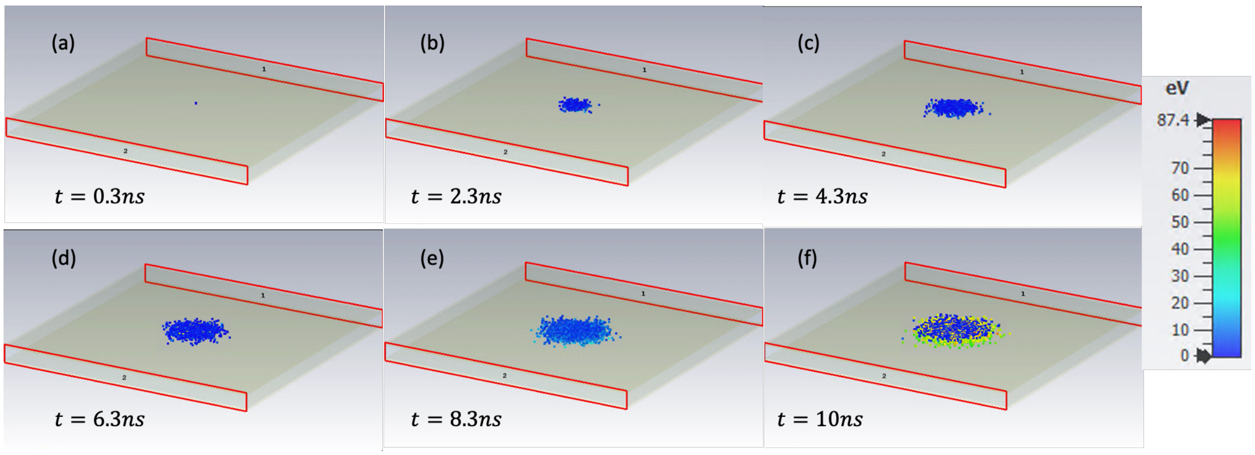

Figure 5.10. Evolution of the multipactor discharge with, $V_{rf} = 99\text{V}$, $fd = 0.9902$ GHz · mm, $f = 1$ GHz, $d = 0.9902$ mm.

5.2. Analysis for Two-Frequency RF Field Induced Multipactor

5.2.1. Electron Dynamics

As described in Chapter 2 Section 2.1, the two frequency rf electric field can be described as $E_y = [E_{rf}\sin(\omega t + \theta) + \beta E_{rf}\sin(n(\omega t + \theta) + \gamma)]$. Here E_{rf} is the peak electric field strength, ω is the angular frequency, and θ is the initial phase of the electric field, of the fundamental carrier mode. β is the field strength of the second carrier mode relative to the fundamental mode, γ is the relative phase of the second carrier mode when $(\omega t + \theta) = 0$ or integer multiple of 2π, and n is the ratio of the two carrier frequencies. Therefore, the force law governing the electron trajectories for the two frequency rf field is as follows,

$$a(t) = \frac{eV_{rf}}{md}[sin(\omega t + \theta) + \beta\sin(n(\omega t + \theta) + \gamma)], \tag{5.14}$$

The velocity of the electron is obtained as,

$$v = \frac{eV_{rf}}{m\omega d}\left\{cos\theta - \cos(\omega t + \theta) + \frac{\beta}{n}[\cos(n\theta + \gamma) - \cos(n(\omega t + \theta) + \gamma)]\right\} + v_0 sin\phi. \quad (5.15)$$

and the instantaneous position of a multipactor electron is obtained as,

$$y = \frac{eV_{rf}}{m\omega^2 d}\left\{\omega t cos\theta - \sin(\omega t + \theta) + sin\theta + \frac{\beta}{n}[n\omega t cos(n\theta + \gamma) - \sin(n(\omega t + \theta) + \gamma) + sin(n\theta + \gamma)]\right\} + v_0 t sin\phi + y_0. \quad (5.16)$$

5.2.2. Analytical Model

Developing a general analytical model for the two-frequency rf operation is not as straightforward as that of the single frequency rf operation. This is due to the fact that for two-frequency rf operation, there can be infinite number of the rf waveshape for different combinations of $n, \beta,$ and γ. From our discussion in section 5.1.2, it is clear that the electron transit time between the parallel plates is dependent on the rf waveshape. Therefore, unlike the single frequency case, a general assumption cannot be made about the electron transit time for the two-frequency case that will work for arbitrary combinations of $n, \beta,$ and γ. In the next sections, we resort to the Monte Carlo and CST simulations to study the two-frequency rf operation.

5.2.3. Monte Carlo and CST Simulation

We follow the same MC simulation procedure described in section 5.1.3 and construct the multipactor charts for the two frequency rf fields. Figure 5.11 shows the multipactor susceptibility charts calculated from MC simulations for random emission energy and emission angle following Eqs. 2.6, and also from CST simulations, for the cases with relative strength of the second carrier $\beta = 1$, frequency ratio between the two carrier modes $n = 2$, and relative phase of the second carrier $\gamma = 0, \pi/2,$ and $3\pi/4$. It is important to note here that along the horizontal axis of the two-frequency susceptibility chart, we have the product of the fundamental rf frequency, f, and the gap distance, d.

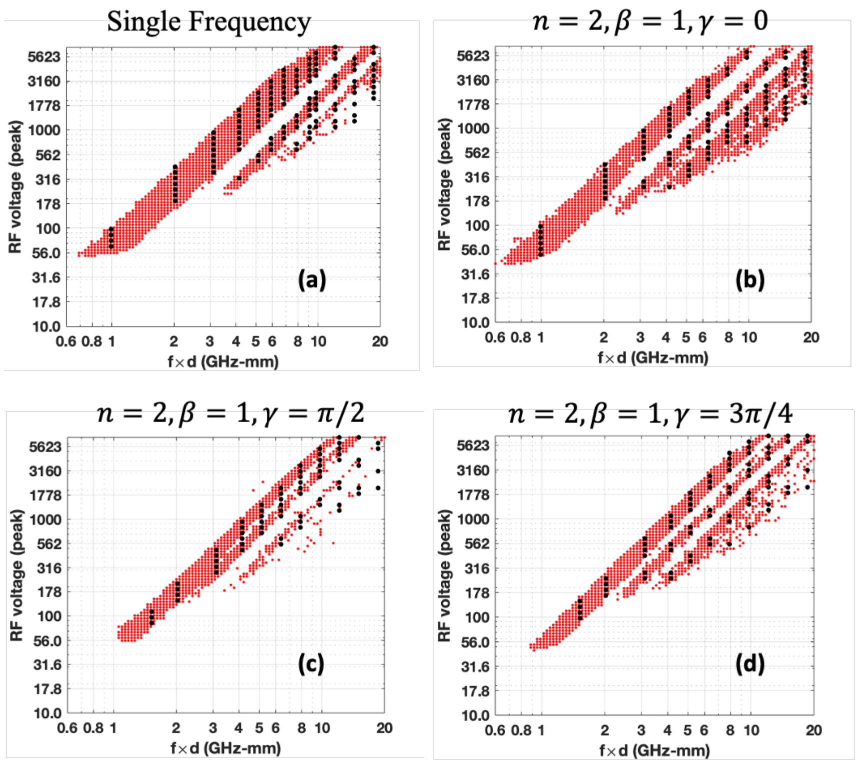

Figure 5.11. Multipactor susceptibility charts calculated from MC simulation (red dotted regions) for random emission voltage and emission angle and from CST simulation (black dotted regions) for (a) single frequency rf operation, which is the same as Fig. 5.9 above, (b) relative strength of the second carrier $\beta = 1$, frequency ratio between the two carrier modes $n = 2$, and relative phase of the second carrier, $\gamma = 0$, (c) $n = 2, \beta = 1, \gamma = \pi/2$, and (d) $n = 2, \beta = 1, \gamma = 3\pi/4$. The CST simulation is conducted for $fd = 1, 2, 3, 4, 5, 6, 7, 8, 9, 10, 12, 15$, and 18 GHz · mm. For all the cases, we use fundamental rf frequency, $f = 1$GHz, and variation of fd is obtained by varying the gap distance, d.

Figure 5.11 shows that multipactor susceptibility regions are sensitive to the relative phase γ of the second carrier mode. As γ increases from $\gamma = 0$ to $\pi/2$, and $3\pi/4$, the multipactor susceptibility regions slightly shrink. This agrees with previous results of V. Semenov [39] and can be attributed to the modulation of rf envelope by the second carrier mode. The susceptibility regions have the smallest area for $\gamma = \pi/2$. The difference between the MC and the CST results can be attributed to the differences between the two methods as described in section 5.1.5.

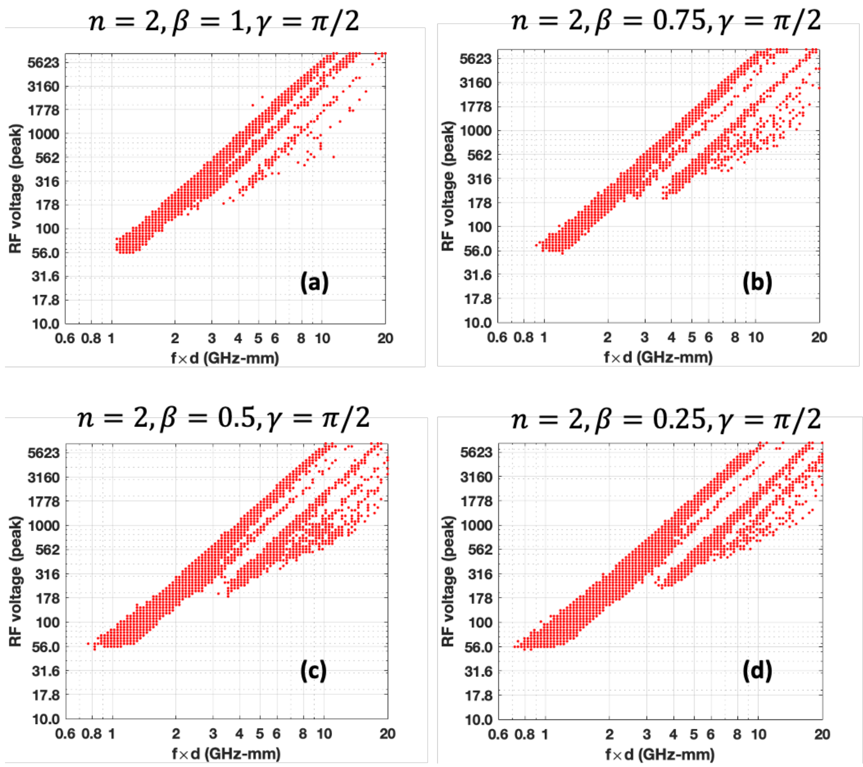

Figure 5.12. Multipactor susceptibility charts calculated from MC simulation (red dotted regions) for random emission voltage and emission angle for frequency ratio between the two carrier modes, $n = 2$, relative phase of the second carrier, $\gamma = \pi/2$, and relative strength of the second carrier (a) $\beta = 1$, (b) $\beta = 0.75$, (c) $\beta = 0.5$ and (d) $\beta = 0.25$. For all the cases, we use fundamental rf frequency, $f = 1$GHz, and variation of fd is obtained by varying the gap distance, d.

Figure 5.12 shows that as the relative strength of the second carrier mode decreases, the effect of the second carrier mode becomes less prominent on the susceptibility chart, as the chart gradually approaches that of single frequency operation. This has also been previously observed for single surface multipactor discharge with two-frequency rf fields [125].

5.2.4. Electron Trajectories and Multipactor Modes

As discussed before in section 5.2.2, multipactor modes cannot be rigidly defined for two-frequency rf operation. However, careful examination of the particle trajectories for points at different regions in the susceptibility chart leads to a few interesting observations.

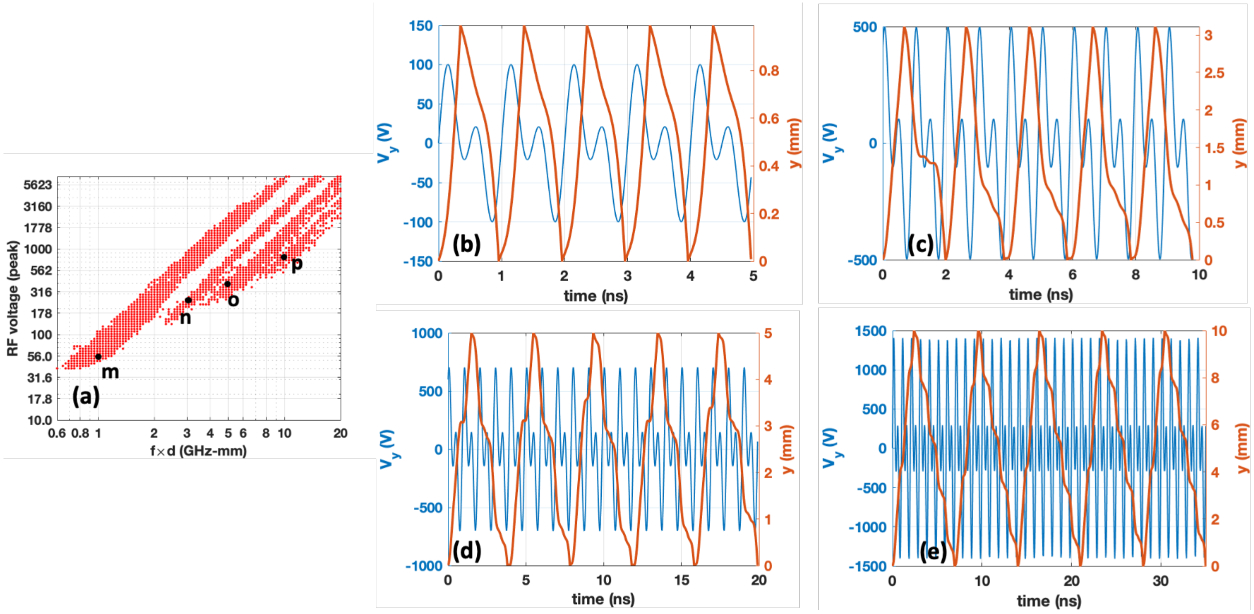

Figure 5.13. (a) Multipactor susceptibility chart for two-frequency rf operation with frequency ratio between the two carrier modes, $n = 2$, relative strength of the second carrier mode, $\beta = 1$, and relative phase of the second carrier mode, $\gamma = 0$ calculated from MC simulation for random emission voltage and emission angle. (b)-(e): Instantaneous rf voltage (blue lines) and corresponding macroparticle trajectories (red lines) for (b) $V_{rf} = 56.86\text{V}$, $fd = 0.9902$ GHz · mm, (c) $V_{rf} = 283\text{V}$, $fd = 3.112$ GHz · mm, (d) $V_{rf} = 400\text{V}$, $fd = 5$ GHz · mm, and (e) $V_{rf} = 800\text{V}$, $fd = 10\text{GHz} \cdot \text{mm}$. For all the cases, we use fundamental rf frequency, $f = 1\text{GHz}$, and variation of fd is obtained by varying the gap distance, d. Plots (b)-(e) correspond to the points m, n, o, and p in the susceptibility chart in (a), respectively.

For a single multipactor mode in single frequency rf operation, the transit time of the macroparticle from the top plate to the bottom plate and the transit time from the bottom plate to the top plate are equal. However, for the two frequency rf operation, we frequently observe mixed multipactor modes where the two transit times are not equal to each other, and yet the time for a complete round trip of the particle remains fixed.

For example, Fig 5.13(b) shows a case of two frequency operation with $\beta = 1, n = 2, \gamma = \pi/2$, $V_{rf} = 56.86\text{V}$, $fd = 0.9902$ GHz · mm, the transit time from bottom plate to top plate, $\tau_{AB} = 0.4\text{ns}$, and the transit time from bottom plate to top plate, $\tau_{BA} = 0.6\text{ns}$. The total time required for the round trip is therefore, $\tau_{round} = 1ns$. The corresponding point m is shown in the susceptibility chart in Fig. 5.13(a).

In the case of Fig 5.13(c) with $V_{rf} = 283\text{V}$, $fd = 3.112\ \text{GHz} \cdot \text{mm}$, we have $\tau_{AB} = 0.8\text{ns}$, and $\tau_{BA} = 1.2\text{ns}$. The total time required for the round trip is therefore, $\tau_{round} = 2ns$. The corresponding point n is shown in the susceptibility chart in Fig. 5.13(a). Similarly, for the cases of Figs. 5.13(d)-(e), we have $\tau_{AB} = 1.5\text{ns}$ and 2.5ns, respectively and $\tau_{BA} = 2.5\text{ns}$ and 4.5ns, respectively. The total time required for the round trips are therefore, $\tau_{round} = 4\text{ns}$ and 7ns, respectively. The corresponding points o and p are shown in the susceptibility chart in Fig. 5.13(a).

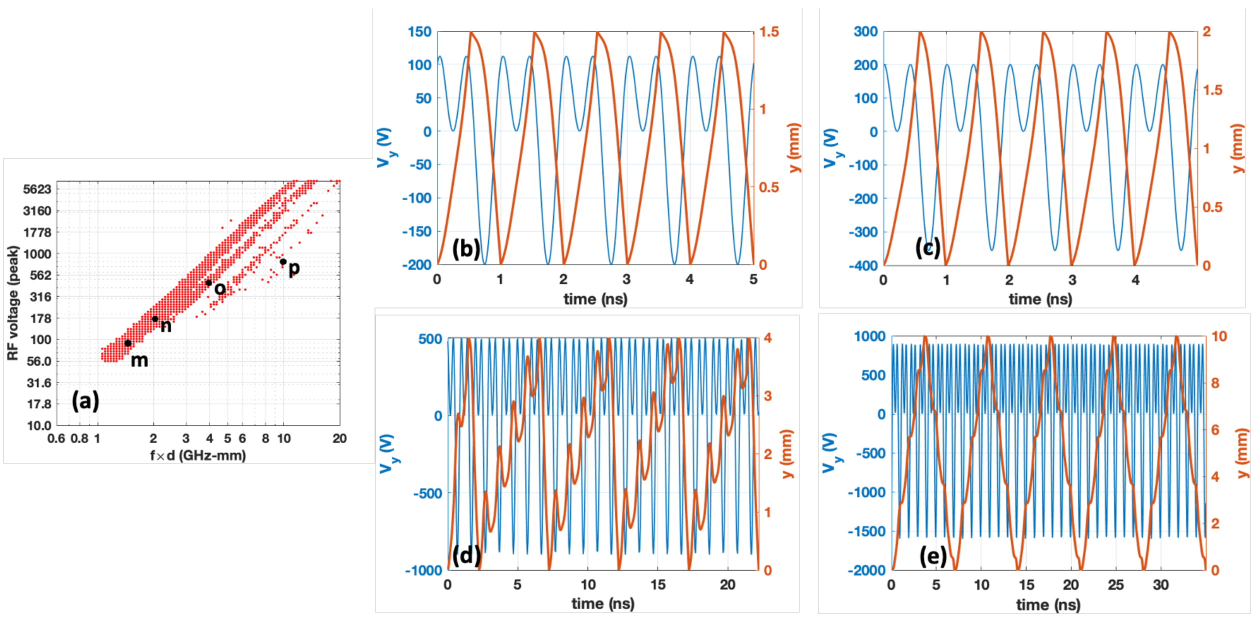

Figure 5.14. (a) Multipactor susceptibility chart for two-frequency rf operation with frequency ratio between the two carrier modes, $n = 2$, relative strength of the second carrier mode, $\beta = 1$, and relative phase of the second carrier mode, $\gamma = \pi/2$ calculated from MC simulation for random emission energy and emission angle. (b)-(e): Instantaneous rf voltage (blue lines) and corresponding macroparticle trajectories (red lines) for (b) $V_{rf} = 100\text{V}$, $fd = 1.5\ \text{GHz} \cdot \text{mm}$, (c) $V_{rf} = 178\text{V}$, $fd = 2\ \text{GHz} \cdot \text{mm}$, (d) $V_{rf} = 450\text{V}$, $fd = 4\ \text{GHz} \cdot \text{mm}$, and (e) $V_{rf} = 800\text{V}$, $fd = 10\text{GHz} \cdot \text{mm}$. For all the cases, we use fundamental rf frequency, $f = 1\text{GHz}$, and variation of fd is obtained by varying the gap distance, d. Plots (b)-(e) correspond to the points m, n, o, and p in the susceptibility chart in (a), respectively.

Figure 5.14 shows similar mixed multipactor modes for $\beta = 1, n = 2, \gamma = \pi/2$ where τ_{AB} and τ_{BA} are different, but τ_{round} is fixed. For Figs. 5.14(b)-(e) we have four cases with $\tau_{round} =$ 1ns, 1ns, 5ns, and 7ns respectively.

5.3. Preliminary Results on Space Charge Effect

In addition to a Particle-in-Cell (PIC) solver without space charge effect, CST also offers a PIC solver with space charge effect [88,133]. Next, we turn on the space charge effect and run the simulation for single frequency rf operation to examine the effect of space charge on the time dependent physics and multipactor susceptibility.

5.3.1. Space Charge Effect on the Time Dependent Physics

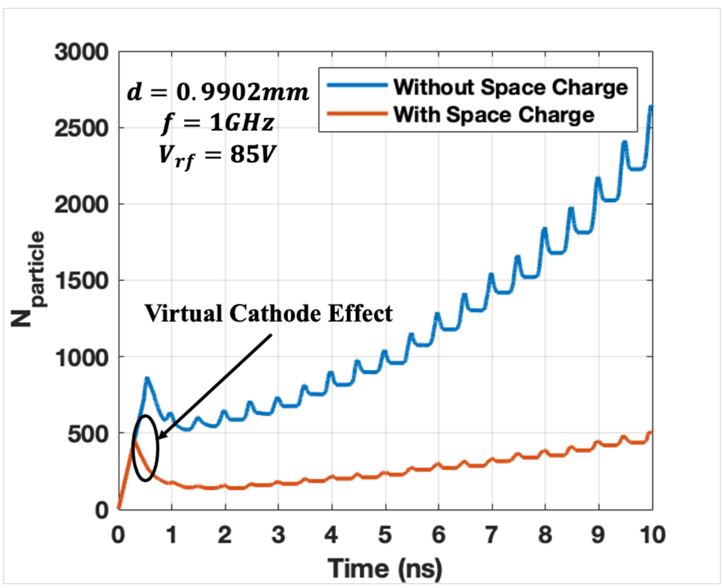

Figure 5.15. Number of particles vs time in CST with peak rf voltage, $V_{rf} = 85$V, gap distance $d = 0.9902$mm, and rf frequency $f = 1$GHz without space charge effect (blue curve), with the space charge effect (red curve). The total number of seed particles in the simulation, $N_{seed,total} = 1515$, and the number of electrons contained in each particle, $N_e = 10^5$.

First, we try to understand how space charge affects multipactor electron dynamics and the time dependent physics. As an example case, we choose the point in the susceptibility chart with $V_{rf} = 85$V, and $fd = 1$GHz $\cdot$ mm. We can observe from Figs. 5.15 that the growth rate of electron population without space charge is much higher than the growth rate of electron population with space charge. Both cases result in an exponential growth of electrons with the secondary electron yield, $\delta > 1$. Therefore, space charge significantly affects the time dependent physics of multipactor discharge. Figure 5.16 shows the three-dimensional picture of the evolution of electron population in the system with and without space charge.

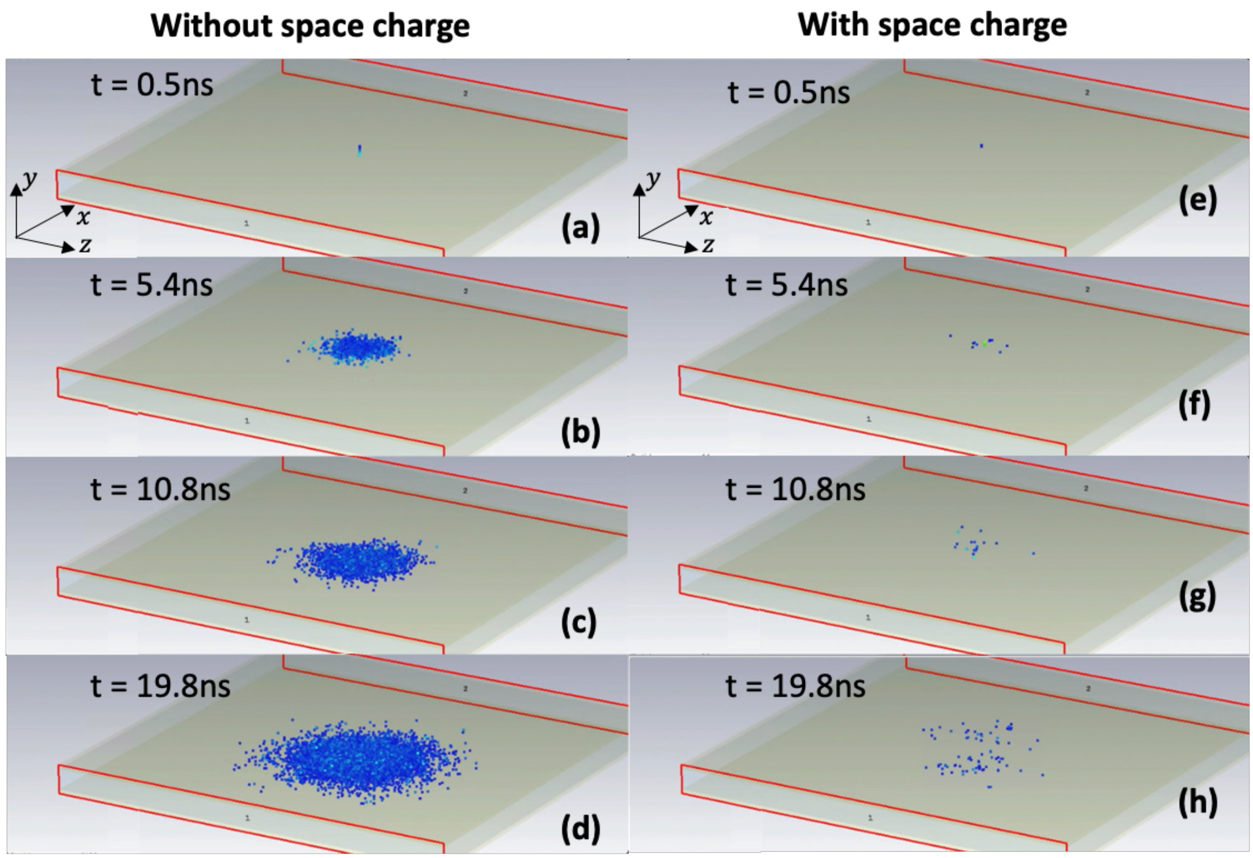

Figure 5.16. Three-dimensional pictures of the evolution of multipactor discharge (a)-(d): without space charge, (e)-(h): with space charge, for $V_{rf} = 85$V, $f = 1$ GHz, $d = 0.9902$ mm. The total number of seed particles in the simulation, $N_{seed,total} = 1515$, and the number of electrons contained in each particle, $N_e = 10^5$.

To understand why the growth rate of electron population without space charge is higher compared to that with space charge, we examine the y-directional position (y)-velocity (v_y) phase space. Figure 5.17(a)-(c) show that when space charge effect is absent, the number of seed particles increases linearly from $N_{seed} = 456$ to $N_{seed} = 797$ from time $t = 0.3ns$ to $t = 0.5ns$ according to the input assigned in CST. These seed particles impact the bottom plate near the time $t = 0.5ns$ and the impact velocity of the primary particles for these impacts, $v_i > 4 \times 10^6 m/s$ (Fig. 5.17(c)). At $t = 0.5ns$, the electric field reverses direction and then the emitted secondary particles are accelerated toward the top plate. These secondary particles impact the top plate near the time $t = 1ns$ (Fig 5.17(g)).

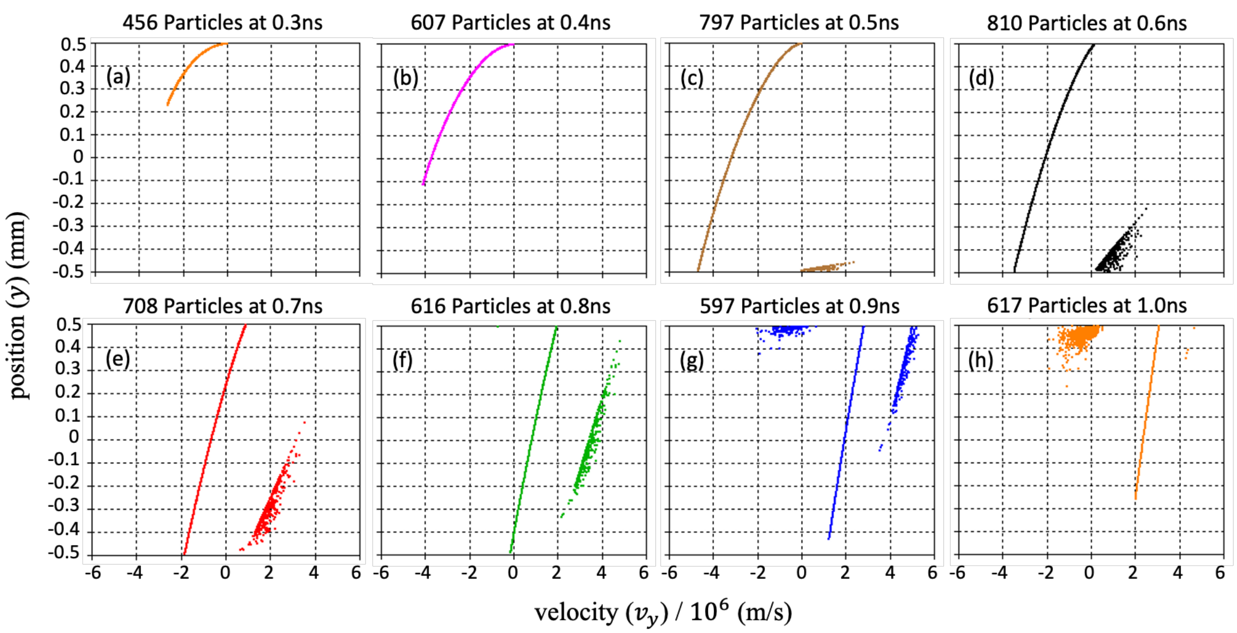

Figure 5.17. y vs v_y without space charge for $V_{rf} = 85$V, $f = 1$ GHz, $d = 0.9902$ mm at times (a) $t = 0.3T_{rf}$, (b) $t = 0.4T_{rf}$, (c) $t = 0.5T_{rf}$, (d) $t = 0.6T_{rf}$, (e) $t = 0.7T_{rf}$, (f) $t = 0.8T_{rf}$, (g) $t = 0.9T_{rf}$, (h) $t = 1.0T_{rf}$, where $T_{rf} = 1$ns is the rf period. The total number of seed particles in the simulation is set as $N_{seed,total} = 1515$, and the number of electrons contained in each particle, $N_e = 10^5$.

However, electron dynamics changes significantly in the presence of space charge. Figures 5.17(a) and 5.18(a) show that at time $t = 0.3ns$, the number of seed particles with space charge is equal to the number of seed particles without space charge ($N_{seed} = 456$ for both cases). However, at $t = 0.4ns$, we only observe $N_{seed} = 371$ with space charge (Fig.5.18(b)) compared to $N_{seed} = 607$ without space charge (Fig. 5.17(b)). This happens because when space charge effect is accounted for, seed particles emitted from the surface at a later time are repelled by the seed particles emitted during the early period and consequently they are absorbed by the emitting surface (top plate). This is due to the virtual cathode effect [134–138] which is also shown in Fig. 5.15. In addition, space charge repulsion decreases the acceleration of the seed particles by the electric field. Therefore, we observe that the velocities of the seed particles with space charge effect (Figs. 5.18(a)-(c)) are significantly lower than the velocities of the seed particles without space charge effect (Figs. 5.17(a)-(c)). As a result, the primary particles fail to reach the bottom plate at $t = 0.5ns$ (Fig. 5.18(c)) when the electric field reverses direction, i.e., the resonance condition discussed in Section 5.1.1 is not met. The reversed electric field decelerates the seed particles, and they impact the bottom plate with velocities $v_y < 4 \times 10^6 m/s$ (Fig. 5.18(d)) resulting in a lower SEY compared to that without space charge effect. In addition, many of the emitted secondary particles are absorbed by the emitting surface due to the virtual cathode effect.

Therefore, the lower growth rate of electron population with space charge effect can be attributed to the virtual cathode effect, the disruption of resonant electron motion, and low SEY due to low impact energy of the primary electrons.

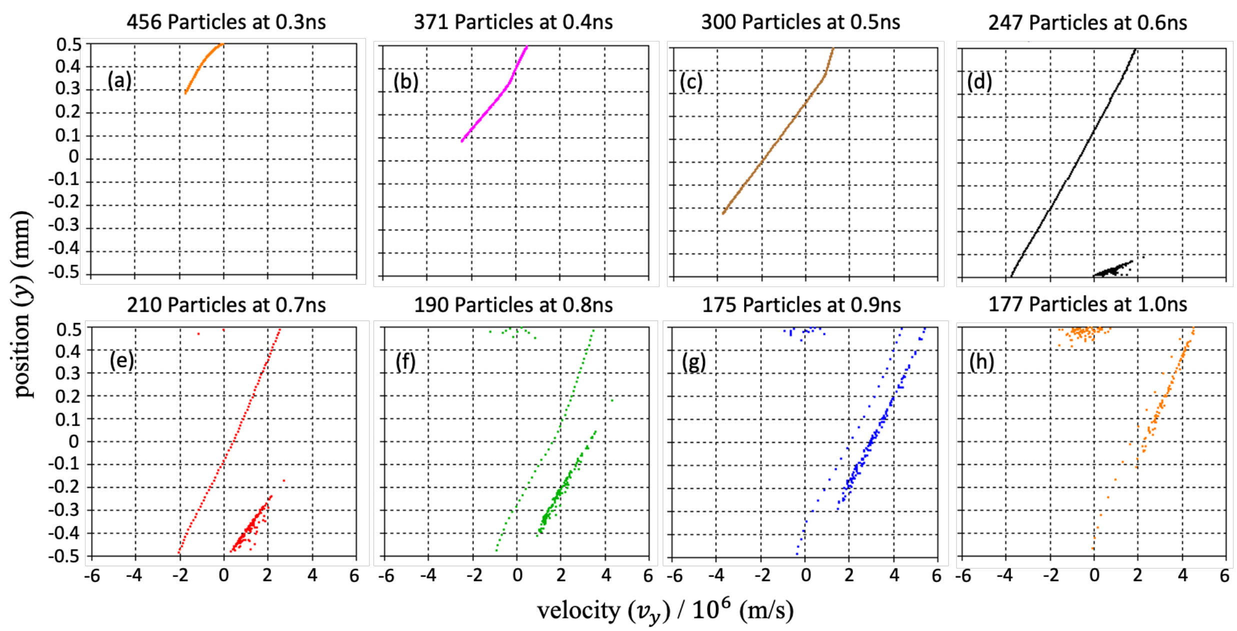

Figure 5.18. y vs v_y with space charge for $V_{rf} = 85$V, $f = 1$ GHz, $d = 0.9902$ mm at times (a) $t = 0.3T_{rf}$, (b) $t = 0.4T_{rf}$, (c) $t = 0.5T_{rf}$, (d) $t = 0.6T_{rf}$, (e) $t = 0.7T_{rf}$, (f) $t = 0.8T_{rf}$, (g) $t = 0.9T_{rf}$, (h) $t = 1.0T_{rf}$, where $T_{rf} = 1$ns is the rf period. The total number of seed particles in the simulation is set as $N_{seed,total} = 1515$, and the number of electrons contained in each particle, $N_e = 10^5$.

5.3.2. Space Charge Effect with Different Total Volume Charge

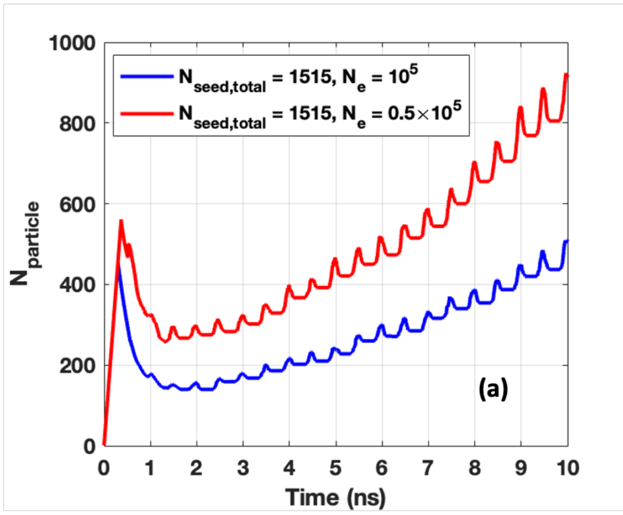

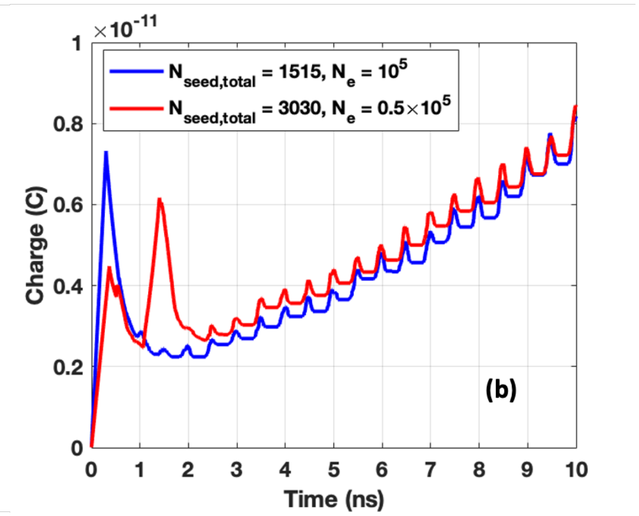

Figure 5.19. (a) Number of particles vs time for the number of electrons contained in each particle, $N_e = 10^5$(blue curve) and $N_e = 0.5 \times 10^5$(red curve). For both cases, we use emission period of seed particles, $t_{emission} = 1ns$ and the total number of seed particles, $N_{seed,total} = 1515$. (b) Volume charge vs time with $t_{emission} = 1$ns, $N_{seed,total} = 1515$, $N_e = 10^5$ (blue curve), and $t_{emission} = 2$ns, $N_{seed,total} = 3030$ and $N_e = 0.5 \times 10^5$(red curve). For all the cases, we use $V_{rf} = 85$V, $f = 1$ GHz, $d = 0.9902$ mm.

Figure 5.19(a) shows that with a fixed total number of seed particles, $N_{seed,total}$, as the number of electrons contained in each particle, N_e, increases, space charge effect becomes more prominent. This happens because as N_e increases, the total emitted charge in the volume also increases, making space charge more significant. Thus, it is important to choose a proper N_e in CST simulation in order to have sufficient volume charge to observe the impact of space charge effect.

Figure 5.19(b) shows two multipactor simulation cases in CST with space charge. In one case (blue curve), we use $N_{seed,total} = 1515$ and $N_e = 10^5$. In the other case (red curve), we increase $N_{seed,total}$ by two times ($N_{seed,total} = 3030$) and at the same time decrease N_e by two times ($N_e = 0.5 \times 10^5$), so that the total volume charge for the two cases remain the same. Since the volume charge is the same for the two cases, we observe that the charge growth due to multipactor remains almost the same for the two cases. The major difference between the two cases observed for $t < 2$ns is due to the fact that for the first case (blue curve), seed particles are emitted for $t_{emission} = 1$ns whereas for the second case (red curve), seed particles are emitted for $t_{emission} = 2$ns resulting in some differences in the charge growth between the two cases for $t < 2$ns.

5.3.3. Space Charge Effect on Multipactor Susceptibility

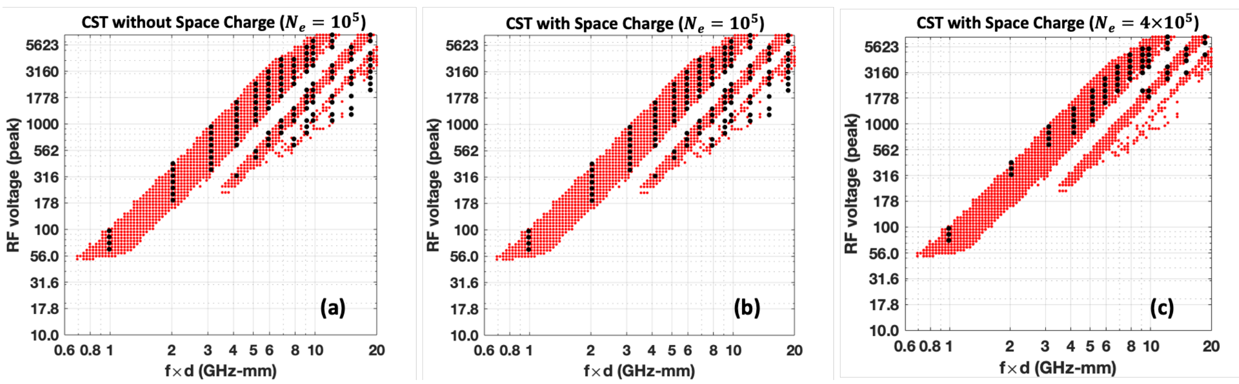

Figure 5.20. Multipactor susceptibility charts for single frequency rf operation calculated from MC simulation without space charge effect (dotted red regions) for random emission energy and emission angle along with (a) CST simulation (black dotted regions) without space charge effect for $N_{seed,total} = 1515$, $N_e = 10^5$. (b) CST simulation with space chare effect for $N_{seed,total} = 1515$, $N_e = 10^5$, and (b) CST simulation with space chare effect for $N_{seed,total} = 1515$,$N_e = 4 \times 10^5$.

We observe from Fig. 5.20(a-b) that the susceptibility charts without space charge effect and with space charge effect are almost identical when we choose $N_e = 10^5$. However, if we increase the total volume charge by choosing $N_e = 4 \times 10^5$ (Fig. 5.20(c)), space charge effect on multipactor susceptibility becomes more prominent, as described in Section 5.3.2. As a result, multipactor susceptibility bands shrink when space charge increases. This trend agrees with previous study conducted by G. Romanov [139].

The difference in the susceptibility charts with and without space charge effect can be explained from the time dependent physics described in Section 5.3.1. Due to the virtual cathode effect induced by space charge as well as the low impact energy of primary electrons leading to low SEY of impacts, a higher electric field is required to initiate multipactor in the presence of space charge which results in the upwards shift of the lower multipactor susceptibility boundary. For the upper boundary, in the presence of the repulsive space charge field, a lower RF electric field is required to make sure the emitted electrons do not back strike the original emitting surface (cf. Fig. 5.2). As a result, the presence of space charge leads to the shrinkage of the susceptibility bands in Fig. 5.20(c).

5.3.4. Space Charge Induced Multipactor Saturation

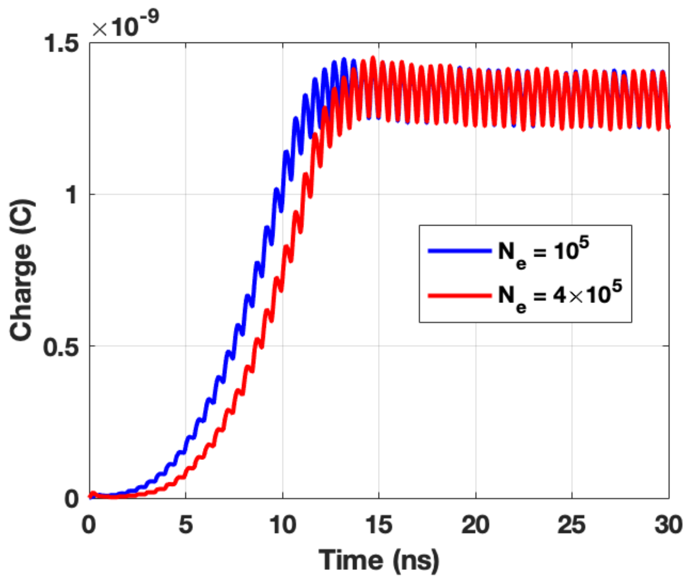

Figure 5.21. Multipactor saturation in CST simulation due to space charge effect with $N_e = 10^5$ (blue curve), and $N_e = 4 \times 10^5$(red curve). For both cases, we use $N_{seed,total} = 1515$, $V_{rf} = 369.6\text{V}$, $f = 1$ GHz, and $d = 2.02$ mm.

Previous studies [50,53,139] have concluded that space charge plays a significant role in two-surface multipactor saturation mechanism. S. Riyopoulos attributed multipactor saturation to two synergistic effects: spreading of the impact phases into the region where the vacuum rf retards emission and field reversal in the front end of the bunch due to the space-charge field [53]. In our CST simulation, we observe multipactor saturation with space charge effect when the simulation is conducted for a long time period (30ns in Fig. 5.21). However, when the same simulation is conducted in the absence of space charge effect, the number of particles keep increasing indefinitely, since there is no saturation mechanism, and eventually the program crashes.

Figure 5.21 also shows that the multipactor saturation level, in terms of total charge in the volume, for a given set of inputs does not depend on N_e. The same saturation level is observed for both cases with $N_e = 10^5$ (blue curve), and $N_e = 4 \times 10^5$(red curve) in Fig. 5.21. However, due to the difference in charge growth rate for the two cases, multipactor saturation is obtained at different times.

CHAPTER 6: Summary and Future Works

This dissertation presents a numerical and analytical investigation of multipactor discharge with two carrier frequencies. While multipactor can occur in a system with multiple surfaces and complicated geometries, we focus our study on single-surface and parallel plate geometries with an emphasis on the former.

6.1. On Multipactor Susceptibility and Time Dependent Physics of Single Surface Multipactor Discharge

By employing Monte Carlo simulations and analytical calculations we obtain multipactor susceptibility diagrams on a dielectric in terms of the two-frequency transverse rf electric field and normal surface charging field. We present a novel multiparticle Monte Carlo simulation model in one dimension with adaptive time steps that can calculate the electron flight times *exactly*. We employ this model to investigate the effects of the relative strength and phase, and the frequency separation between the two carriers on time averaged multipactor susceptibility and time dependent physics of multipactor discharge. We show that two frequency operation reduces the multipactor strength compared to single frequency operation with the same total rf power. We demonstrate migration of the multipactor trajectory for different rf field configurations which can be used for directing multipacting electrons to a specific desirable location in the geometry for purposes such as device cleaning or to reduce further susceptibility to multipactor. With small frequency ratio between the two carrier modes, we observe the formation of beat waves in the temporal profiles of the normal electric field due to surface charging.

The multiparticle Monte Carlo simulation scheme presented in this thesis does not account for space charge. However, a more advanced MC simulation scheme may be developed to include the space charge effect without losing the computational speed and simplicity. Developing such an algorithm can be a subject of future research.

Possible future work may also include investigating multipactor discharge due to non-sinusoidal rf waveshapes. Wen *et al.* have studied the time dependent physics of multipactor discharge with transverse Gaussian type electric field [122] using PIC and multiparticle Monte Carlo simulations to demonstrate multipactor suppression. Multipactor susceptibility charts can be constructed for such non sinusoidal rf operation by extending our works in this dissertation. A study on multipactor induced by multi-carrier (more than two frequencies) rf operation can also be of interest for practical applications. Other types of electric field waveforms, such as rectangular or triangular waveforms may have interesting effects on multipactor discharge. Another important domain of future research may include multipactor induced by non-transverse rf modes which will significantly change electron impact energies and angles leading to different secondary electron emission conditions.

6.2. On Frequency Domain Analysis of Single Surface Multipactor

The thesis presents a comprehensive frequency domain analysis of multipactor discharge on single dielectric surface for both single- and two-frequency rf operations. We find that for the single frequency rf operation, the normal electric field consists of pronounced even harmonics of the driving rf frequency and the strength of a harmonic component in the normal electric field is a function of its frequency and the incident rf amplitude. We propose an empirical relation between the strength and frequency of the harmonics and the input rf amplitude. For two frequency rf operation, we observe spectral peaks are in the amplitude spectrum of the normal electric field at various frequencies of intermodulation product of the rf carrier frequencies. We propose empirical relations between the heights of different spectral peaks and the input rf amplitudes.

To the knowledge of the author, the frequency components of the surface charging field associated with single surface multipactor discharge have not been investigated in experiments. Diagnosis and harvesting of these frequency components may be an interesting research pursuit for future. These frequency components may be useful in various applications, such as harmonic generation [113]. Future research may also include the effect of these frequency components on transmitted rf signal quality [36]. Our research on the frequency domain analysis of multipactor can also be extended to multi-frequency rf operation.

6.3. On Two Surface Multipactor

We investigate two surface multipactor with two frequency rf fields using Monte Carlo and CST simulation. We observe that multipactor susceptibility is sensitive to the relative strength and phase of the second carrier mode. Multipactor susceptibility regions can become smaller with two frequency rf operation. Regions of single and mixed multipactor modes are observed in the susceptibility chart. For these mixed multipactor modes, electrons take fixed times to complete a round trip between the two surfaces. However, the required times of the electrons to traverse the gap once during each round trip are different. An analytical model for these mixed multipactor modes may be developed in future. The effect of non-integer frequency separation on two surface multipactor may be examined. The connection between single and two surface multipactor may also be investigated.

CST simulation with space charge reveals that space charge largely changes the time dependent physics of multipactor discharge. Electron growth rate is smaller with space charge than without it. This happens due to virtual cathode effect, disruption of resonant electron motion, and low SEY due to low impact energy of primary electrons due to space charge. Since a higher electric field is required to overcome these effects and initiate multipactor discharge, susceptibility bands in the multipactor susceptibility chart shrink in the presence of space charge effect.

In addition to two surface geometry, CST simulation may be employed in future to study a variety of geometries such as coaxial, rectangular, microstrip, circular, and elliptical waveguides. CST may also be employed in the frequency domain analysis of multipactor for these geometries.

REFERENCES

REFERENCES

[1] P. T. Farnsworth, *Television by Electron Image Scanning*, Journal of the Franklin Institute **218**, 411 (1934).

[2] J. R. M. Vaughan, *Multipactor*, IEEE Transactions on Electron Devices **35**, 1172 (1988).

[3] R. A. Kishek, Y. Y. Lau, L. K. Ang, A. Valfells, and R. M. Gilgenbach, *Multipactor Discharge on Metals and Dielectrics: Historical Review and Recent Theories*, Physics of Plasmas **5**, 2120 (1998).

[4] R. A. Kishek and Y. Y. Lau, *Multipactor Discharge on a Dielectric*, Physical Review Letters **80**, 193 (1998).

[5] P. Zhang, Y. Y. Lau, M. Franzi, and R. M. Gilgenbach, *Multipactor Susceptibility on a Dielectric with a Bias Dc Electric Field and a Background Gas*, Physics of Plasmas **18**, 053508 (2011).

[6] A. J. Hatch and H. B. Williams, *The Secondary Electron Resonance Mechanism of Low-Pressure High-Frequency Gas Breakdown*, Journal of Applied Physics **25**, 417 (1954).

[7] A. J. Hatch and H. B. Williams, *Multipacting Modes of High-Frequency Gaseous Breakdown*, Physical Review **112**, 681 (1958).

[8] H. Bruining, J. H. De Boer, and W. G. Burgers, *Secondary Electron Emission of Soot in Valves with Oxidecathode*, Physica **4**, 267 (1937).

[9] A. J. Dekker, *Secondary Electron Emission*, in *Solid State Physics*, edited by F. Seitz and D. Turnbull, Academic Press, Vol. 6, pp. 251–311 (1958).

[10] J. R. M. Vaughan, *A New Formula for Secondary Emission Yield*, IEEE Transactions on Electron Devices **36**, 1963 (1989).

[11] M. Furman and M. Pivi, *Probabilistic Model for the Simulation of Secondary Electron Emission*, Phys. Rev. ST Accel. Beams **5**, 124404 (2002).

[12] A. A. Neuber, M. Butcher, H. Krompholz, L. L. Hatfield, and M. Kristiansen, *The Role of Outgassing in Surface Flashover under Vacuum*, IEEE Transactions on Plasma Science **28**, 1593 (2000).

[13] D. H. Preist and R. C. Talcott, *On the Heating of Output Windows of Microwave Tubes by Electron Bombardment*, IRE Transactions on Electron Devices **8**, 243 (1961).

[14] J. R. M. Vaughan, *Some High-Power Window Failures*, IRE Transactions on Electron Devices **8**, 302 (1961).

[15] S. Yamaguchi, Y. Saito, S. Anami, and S. Michizono, *Trajectory Simulation of Multipactoring Electrons in an S-Band Pillbox RF Window*, IEEE Transactions on Nuclear Science **39**, 278 (1992).

[16] A. Neuber, J. Dickens, D. Hemmert, H. Krompholz, L. L. Hatfield, and M. Kristiansen, *Window Breakdown Caused by High-Power Microwaves*, IEEE Transactions on Plasma Science **26**, 296 (1998).

[17] T. P. Graves, Experimental Investigation of Electron Multipactor Discharges at Very High Frequency, Ph.D. Thesis, Massachusetts Institute of Technology (2006).

[18] F. Höhn, W. Jacob, R. Beckmann, and R. Wilhelm, *The Transition of a Multipactor to a Low-Pressure Gas Discharge*, Physics of Plasmas **4**, 940 (1997).

[19] T. P. Graves, S. J. Wukitch, B. LaBombard, and I. H. Hutchinson, *Effect of Multipactor Discharge on Alcator C-Mod Ion Cyclotron Range of Frequency Heating*, Journal of Vacuum Science & Technology A: Vacuum, Surfaces, and Films **24**, 512 (2006).

[20] J. D. Cobine, *Gaseous Conductors*, Dover Publications Inc., New York (1958). https://biblio.co.uk/book/gaseous-conductors-cobine-jd/d/723026587.

[21] J. H. Booske, *Plasma Physics and Related Challenges of Millimeter-Wave-to-Terahertz and High Power Microwave Generation*, Phys. Plasmas **15**, 17 (2008).

[22] R. J. Barker, N. C. Luhmann, J. H. Booske, and G. S. Nusinovich, *Modern Microwave and Millimeter Wave Power Electronics,* IEEE Press, Piscataway, Hoboken, N.J. (2004).

[23] J. W. Luginsland, T. Antonsen, J. P. Verboncoeur, R. W. Lemke, L. Ludeking, P. Mardahl, A. T. Lin, Y. Y. Lau, and J. D. Blahovec, *High Power Microw. Sources Technology,* Edited by E. Schamiloglu and R. J. Barker, Wiley/IEEE Press, New York, N.Y. (2001), p. 376.

[24] D. Shiffler, T. K. Statum, T. W. Hussey, O. Zhou, and P. Mardahl, *Mod. Microw. Millim. Wave Power Electron.*, IEEE, Piscataway, N.J. (2005), p. 691.

[25] P. Wong, P. Zhang, and J. Luginsland, *Recent Theory of Traveling-Wave Tubes: A Tutorial-Review*, Plasma Res. Express **2**, 023001 (2020).

[26] J. Benford, J. A. Swegle, and E. Schamiloglu, *High Power Microwaves*, 2nd ed. CRC Press, New York, 2007.

[27] N. Rozario, H. F. Lenzing, K. F. Reardon, M. S. Zarro, and C. G. Baran, *Investigation of Telstar 4 Spacecraft Ku-Band and C-Band Antenna Components for Multipactor Breakdown*, IEEE Transactions on Microwave Theory and Techniques **42**, 558 (1994).

[28] S. Anza, C. Vicente, J. Gil, V. E. Boria, B. Gimeno, and D. Raboso, *Nonstationary Statistical Theory for Multipactor*, Physics of Plasmas **17**, 062110 (2010).

[29] S. Anza, M. Mattes, C. Vicente, J. Gil, D. Raboso, V. E. Boria, and B. Gimeno, *Multipactor Theory for Multicarrier Signals*, Physics of Plasmas **18**, 1 (2011).

[30] S. Anza, C. Vicente, J. Gil, M. Mattes, D. Wolk, U. Wochner, V. E. Boria, B. Gimeno, and D. Raboso, *Multipactor Prediction with Multi-Carrier Signals: Experimental Results and Discussions on the 20-Gap-Crossing Rule*, 8th European Conference on Antennas and Propagation (EuCAP), Hague, The Netherlands (2014), pp. 1638–1642.

[31] S. Anza, C. Vicente, J. Gil, V. E. Boria, and D. Raboso, *Experimental Verification of Multipactor Prediction Methods in Multicarrier Systems*, 46th European Microwave Conference (EuMC), London, UK (2016), pp. 226–229.

[32] S. Anza, C. Vicente, B. Gimeno, V. E. Boria, and J. Armendáriz, *Long-Term Multipactor Discharge in Multicarrier Systems*, Physics of Plasmas **14**, 082112 (2007).

[33] A. Sazontov, V. Semenov, M. Buyanova, N. Vdovicheva, D. Anderson, M. Lisak, J. Puech, and L. Lapierre, *Multipactor Discharge on a Dielectric Surface: Statistical Theory and Simulation Results*, Physics of Plasmas **12**, 093501 (2005).

[34] V. E. Semenov, N. Zharova, R. Udiljak, D. Anderson, M. Lisak, and J. Puech, *Multipactor in a Coaxial Transmission Line. II. Particle-in-Cell Simulations*, Physics of Plasmas **14**, 033509 (2007).

[35] A. A. Hubble, M. S. Feldman, P. T. Partridge, and R. Spektor, *Evolution of Multipactor Breakdown in Multicarrier Systems*, Physics of Plasmas **26**, 053502 (2019).

[36] P. Y. Wong, Y. Y. Lau, P. Zhang, N. Jordan, R. M. Gilgenbach, and J. Verboncoeur, *The Effects of Multipactor on the Quality of a Complex Signal Propagating in a Transmission Line*, Physics of Plasmas **26**, 112114 (2019).

[37] Special Sessions on Multipactor, I and II, IEEE ICOPS, Denver, CO, June,2018.

[38] David Raboso, *Multipactor RF breakdown at ESA: testing techniques, R&D investigations and standards,* WMH Workshop, IMS 2007. *Https://Ece.Uwaterloo.ca/~mingyu/MTTs2007/4.Pdf*.

[39] V. Semenov, A. Kryazhev, D. Anderson, and M. Lisak, *Multipactor Suppression in Amplitude Modulated Radio Frequency Fields*, Physics of Plasmas **8**, 5034 (2001).

[40] A. Iqbal, J. Verboncoeur, and P. Zhang, *Multipactor Susceptibility on a Dielectric with Two Carrier Frequencies*, Physics of Plasmas **25**, 043501 (2018).

[41] F. Piro and Y. Brand, *PIM and Multipactor Considerations for Future High-RF Power Space Missions*, 8th European Conference on Antennas and Propagation (EuCAP), Hague, The Netherlands (2014), pp. 1643–1646.

[42] S. Anza, C. Vicente, J. Gil, M. Mattes, D. Wolk, U. Wochner, V. E. Boria, B. Gimeno, and D. Raboso, *Prediction of Multipactor Breakdown for Multicarrier Applications: The Quasi-Stationary Method*, IEEE Transactions on Microwave Theory and Techniques **60**, 2093 (2012).

[43] C. Gutton and H. Gutton, Compt. Rend. **186(303)**, (1928).

[44] P. T. Farnsworth, *Multipactor*, Technical Report 2135615 (1938).

[45] P. T. Farnsworth, *Multipactor Oscillator*, Technical Report 2137528 (1938).

[46] P. T. Farnsworth, *Multipactor Oscillator and Amplifier*, Technical Report 2091439 (1937).

[47] P. T. Farnsworth, *Multipactor Phase Control*, Technical Report 2071517 (1938).

[48] W. Henneburg, R. Orthuber, and E. Steudel, *Zur Wirkungsweise Des Elektronenvervielfachers*, Z. Tech. Phys. **17**, 115 (1936).

[49] E. W. B. Gill and A. von Engel, *Starting Potentials of High-Frequency Gas Discharges at Low Pressure*, Proc. R. Soc. Lond. A **192**, 446 (1948).

[50] R. A. Kishek, Interaction of Multipactor Discharge And rf Structures, Ph.D. Thesis, University of Michigan (1997).

[51] S. Riyopoulos, D. Chernin, and D. Dialetis, *Theory of Electron Multipactor in Crossed Fields*, Phys. Plasmas **2**, 21 (1995).

[52] S. Riyopoulos, D. Chernin, and D. Dialetis, *Effect of Random Secondary Delay Times and Emission Velocities in Electron Multipactors*, IEEE Transactions on Electron Devices **44**, 489 (1997).

[53] S. Riyopoulos, *Multipactor Saturation Due to Space-Charge-Induced Debunching*, Physics of Plasmas **4**, 1448 (1997).

[54] R. Kishek and Y. Y. Lau, *Interaction of Multipactor Discharge and Rf Circuit*, Phys. Rev. Lett. **75**, 1218 (1995).

[55] R. A. Kishek and Y. Y. Lau, *A Novel Phase Focusing Mechanism in Multipactor Discharge*, Physics of Plasmas **3**, 1481 (1996).

[56] R. A. Kishek, Y. Y. Lau, and D. Chernin, *Steady State Multipactor and Dependence on Material Properties*, Physics of Plasmas **4**, 863 (1997).

[57] L.-K. Ang, Y. Y. Lau, R. A. Kishek, and R. M. Gilgenbach, *Power Deposited on a Dielectric by Multipactor*, IEEE Transactions on Plasma Science **26**, 290 (1998).

[58] A. Valfells, J. P. Verboncoeur, and Y. Y. Lau, *Space-Charge Effects on Multipactor on a Dielectric*, IEEE Transactions on Plasma Science **28**, 529 (2000).

[59] A. Valfells, L. K. Ang, Y. Y. Lau, and R. M. Gilgenbach, *Effects of an External Magnetic Field, and of Oblique Radio-Frequency Electric Fields on Multipactor Discharge on a Dielectric*, Physics of Plasmas **7**, 750 (2000).

[60] M. Siddiqi and R. Kishek, *Map-Based Multipactor Theory for Cross-Field Devices*, IEEE Transactions on Electron Devices **66**, 3162 (2019).

[61] M. Siddiqi and R. A. Kishek, *A Predictive Model for Two-Surface Multipactor Stability and Growth Based on Chaos Theory*, Physics of Plasmas **26**, 043104 (2019).

[62] M. Siddiqi and R. Kishek, *Construction of Multipactor Susceptibility Diagrams From Map-Based Theory*, IEEE Transactions on Electron Devices **66**, 3587 (2019).

[63] M. Siddiqi and R. Kishek, *A Model for Multipactor Discharge on a Dielectric Based on Chaos Theory*, IEEE Transactions on Electron Devices **66**, 4387 (2019).

[64] M. Siddiqi and R. Kishek, *A Predictive Model for Multipactor Discharge in Coaxial Systems Based on Chaos Theory*, IEEE Transactions on Electron Devices **66**, 4403 (2019).

[65] H. C. Kim and J. P. Verboncoeur, *Transition of Window Breakdown from Vacuum Multipactor Discharge to Rf Plasma*, Physics of Plasmas **13**, 123506 (2006).

[66] K. D. Bergeron, *Theory of the Secondary Electron Avalanche at Electrically Stressed Insulator-vacuum Interfaces*, Journal of Applied Physics **48**, 3073 (1977).

[67] A. G. Sazontov and V. E. Nevchaev, *Effects of Rf Magnetic Field and Wave Reflection on Multipactor Discharge on a Dielectric*, Physics of Plasmas **17**, 033509 (2010).

[68] D.-Q. Wen, P. Zhang, Y. Fu, J. Krek, and J. P. Verboncoeur, *Temporal Single-Surface Multipactor Dynamics under Obliquely Incident Linearly Polarized Electric Field*, Physics of Plasmas **26**, 123509 (2019).

[69] C. Chang, G. Liu, C. Tang, C. Chen, S. Qiu, J. Fang, and Q. Hou, *The Influence of Desorption Gas to High Power Microwave Window Multipactor*, Physics of Plasmas **15**, 093508 (2008).

[70] S. K. Nam and J. P. Verboncoeur, *Effect of Electron Energy Distribution Function on the Global Model for High Power Microwave Breakdown at High Pressures*, Applied Physics Letters **92**, 231502 (2008).

[71] S. K. Nam, C. Lim, and J. P. Verboncoeur, *Dielectric Window Breakdown in Oxygen Gas: Global Model and Particle-in-Cell Approach*, Physics of Plasmas **16**, 023501 (2009).

[72] Y. Y. Lau, J. P. Verboncoeur, and H. C. Kim, *Scaling Laws for Dielectric Window Breakdown in Vacuum and Collisional Regimes*, Applied Physics Letters **89**, 261501 (2006).

[73] H. C. Kim and J. P. Verboncoeur, *Time-Dependent Physics of a Single-Surface Multipactor Discharge*, Physics of Plasmas **12**, 123504 (2005).

[74] A. M. Perez, C. Tienda, C. Vicente, S. Anza, J. Gil, B. Gimeno, V. E. Boria, and D. Raboso, *Prediction of Multipactor Breakdown Thresholds in Coaxial Transmission Lines for Traveling, Standing, and Mixed Waves*, IEEE Transactions on Plasma Science **37**, 2031 (2009).

[75] R. Udiljak, D. Anderson, M. Lisak, V. E. Semenov, and J. Puech, *Multipactor in a Coaxial Transmission Line. I. Analytical Study*, Physics of Plasmas **14**, 033508 (2007).

[76] E. Somersalo, P. Yla-Oijala, and D. Proch, *Electron Multipacting in RF Structures*, (1994).

[77] I. A. Kossyi, G. S. Luk'yanchikov, V. E. Semenov, N. A. Zharova, D. Anderson, M. Lisak, and J. Puech, *Experimental and Numerical Investigation of Multipactor Discharges in a Coaxial Waveguide*, J. Phys. D: Appl. Phys. **43**, 345206 (2010).

[78] V. E. Semenov, E. I. Rakova, D. Anderson, M. Lisak, and J. Puech, *Multipactor in Rectangular Waveguides*, Physics of Plasmas **14**, 033501 (2007).

[79] C. Vicente, M. Mattes, D. Wolk, B. Mottet, H. L. Hartnagel, J. R. Mosig, and D. Raboso, *Multipactor Breakdown Prediction in Rectangular Waveguide Based Components*, IEEE MTT-S International Microwave Symposium Digest (2005).

[80] V. E. Semenov, E. I. Rakova, A. G. Sazontov, I. M. Nefedov, V. I. Pozdnyakova, I. A. Shereshevskii, D. Anderson, M. Lisak, and J. Puech, *Simulations of Multipactor Thresholds in Shielded Microstrip Lines*, J. Phys. D: Appl. Phys. **42**, 205204 (2009).

[81] V. E. Semenov, N. A. Zharova, D. Anderson, M. Lisak, and J. Puech, *Simulations of Multipactor in Circular Waveguides*, Physics of Plasmas **17**, 123503 (2010).

[82] A. M. Pérez, V. E. Boria, B. Gimeno, S. Anza, C. Vicente, and J. Gil, *Multipactor Analysis in Circular Waveguides*, Journal of Electromagnetic Waves and Applications **23**, 1575 (2009).

[83] A. Frotanpour, G. Dadashzadeh, M. Shahabadi, and B. Gimeno, *Analysis of Multipactor RF Breakdown Thresholds in Elliptical Waveguides*, IEEE Transactions on Electron Devices **58**, 876 (2011).

[84] J. de Lara, F. Perez, M. Alfonseca, L. Galan, I. Montero, E. Roman, and D. R. Garcia-Baquero, *Multipactor Prediction for On-Board Spacecraft RF Equipment with the MEST Software Tool*, IEEE Transactions on Plasma Science **34**, 476 (2006).

[85] F. Pérez, J. de Lara, L. Galán, M. Alfonseca, I. Montero, E. Román, and D. Raboso, *Simulation of Multipactor Effect through the Individual Simulation of Electrons*, in *Proc. 5th Int. Workshop MULCOPIM*, pp. 267–273 (2005).

[86] G. Burt, R. G. Carter, A. C. Dexter, C. Institute, and L. University, *Benchmarking Simulations of Multipactor in Rectangular Waveguides Using CST-Particle Studio*, in Proceedings of SRF2009, Berlin, Germany, pp. 321–325 (2009).

[87] G. Romanov, *Update on Multipactor in Coaxial Waveguides Using CST Particle Studio*, in Proceedings of 2011 Particle Accelerator Conference, New York, pp. 820–822, (2011).

[88] S. V. Langellotti, N. M. Jordan, Y. Y. Lau, and R. M. Gilgenbach, *CST Particle Studio Simulations of Coaxial Multipactor and Comparison With Experiments*, IEEE Transactions on Plasma Science **48**, 1942 (2020).

[89] J. Tuckmantel, C. Benvenuti, D. Bloess, D. Boussard, G. Geschonke, E. Haebel, N. Hilleret, S. Juras, H. P. Kindermann, J. Uythoven, C. Wyss, and M. Stirbet, *Improvements to Power Couplers for the LEP2 Superconducting Cavities*, in *Proceedings Particle Accelerator Conference*, Vol. 3, pp. 1642–1644 (1995).

[90] K. J. Kleman, *A New 50 MHz RF Cavity for Aladdin*, in *Proceedings of International Conference on Particle Accelerators* Vol. 2, pp. 924–926, (1993).

[91] J. W. Noé, *Freon Plasma Surface Treatment for Multipactoring*, Nuclear Instruments and Methods in Physics Research Section A: Accelerators, Spectrometers, Detectors and Associated Equipment **328**, 291 (1993).

[92] D. Proch, *SRF Cavities for Future Applications*, in *Proceedings of International Conference on Particle Accelerators,* Vol 2, pp. 758–762 (1993).

[93] E.-G. Schweppe, R. Bachmor, and E. Demmel, *Design and Results of a 1.3 MW CW Klystron for LEP*, in *Proceedings of International Conference on Particle Accelerators,* Vol 2, pp. 1178–1180 (1993).

[94] M. Ye, Y. N. He, S. G. Hu, R. Wang, T. C. Hu, J. Yang, and W. Z. Cui, *Suppression of Secondary Electron Yield by Micro-Porous Array Structure*, Journal of Applied Physics **113**, 074904 (2013).

[95] J. M. Sattler, R. A. Coutu, R. Lake, T. Laurvick, T. Back, and S. Fairchild, *Modeling Micro-Porous Surfaces for Secondary Electron Emission Control to Suppress Multipactor*, Journal of Applied Physics **122**, 055304 (2017).

[96] A. Iqbal, J. Ludwick, S. Fairchild, M. Cahay, D. Gortat, M. Sparkes, W. O'Neill, T. C. Back, and P. Zhang, *Empirical Modeling and Monte Carlo Simulation of Secondary Electron Yield Reduction of Laser Drilled Microporous Gold Surfaces*, Journal of Vacuum Science & Technology B **38**, 013801 (2020).

[97] D. Gonzalez-Iglesias, P. Soto, S. Anza, B. Gimeno, V. E. Boria, C. Vicente, and J. Gil, *Multipactor Susceptibility Charts for Ridge and Multiridge Waveguides*, IEEE Transactions on Electron Devices **59**, 3601 (2012).

[98] C. Chang, G. Z. Liu, H. J. Huang, C. H. Chen, and J. Y. Fang, *Suppressing High-Power Microwave Dielectric Multipactor by the Sawtooth Surface*, Physics of Plasmas **16**, 083501 (2009).

[99] I. Montero, S. H. Mohamed, M. García, L. Galán, and D. Raboso, *Effect of Surface Reactions of Low-Energy Carbon Ions on the Secondary Electron Emission of TiN:O Thin Films*, Journal of Applied Physics **101**, 113306 (2007).

[100] A. Ruiz, E. Román, P. Lozano, M. García, L. Galán, I. Montero, and D. Raboso, *UHV Reactive Evaporation Growth of Titanium Nitride Thin Films, Looking for Multipactor Effect Suppression in Space Applications*, Vacuum **81**, 1493 (2007).

[101] D. C. Joy, *A Database of Electron-Solid Interactions,* Scanning **17**, 270 (2006). http://web.utk.edu/~srcutk/htm/interact.htm.

[102] D. Wu, J. Ma, Y. Bao, W. Cui, T. Hu, J. Yang, and Y. Bai, *Fabrication of Porous Ag/TiO2/Au Coatings with Excellent Multipactor Suppression*, Sci Rep **7**, (2017).

[103] J. Ludwick, A. Iqbal, D. Gortat, J. D. Cook, M. Cahay, P. Zhang, T. C. Back, S. Fairchild, M. Sparkes, and W. O'Neill, *Angular Dependence of Secondary Electron Yield from Microporous Gold Surfaces*, Journal of Vacuum Science & Technology B **38**, 054001 (2020).

[104] R. A. Rimmer, Ph.D. Thesis, Lancaster University (1988).

[105] C. M. Lyneis, H. A. Schwettman, and J. P. Turneaure, *Elimination on Electron Multipacting in Superconducting Structures for Electron Accelerators*, Appl. Phys. Lett. **31**, 541 (1977).

[106] B. G. Martínez, *Recent Advances on Multipactor Effect in Satellites RF Comunications*, ECLOUD'18 La Biodola Bay, Isola d'Elba, Italy (2018). https://agenda.infn.it/event/13351/contributions/18975/attachments/13638/15344/ecloud2018_BGM_Valencia.pdf.

[107] C. Chang, G. Z. Liu, C. X. Tang, C. H. Chen, H. Shao, and W. H. Huang, *Suppression of High-Power Microwave Dielectric Multipactor by Resonant Magnetic Field*, Appl. Phys. Lett. **96**, 111502 (2010).

[108] C. Chang, J. Fang, Z. Zhang, C. Chen, C. Tang, and Q. Jin, *Experimental Verification of Improving High-Power Microwave Window Breakdown Thresholds by Resonant Magnetic Field*, Appl. Phys. Lett. **97**, 141501 (2010).

[109] O. A. Ivanov, M. A. Lobaev, V. A. Isaev, and A. L. Vikharev, *Suppressing and Initiation of Multipactor Discharge on a Dielectric by an External Dc Bias*, Physical Review Special Topics - Accelerators and Beams **13**, (2010).

[110] C. Chang, G. Liu, C. Tang, C. Chen, and J. Fang, *Review of Recent Theories and Experiments for Improving High-Power Microwave Window Breakdown Thresholds*, Physics of Plasmas **18**, 055702 (2011).

[111] European Corporation for Space Standardization (ECSS), *Space Engineering: Multipacting Design and Test*, ESA Publication Division (2013).

[112] M. Siddiqi and R. A. Kishek, *A Predictive Model for Long-Term Multipactor Discharge under Two-Carrier Operation Based on Chaos Theory*, Physics of Plasmas **26**, 113111 (2019).

[113] P. Y. Wong, P. Zhang and J. P. Verboncoeur, *Harmonic Generation in Multipactor Discharges*, IEEE Transactions on Plasma Science, vol. 48, no. 6, pp. 1959-1966, June 2020, doi: 10.1109/TPS.2020.2980482.

[114] A. A. Hubble, P. T. Partridge, and R. Spektor, *Evolution of Multipactor Breakdown in Two-Tone Systems*, in Proceedings of the 9th International Workshop on Multipactor, Corona, and Passive Intermodulation, Noordwijk, The Netherlands (2017).

[115] V. H. Chaplin, A. A. Hubble, K. A. Clements, and T. P. Graves, *Center Conductor Diagnostic for Multipactor Detection in Inaccessible Geometries*, Review of Scientific Instruments **88**, 014706 (2017).

[116] T. P. Graves, P. Hanson, J. M. Michaelson, A. D. Farkas, and A. A. Hubble, *Fast Shut-down Protection System for Radio Frequency Breakdown and Multipactor Testing*, Review of Scientific Instruments **85**, 024704 (2014).

[117] P. T. Partridge and A. A. Hubble, *Multipactor Phase Null Test Diagnostic Sensitivity and Criteria*, in Proceedings of the 9th International Workshop on Multipactor, Corona, and Passive Intermodulation, Noordwijk, The Netherlands (2017).

[118] W.-C. Tang and C. M. Kudsia, *Multipactor Breakdown and Passive Intermodulation in Microwave Equipment for Stellite Applications*, in *IEEE Conference on Military Communications,* Vol 1, pp. 181–187 (1990).

[119] L. Zhang, Y. Li, S. Lin, H. Wang, C. Liu, J. Li, and Z. Xu, *Numerical Simulation and Analysis of Passive Intermodulation Caused by Multipaction*, Physics of Plasmas **25**, 082301 (2018).

[120] V. E. Semenov, E. I. Rakova, N. A. Zharova, J. Rasch, D. Anderson, and J. Puech, *Simple Model of the Rf Noise Generated by Multipacting Electrons*, J. Phys. D: Appl. Phys. **47**, 055206 (2014).

[121] S. A. Rice and J. P. Verboncoeur, *Migration of Multipactor Trajectories via Higher-Order Mode Perturbation*, IEEE Transactions on Plasma Science **45**, 1739 (2017).

[122] D.-Q. Wen, A. Iqbal, P. Zhang, and J. P. Verboncoeur, *Suppression of Single-Surface Multipactor Discharges Due to Non-Sinusoidal Transverse Electric Field*, Physics of Plasmas **26**, 093503 (2019).

[123] A. Iqbal, J. Verboncoeur, and P. Zhang, *Temporal Multiparticle Monte Carlo Simulation of Dual Frequency Single Surface Multipactor*, Physics of Plasmas **26**, 024503 (2019).

[124] A. Iqbal, P. Y. Wong, J. P. Verboncoeur, and P. Zhang, *Frequency-Domain Analysis of Single-Surface Multipactor Discharge With Single- and Dual-Tone RF Electric Fields*, IEEE Transactions on Plasma Science **48**, 1950 (2020).

[125] Iqbal, P. Y. Wong, D.-Q. Wen, S. Lin, J. P. Verboncoeur, and P. Zhang, *Time-Dependent Physics of Single-Surface Multipactor Discharge with Two Carrier Frequencies*, Physical Review E **102**, 043201 (2020). DOI: 10.1103/PhysRevE.102.043201

[126] J. R. M. Vaughan, *Secondary Emission Formulas*, IEEE Transactions on Electron Devices **40**, 830 (1993).

[127] A. Iqbal, J. Verboncoeur, P. Wong, and P. Zhang, *Temporal Study of Dual Frequency Single Surface Multipactor by Multiparticle Monte Carlo Simulations*, in *2019 International Vacuum Electronics Conference (IVEC)*, pp. 1–2 (2019).

[128] Sorolla Rosario, F. E., *Contribution to Modeling Multipactor and Corona Discharges in High Power Electromagnetic Fields*, Ph.D. Thesis, Swiss Federal Institute of Technology Lausanne (2012). https://doi.org/10.5075/epfl-thesis-5542.

[129] CST Studio Suite, Dassault Systems, Vélizy-Villacoublay, France (2019).

[130] U. Singh, N. Kumar, N. Kumar, A. Kumar, and A. K. Sinha, *Three-Dimensional Simulation of Triode-Type MIG for 1MW, 120GHz Gyrotron for ECRH Applications*, Infrared Physics & Technology **55**, 108 (2012).

[131] J. Han and S. Ryu, *Optimal Operating Conditions Based on Mode Competition for Maximum Efficiency of Double-Strapped Magnetron*, IEEE Transactions on Plasma Science **47**, 3160 (2019).

[132] D. Safi, P. Birtel, S. Meyne, and A. F. Jacob, *A Traveling-Wave Tube Simulation Approach With CST Particle Studio*, IEEE Transactions on Electron Devices **65**, 2257 (2018).

[133] CST Studio Suite Help, Dassault Systems, Vèlizy-Villacoublay, France, (2019).

[134] Á. Valfells, D. W. Feldman, M. Virgo, P. G. O'Shea, and Y. Y. Lau, *Effects of Pulse-Length and Emitter Area on Virtual Cathode Formation in Electron Guns*, Physics of Plasmas **9**, 2377 (2002).

[135] W. Li, J. X. Ma, J. Li, Y. Zheng, and M. Tan, *Measurement of Virtual Cathode Structures in a Plasma Sheath Caused by Secondary Electrons*, Physics of Plasmas **19**, 030704 (2012).

[136] J. W. Luginsland, S. McGee, and Y. Y. Lau, *Virtual Cathode Formation Due to Electromagnetic Transients*, IEEE Transactions on Plasma Science **26**, 901 (1998).

[137] P. Zhang, Á. Valfells, L. K. Ang, J. W. Luginsland, and Y. Y. Lau, *100 Years of the Physics of Diodes*, Applied Physics Reviews **4**, 011304 (2017).

[138] P. Zhang, Y. S. Ang, A. L. Garner, Á. Valfells, J. W. Luginsland, and L. K. Ang, *Space–Charge Limited Current in Nanodiodes: Ballistic, Collisional, and Dynamical Effects*, Journal of Applied Physics **129**, 100902 (2021).

[139] G. Romanov, *Simulation of Multipacting with Space Charge Effect*, AJPA **5**, 99 (2017).